

Dissertation

submitted to the
Combined Faculties for the Natural Sciences and for Mathematics
of the Ruperto-Carola University of Heidelberg, Germany
for the degree of
Doctor of Natural Sciences

presented by
Diplom-Physiker Klaus Klingmüller
born in Bonn

Oral examination: 17. Oktober 2007

Worldline approach to Casimir effect and Gross-Neveu model

Referees:

PD Dr. Holger Gies

Prof. Dr. Michael G. Schmidt

Weltlinienzugang zu Casimir-Effekt und Gross-Neveu Modell

Zusammenfassung

Wir untersuchen den Casimir-Effekt und das Gross-Neveu Modell mit Hilfe der Weltliniennumerik. Dabei werden die Quantenfluktuationen auf quantenmechanische Pfadintegrale von Punktteilchen abgebildet, welche wir mit Monte-Carlo-Methoden auswerten. Beim Casimir-Effekt erlaubt uns das die präzise Berechnung der Wechselwirkungsenergien für ein Dirichlet-Skalar in für andere Methoden unzugänglichen Casimir-Geometrien. Wir untersuchen Geometrien mit Krümmungen und scharfen Kanten, beide sind von großer Bedeutung für Experimente bzw. die Anwendung in der Nanomechanik. Bei der Berechnung nutzen wir die jeweiligen Symmetrien aus, um eine erhebliche Verringerung der nötigen Rechenzeit zu erzielen. Unsere Ergebnisse zeigen die engen Grenzen der gängigen "Proximity Force Approximation" (PFA) auf und liefern erste Erkenntnisse über den Einfluss der Kanten endlicher Platten auf die Casimir-Kraft. Im Gross-Neveu Modell berechnen wir die Spur über die Fermionfluktuationen mit einem Weltlinienpfadintegral. Dessen numerische Berechnung demonstrieren wir an verschiedenen Konfigurationen des zweidimensionalen Modells. Wir beziehen Temperatur und chemisches Potential in unsere Beschreibung ein und stellen erstmalig weltliniennumerische Berechnungen bei endlichen Werten dieser Größen an. Dabei entdecken wir Teilaspekte des bekannten Phasendiagramms wieder. Die verwendeten Methoden sind grundsätzlich auf höhere Dimensionen übertragbar und stellen für solche eine Aussage über die Existenz eines räumlich inhomogenen Grundzustandes in Aussicht.

Worldline approach to Casimir effect and Gross-Neveu model

Abstract

We employ worldline numerics to study Casimir effect and Gross-Neveu model. In this approach, the quantum fluctuations are mapped onto quantum mechanical path integrals, which are evaluated with Monte Carlo methods. For the Casimir effect, this allows the precise computation of the interaction energy for a Dirichlet scalar in Casimir geometries inaccessible to other methods. We study geometries involving curvature and edges, both are important for experiments and applications in nanotechnology, respectively. Significant reduction of numerical cost is gained by exploiting the symmetries of the worldline ensemble in combination with those of the configurations. Our results reveal the tight validity bounds of the commonly used proximity force approximation (PFA) and provide first insight into the effect of edges of finite plates on the Casimir force. In the Gross-Neveu model, we compute the trace over the fermion fluctuations using a worldline path integral, whose numerical evaluation is demonstrated for various configurations in the two dimensional model. We incorporate temperature and chemical potential in our formalism and perform first worldline numeric computations at finite values of these quantities. We thereby rediscover aspects of the established phase diagram. The methods employed can be extended to higher dimensions, to study the existence of a spatially inhomogeneous ground state beyond the two dimensional Gross-Neveu model.

Contents

I	Casimir effect	1
1	Introduction	3
2	Casimir's parallel plates	7
3	Casimir effect on the worldline	13
3.1	Field theoretic framework	13
3.2	Worldline formulation for a Dirichlet scalar	15
3.3	Worldline numerics	19
4	Casimir curvature effects	21
4.1	Introduction	22
4.2	Sphere above plate	23
4.2.1	Inside	24
4.2.2	Outside	25
4.2.3	Optimization	27
4.2.4	Results	29
4.3	Cylinder above plate	32
5	Casimir edge effects	35
5.1	Introduction	36
5.2	Casimir edge configurations	38
5.2.1	Parallel plates revisited	38
5.2.2	Perpendicular Plates	40
5.2.3	Semi-infinite plate parallel to an infinite plate	43
5.2.4	Thick plates	48
5.2.5	Parallel semi-infinite plates	49
5.3	Edge-configuration estimates	54
5.3.1	Casimir comb	54
5.3.2	Finite parallel-plate configurations	55
6	Conclusions (Part I)	57

A	The proximity force approximation (PFA)	59
A.1	Sphere above plate	60
A.2	Cylinder above plate	61
II	Gross-Neveu model	63
7	Introduction	65
8	The Gross-Neveu model on the worldline	67
8.1	Euclidean action	67
8.2	Auxiliary field	68
8.3	Worldline formalism	70
9	Worldline numerics in two dimensions	73
9.1	Renormalisation	73
9.2	Spatially varying potentials	77
9.3	Single kink	78
9.4	Kink-antikink	80
9.5	Periodic array of kink-antikink pairs	85
10	Temperature	89
10.1	Symmetry restoration	90
11	Chemical potential	93
12	Towards the phase diagram	97
12.1	Phase diagram of the constant potential	97
12.2	In search of crystals	98
13	Conclusions (Part II)	101
	Bibliography	103

Part I

Casimir effect

Chapter 1

Introduction

Recent years have witnessed remarkable qualitative and quantitative progress in the understanding of the Casimir effect [1] both experimentally and theoretically. Measurements of the Casimir force have reached a precision level of 1% [2–7]. Further improvements are currently aimed at with intense efforts, owing to the increasing relevance of these quantum forces for nano- and micro-scale mechanical systems. Also from the perspective of fundamental physics, Casimir precision measurements play a major role in the search for new sub-millimetre forces, resulting in important constraints for new physics [8–15].

On this level of precision, corrections owing to surface roughness, finite conductivity, thermal fluctuations and geometry dependencies have to be accounted for [16–21]. These corrections may be classified in terms of material corrections on the one hand; they are induced, for instance, by surface roughness and finite conductivity which may be viewed as a deviation from the ideal Casimir configuration. On the other hand, corrections due to geometry dependence are of direct quantum origin and thus universal, i.e., independent of the microscopic details of the interactions between the fluctuating field and the constituents of the surfaces. Since material corrections are difficult to control with high precision, force measurements at larger surface separations up to the micron range are intended.* Though this implies stronger geometry dependence, this universal effect is, in principle, under clean theoretical control, since it follows directly from quantum field theory [25].

Straightforward computations of geometry dependencies have long been conceptually complicated, since the relevant information is subtly encoded in the fluctuation spec-

*Measurements at larger surface separations are also aimed at in order to resolve a recent controversy about thermal corrections, see [22, 23] and references therein. Even though thermal contributions are also universal in the *ideal* Casimir limit, they can mix nontrivially with material corrections in a way that may affect any *real* experiment [22, 24].

trum. Generically, analytic solutions are restricted to highly symmetric geometries. This problem is particularly prominent, since current and future precision measurements predominantly rely on configurations involving curved surfaces, such as a sphere above a plate. Curved configurations help to circumvent the difficulty of maintaining parallelism as it occurs in the parallel-plate configuration; the latter has been mastered so far only in one experiment [26] with a precision level of $\sim 15\%$. As a general recipe for curved configurations, the proximity force approximation (PFA) [27, 28] has been the standard, though uncontrolled, tool for estimating curvature effects for non-planar geometries in all experiments so far.

In addition, the rapid progress in the fabrication and use of micro- and nano-scale mechanical devices demands for new theoretical tools to compute Casimir forces: on the nano-scale the Casimir force of the electromagnetic field becomes a dominant force but the complex geometry of such devices, typically involving sharp edges, prohibits to make use of conventional approaches such as the PFA. At the same time nano-mechanical devices are subject of precision measurements of the Casimir forces in these systems [2–7, 14, 15].

In recent years, various new techniques have been developed for computing Casimir effects in more involved geometries [25, 29–41], each with its own merits and limitations. This includes improved approximation techniques which can deal with curved geometries more reliably, such as the semiclassical approximation [29, 30] and the optical approximation [36, 37], as well as exact field theoretic methods based on functional-integral techniques [31–34, 40, 41] or scattering theory [25, 38, 39].

In this work, we use and further develop *worldline numerics* [35, 42–45], which facilitates Casimir computations from field-theoretic first principles. Worldline numerics builds on a combination of the string-inspired approach to quantum field theory [46–52] with Monte Carlo methods. As a main advantage, the worldline algorithm can be formulated for arbitrary geometries, resulting in a numerical estimate of the exact answer [35]. The inherent use of Feynman path-integral techniques circumvents the problem of determining the Casimir fluctuation spectrum [53], which is often encountered in other approaches. The resulting algorithms are trivially scalable and computational efforts increase only linearly with the parameters of the numerics.

Our results obtained by worldline numerics [54] go hand in hand with those obtained by new analytical methods [38–41] which are based on advanced scattering-theory techniques; excellent agreement has been found for the experimentally important sphere-plate and cylinder-plate Casimir configurations.

In addition to being a simple and reliable quantitative method, the worldline formalism also offers an intuitive picture of quantum-fluctuation phenomena. The

fluctuations are mapped onto closed Gaussian random paths (worldlines) which represent the spacetime trajectories of virtual loop processes. The Casimir interaction energy between two surfaces can thus be obtained by identifying all worldlines that intersect both surfaces. These worldlines correspond to fluctuations that would violate the boundary conditions; their removal from the ensemble of all possible fluctuations thereby contributes to the (negative) Casimir interaction energy. The latter measures only that part of the energy that contributes to the force between rigid surfaces; possibly divergent self-energies of the single surfaces [25] are already removed. An example for a computation of single-surface energies for configurations with edges can be found in [55].

This part of the theses is organised as follows: In chapter 2 we recover Casimir's result for the classic parallel plate configuration. An introduction to the worldline-numerical approach in the context of the Casimir effect is given in chapter 3. We explicitly formulate the problem for a scalar field with Dirichlet boundaries and show the relation of Casimir energy and effective action. For the effective action we then derive the worldline expression and present the general recipe how to evaluate it numerically. Chapter 4 is devoted to Casimir curvature effects. We employ worldline numerics to study the sphere-plate and the cylinder-plate configuration. We place emphasis on optimising the general algorithm by exploiting the symmetries of the given geometries. In chapter 5 we study various Casimir configurations involving edges. Our conclusions are provided in chapter 6. In the appendix A we describe the proximity force approximation which is not only a simple (though potentially misleading) approximation, but also provides for a useful normalization for our numerical results.

Chapter 2

Casimir's parallel plates

In its original form, the Casimir force was introduced as retarded London-van der Waals force by Hendrik B. G. Casimir and Dirk Polder in 1947 [56]. Taking the finiteness of the speed of light into account, they studied the force between a neutral atom and a neutral, perfectly conducting plane, as well as the force between two neutral atoms. However, today the term “Casimir Effect” often refers to the attraction between two planes. This variant was studied by Casimir in 1948 [1]. The innovation he introduced in this later work was to shift the focus from the quantum fluctuations of the charge carriers inside the interacting objects to the fluctuations of the electromagnetic field. The result has been an alternative, equivalent description of the same physical effect.

In Casimir's approach, not the complex dynamics and interactions of the individual charges enter the computation, but only their implications for the vacuum fluctuations of the electromagnetic field: the behaviour of the charges effectively imposes boundary conditions on the field—on the surface of the conductors the tangential component of the electric and the perpendicular component of the magnetic field vanish.

From this it follows a change of the field's zero-point energy: All modes contradicting the boundary conditions are excluded from the mode sum. This selection obviously depends on the geometry of the boundaries, in particular on the distance of the plates. Thus the zero-point energy obtains a distance dependency, leading to an—in case of the two plates—attractive force on the boundaries. We emphasize that the force does only depend on the change of the energy and not on the absolute value. Thus, the Casimir force is no evidence for a vacuum energy, as sometimes discussed in conjunction with a cosmological constant. As retarded London-van der Waals force, it can be formulated without reference to zero-point energies [57].

Let us briefly recover Casimir's result for the electromagnetic field in the parallel-

plates geometry. Different aspects of this computation are important for the work at hand: The proximity force approximation (PFA), the standard tool for non-planar Casimir geometries, relies heavily on the parallel-plates result and will be referred to for comparison several times in this theses. The PFA is described in detail in Appendix A. In section 5.2.1 we will derive an alternative expression for the Casimir energy of the parallel plates, which depends on a statistical quantity of random walks. Comparing both expressions, a simple analytic formula for the statistical quantity is obtained. Finally, the basic procedure of the parallel-plate calculation is common for most Casimir computations, but differs significantly from the approach employed in this theses. To point out these differences and depict the shortcomings of the procedure, the parallel-plate calculation is a very illustrative example.

The common recipe to compute Casimir forces consists of three major steps:

1. finding the *modes* of the fluctuating field,
2. summing over the spectrum to obtain the Casimir *energy*,
3. differentiating with respect to a geometry parameter to obtain the Casimir *force*.

In the following we will exercise this recipe for the classic Casimir configuration.

1. *Modes*: Without the plates, a basis of the free field is given by plane wave solutions,

$$\mathbf{E} = \epsilon_{1,2} e^{i(\mathbf{k}\mathbf{x} - \omega t)}, \quad \mathbf{B} = \mathbf{e}_{\mathbf{k}} \times \mathbf{E}, \quad (2.1)$$

with the two linearly independent polarisation vectors ϵ_1 and ϵ_2 perpendicular to the wave vector \mathbf{k} .

Adding one single plate in the y - z plane at $x = 0$, the boundary condition for the electric field,

$$\mathbf{n} \times \mathbf{E}|_{x=0} = 0, \quad (2.2)$$

where \mathbf{n} is the normal of the plate, only allows linear combinations of plane waves with a node at $x = 0$, except for the case $\mathbf{k} \perp \mathbf{n}$. In this special case, the electric-field vector \mathbf{E} of the plane wave can be perpendicular to the plate, but this implies the magnetic field \mathbf{B} to be parallel to the plate, in contradiction to the second boundary condition,

$$\mathbf{n} \cdot \mathbf{B}|_{x=0} = 0. \quad (2.3)$$

Thus for a single plate the modes are given by linear combinations of plane waves with a node on the plate. Due to the dispersion relation $|\mathbf{k}| = \omega$ a plane wave with given \mathbf{k}

and ω can only occur in combination with a plane wave with $\mathbf{k}' = (-k_x, k_y, k_z)^\top$ in the form

$$\epsilon_{1,2} \left(e^{i(k_x x + k_y y + k_z z - \omega t)} - e^{i(-k_x x + k_y y + k_z z - \omega t)} \right) = 2i \epsilon_{1,2} \sin(k_x x) e^{i(k_y y + k_z z - \omega t)} \quad (2.4)$$

so that a suitable basis is

$$\mathbf{E} = \epsilon_{1,2} \sin(k_x x) e^{i(k_y y + k_z z - \omega t)}. \quad (2.5)$$

In the same way, adding a second plate at $x = a$ in the y - z plane demands for a node in this plane. Only those wave vectors are possible, for which $\sin(k_x a)$ vanishes, i.e., $k_x = n\pi/a$ with an integer $n \geq 1$. Thus we can finally specify the modes for the field inside of two parallel plates:

$$\mathbf{E} = \epsilon_{1,2} \sin\left(\frac{na}{\pi} x\right) e^{i(k_y y + k_z z - \omega t)}. \quad (2.6)$$

Outside the plates, the modes are of course still given by Eq. (2.5) for $x < 0$ and the same equation with x replaced by $x - a$ for $x > a$, respectively.

The corresponding real vector-space of the real parts of the fields has the basis

$$\mathbf{E} = \epsilon_{1,2} \sin\left(\frac{na}{\pi} x\right) \begin{Bmatrix} \sin \\ \cos \end{Bmatrix} (k_y y + k_z z - \omega t). \quad (2.7)$$

2. Energy: The Casimir-energy is obtained by summing the zero-point energies of all modes,

$$E_{\text{Casimir}} = \sum_i \frac{1}{2} \hbar \omega_i, \quad (2.8)$$

where the index i identifies the modes. In general this sum is infinite, demanding for a careful handling of divergences. These divergences can arise from fluctuations that induce a RG running of renormalisable operators and can be removed by fixing physical parameters. Some divergences may also be artificial, since they might be induced by an unphysical over-idealised limit (such as perfect conductivity). For two disjunct bodies, the finite distance-dependent part can be extracted by subtracting the infinite-distance limit. Here, without mathematical rigour, we employ dimensional regularisation which simply projects out all divergences. The number of dimensions $D = d + 1$ will be treated as a continuous, complex variable. As a byproduct, the final expressions will be valid even for $D \neq 4$. For a more rigorous and detailed treatment see e.g. reference [58].

In case of the free field, the mode sum corresponds to an integration over all possible wave vectors \mathbf{k} and a sum over both polarizations $\epsilon_{1,2}$,

$$E_{\text{Casimir}} = V \int \frac{d^d k}{(2\pi)^d} \sum_{\epsilon_{1,2}} \frac{1}{2} \omega_{\mathbf{k}}, \quad (2.9)$$

where we have set \hbar to unity. Between the two plates, the component k_x is discrete, $k_x = n\pi/a$ and thus $dk_x = \pi/a$. The energy $\omega_{\mathbf{k}}/2$ is independent of the polarisation and the corresponding sum gives merely a factor of two (as for the free field). Another factor of two comes from summing over the two possible functions sin and cos in Eq. (2.7). We obtain

$$E_{\text{Casimir}} = 4V \int \frac{d^{d-1} k}{(2\pi)^{d-1}} \sum_{n=1}^{\infty} \frac{1}{2a} \frac{1}{2} \omega_{\mathbf{k}} \quad (2.10)$$

$$= A \int \frac{d^{d-1} k}{(2\pi)^{d-1}} \sum_{n=1}^{\infty} \sqrt{\left(\frac{n\pi}{a}\right)^2 + k^2}, \quad (2.11)$$

where we have denoted the area of the plates V/a with A . A proper-time representation of the square root, Gaussian integration, summation and analytical continuation in d yields [59]

$$E_{\text{Casimir}} = A \sum_{n=1}^{\infty} \int \frac{d^{d-1} k}{(2\pi)^{d-1}} \int_0^{\infty} \frac{dt}{t} t^{-1/2} e^{-t(k^2 + n^2\pi^2/a^2)} \frac{1}{\Gamma(-1/2)} \quad (2.12)$$

$$= -A \frac{1}{2\sqrt{\pi}} \frac{1}{(4\pi)^{(d-1)/2}} \sum_{n=1}^{\infty} \int_0^{\infty} \frac{dt}{t} t^{-1/2-d/2} e^{-tn^2\pi^2/a^2} \quad (2.13)$$

$$= -A \frac{1}{2\sqrt{\pi}} \frac{1}{(4\pi)^{(d-1)/2}} \left(\frac{\pi}{a}\right)^d \Gamma(-d/2) \zeta(-d-2) \quad (2.14)$$

$$= -A \frac{1}{2^d \pi^{(d+1)/2}} \frac{1}{a^d} \Gamma((d+1)/2) \zeta(d+1) \quad (2.15)$$

$$= -\frac{2A}{2^D \pi^{D/2} a^{D-1}} \Gamma(D/2) \zeta(D). \quad (2.16)$$

For $D = 4$, the energy per area evaluates to

$$\frac{E_{\text{Casimir}}}{A} = -\frac{\pi^2}{720} \frac{1}{a^3}. \quad (2.17)$$

3. *Force*: Finally, differentiation with respect to minus the distance a yields the attractive Casimir force per area:

$$\frac{F_{\text{Casimir}}}{A} = -\frac{d}{da} \frac{E_{\text{Casimir}}}{A} = -\frac{\pi^2}{240} \frac{1}{a^4}. \quad (2.18)$$

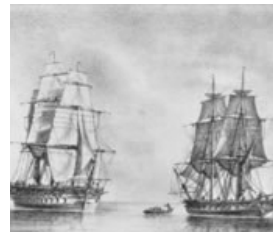
In different scenarios, it might be useful to differentiate with respect to other parameters, such as angles (to obtain Casimir torques).

In general, step 1 and 2 are the problematic ones. For most geometries, one cannot explicitly determine the modes of the fluctuating field. Even if the modes can be identified, the divergences occurring in the mode sum are not necessarily controllable. The worldline approach to the Casimir effect, which will be presented in the next chapter, addresses these problems by combining step 1 and step 2 in one single computational step.

Casimir explicitly addressed the electromagnetic field between two conductors, but the same principle is true for any fluctuating field with boundary conditions. For example in the (at least historically relevant) hadron bag-model [60] the spherical boundary is supposed to be a perfect colour magnetic conductor imposing boundary conditions on the colour electromagnetic field in its interior. The fluctuations do not even have to be of quantum nature: acoustic noise may also cause a Casimir force [61] and an attraction between ships (Fig. 2.1), rooted in the modification of the water-wave spectrum induced by the hulls [62–64] is still discussed. In this thesis, we will concentrate on a scalar field obeying Dirichlet boundaries. For such a field, the parallel-plates computation is much the same as the preceding calculation. The only difference is the polarisation vector, which is not present for the scalar field. Therefore Eq. (2.10) and therewith the final results just differ by a factor of two and we can immediately write down the parallel-plates Casimir energy for the Dirichlet scalar in D dimensions:

$$E_{\text{Casimir}} = -\frac{A}{(4\pi)^{D/2} a^{D-1}} \Gamma(D/2) \zeta(D). \quad (2.19)$$

An alternative expression for the same quantity will be derived in section 5.2.1.



Calme avec grosse houle.

À la suite d'un très-mauvais temps il arrive quelquefois que le vent calme tout-à-coup; mais il n'en est pas de même de la mer, qui reste grosse long-temps encore, et tourmente le bâtiment par des mouvements d'autant plus violents qu'il n'est plus appuyé par la résistance du vent sur les voiles.

Dans cette position, la mâture est compromise, si on ne prend pas promptement les mesures nécessaires pour la soutenir, en ridant les gal-

haubans des deux bords et bridant les bas-haubans s'ils ont pris trop de mou.

Lorsque plusieurs bâtiments se trouvent réunis, on ne doit pas négliger de manœuvrer pour saisir le plus petit souffle de vent, afin de s'écarter et d'éviter les abordages, qui seraient extrêmement dangereux. Lorsqu'on se trouve assez éloigné du bâtiment le plus voisin, on peut amener et carguer les voiles pour les ménager.

Le Calme plat.

LORSQUE deux bâtiments sont en calme, ils tendent toujours à se rapprocher et finissent par s'aborder, étant attirés l'un vers l'autre par une certaine force attractive: dans ce cas, on se sert des canots pour s'éloi-

guer, et on y parvient plus promptement en faisant remorquer l'un des bâtiments par les canots des deux. Les petits bâtiments ont de plus la ressource de leurs avirons de galère.



Figure 2.1: "Une certaine force attractive" P. C. Caussée, *L'Album du Marin*, 1836 [62]

Chapter 3

Casimir effect on the worldline

In this chapter, we present the basic concept of how to employ worldline numerics to compute Casimir energies, which has been originally described in [35]. Generally, we work in $D = d + 1$ dimensional Euclidean spacetime. If not stated otherwise, all quantities are supposed to be Euclidean. Minkowskian quantities are explicitly denoted by the subscript M.

3.1 Field theoretic framework

We consider a real scalar quantum field ϕ . For the time being, it may be massive with mass m , but with the electromagnetic field as most prominent object of study in mind, we will work with a massless field later on. Anyway, all computations could be easily performed with a finite mass m , too.

The Casimir geometry is implemented by coupling the quantum field to a background potential $V(x)$. The shape of the potential determines the kind of boundary conditions it imposes on the field. Qualitatively one can say, the amplitude of the ϕ field fluctuations is suppressed at those regions of spacetime, where the potential $V(x)$ is large. Thus, Dirichlet boundaries can be modelled using delta functionals as illustratively shown in Fig. 3.1 and more precisely defined later in Eq. (3.18). Variants of this kind of potential can also be used to realise finite conductivity, for example.

Kinetic term, mass term and the coupled potential form the field-theoretic Euclidean Lagrangian

$$\mathcal{L} = \frac{1}{2} \partial_\mu \phi \partial_\mu \phi + \frac{1}{2} m^2 \phi^2 + \frac{1}{2} V(x) \phi^2. \quad (3.1)$$

Our aim is to compute the vacuum energy, i.e. the energy of the vacuum state Ω . Of course, the final result should be the physical Minkowskian quantity, $E_{\Omega\text{M}}$. The

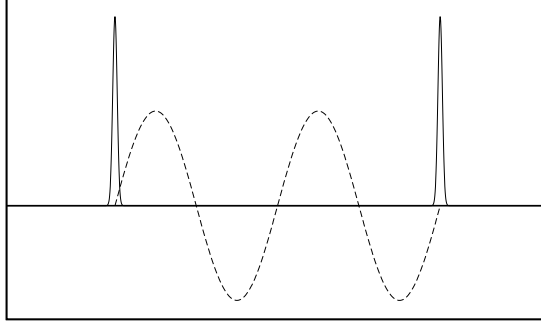


Figure 3.1: Boundary conditions induced by a background potential (solid peaks). The fluctuations of the quantum field (dashed line) are suppressed where the potential is large.

vacuum energy appears in the vacuum-persistence amplitude,

$$\langle \Omega | e^{-iH_M T} | \Omega \rangle \equiv e^{-iE_{\Omega M} T} = \int \mathcal{D}\phi e^{i(S_M + \int J\phi)} = e^{-iW_M}, \quad (3.2)$$

with the generating functional of the connected Green's functions W_M . The extension in time direction $T = \int dx^0$ is supposed to go to infinity. We conclude

$$E_{\Omega M} = \frac{W_M}{\int dx^0}. \quad (3.3)$$

The effective action Γ_M is defined as a Legendre transform of the generating functional W_M as a function of the external source J , and thus, in the absence of any sources ($J \equiv 0$), both quantities are identical except for the sign, $\Gamma_M = -W_M$, so that

$$E_{\Omega M} = -\frac{\Gamma_M}{\int dx^0}. \quad (3.4)$$

With worldline numerics we are able to compute the effective action, to be more precise the *Euclidean* effective action Γ . Hence, we finally write the Mikowskian vacuum energy $E_{\Omega M}$ in terms of the Euclidean action and the Euclidean time x_D , using the relations $\Gamma = -i\Gamma_M$ and $x_D = ix^0$:

$$E_{\Omega M} = \frac{\Gamma}{\int dx_D}. \quad (3.5)$$

It is this quantity that we call “Casimir energy” and will denote with $\mathcal{E} := E_{\Omega M}$ in the following, in contrast to the “Casimir interaction energy” E_{Casimir} which will be

introduced in the subsequent section.

3.2 Worldline formulation for a Dirichlet scalar

We will now derive the worldline expression for the effective action of a real Dirichlet scalar which can be evaluated numerically as described in the next section. For an extensive review of the worldline formalism in general see [50].

We make use of the Euclidean version of the last relation in Eq. (3.2) (with $J \equiv 0$),

$$e^{-\Gamma} = e^{\mathbb{W}} = \int \mathcal{D}\phi e^{-S}. \quad (3.6)$$

The expansion of the classical action $S = \int d^D x \mathcal{L}$ in the exponent on the right hand side about its stationary point $\phi_{\text{cl}} \equiv 0$ terminates after the $\mathcal{O}(\phi^2)$ term, because higher functional derivatives of the Lagrangian Eq. (3.1) are zero. In addition, the classical action of the classical field $S[\phi_{\text{cl}}]$ is zero so that there is only the quadratic one-loop term in the expansion and the path integral is Gaussian:

$$e^{-\Gamma} = \int \mathcal{D}\phi e^{-1/2 \int \phi \frac{\delta^2 S}{\delta \phi^2} \phi} = \det^{-1/2} \frac{\delta^2 S}{\delta \phi^2}. \quad (3.7)$$

We end up with the effective action

$$\Gamma = \frac{1}{2} \ln \det \frac{\delta^2 S}{\delta \phi^2} = \frac{1}{2} \text{Tr} \ln \frac{\delta^2 S}{\delta \phi^2}. \quad (3.8)$$

Carrying out the functional derivatives, we obtain the complete unrenormalised effective action as a function of V ,

$$\Gamma[V] = \frac{1}{2} \text{Tr} \ln \frac{-\partial^2 + m^2 + V(x)}{-\partial^2 + m^2}, \quad (3.9)$$

which is already normalised to satisfy the relation $\Gamma[0] = 0$. Next, we use a proper-time representation of the logarithm with UV cutoff Λ at the lower bound of the

propertime integral* and perform the trace in x space,

$$\Gamma[V] = -\frac{1}{2} \int d^D x \langle x | \int_{1/\Lambda^2}^{\infty} \frac{dT}{T} \left(e^{-T(-\partial^2 + m^2 + V(x))} - e^{-T(-\partial^2 + m^2)} \right) | x \rangle \quad (3.10)$$

$$= -\frac{1}{2} \int_{1/\Lambda^2}^{\infty} \frac{dT}{T} \int d^D x \left(\langle x | e^{-T(-\partial^2 + m^2 + V(x))} | x \rangle - \frac{1}{(4\pi T)^{D/2}} e^{-m^2 T} \right). \quad (3.11)$$

Performing the trace in x space is actually crucial for our approach. There is no need to determine the spectrum of the operator in the Tr-In term of Eq. (3.9), which would correspond to the explicit determination of the modes of the fluctuating field as we have demonstrated for the parallel plates in chapter 2. Thus, this delicate task which is solvable only for very few Casimir configurations is not required in the worldline approach!

Interpreting the matrix element $\langle x | \dots | x \rangle$ as a quantum mechanical transition amplitude in propertime T , we can introduce the Feynman path integral, or worldline, representation,

$$\begin{aligned} \int d^D x \langle x | e^{-T(-\partial^2 + V(x))} | x \rangle \\ = \int d^D x_{\text{CM}} \mathcal{N} \int_{x(0)=x(T)} \mathcal{D}x e^{-\int_0^T d\tau \dot{x}^2/4 - \int_0^T d\tau V(x_{\text{CM}} + x(\tau))}. \end{aligned} \quad (3.12)$$

The Tr operation of Eq. (3.9), which has led to a transition amplitude at *coincident* points in Eq. (3.11), induces a path integral over *closed* worldlines, $x(0) = x(T)$. In Eq. (3.12), we have shifted all worldline loops under the spacetime integral to have a common centre of mass x_{CM} , implying $\int_0^T d\tau x_{\mu}(\tau) = 0$. The normalization \mathcal{N} is determined from the limit of zero potential,

$$\langle x | e^{T\partial^2} | x \rangle \equiv \frac{1}{(4\pi T)^{D/2}} = \mathcal{N} \int_{x(0)=x(T)} \mathcal{D}x e^{-\int_0^T d\tau \dot{x}^2/4}, \quad (3.13)$$

such that the path integral can be interpreted as an expectation value with respect to

*Other regularization techniques are possible as well, e.g., dimensional regularization, $(dT/T) \rightarrow \mu^{2\epsilon}(dT/T^{1-\epsilon})$; the propertime cutoff is used only for the sake of definiteness. For a pedagogical review of various regularization techniques in the Casimir context, see [65].

an ensemble of worldlines with Gaußian velocity distribution,

$$\mathcal{N} \int_{x(0)=x(T)} \mathcal{D}x \dots e^{-\int_0^T d\tau \dot{x}^2/4} = \frac{1}{(4\pi T)^{D/2}} \langle \dots \rangle_x. \quad (3.14)$$

Equation (3.11) finally reads

$$\Gamma[V] = -\frac{1}{2} \frac{1}{(4\pi)^{D/2}} \int_{1/\Lambda^2}^{\infty} \frac{dT}{T^{1+D/2}} e^{-m^2 T} \int d^D x_{\text{CM}} \langle e^{-\int_0^T d\tau V(x(\tau))} - 1 \rangle_x. \quad (3.15)$$

In this work, we concentrate on Casimir forces between disconnected rigid bodies which we represent by a time-independent potential $V(\mathbf{x}) = V_1(\mathbf{x}) + V_2(\mathbf{x}) + \dots$; the potentials $V_i(\mathbf{x})$ for the single bodies have pairwise disjoint supports, i.e., $V_i(\mathbf{x})V_j(\mathbf{x}) = 0$ for all \mathbf{x} and $i \neq j$. As described above (Eq. (3.5)) we obtain the Casimir energy from the effective action by scaling out the trivial time integration, cf. Eq. (3.5),

$$\mathcal{E} = \frac{\Gamma}{\int d^D x_{\text{CM},D}}. \quad (3.16)$$

For the Casimir force, only the portion of the Casimir energy which depends on the relative position of the objects is relevant. This portion can conveniently be extracted from the total Casimir energy by subtracting the (self-)energies of the single objects. This leads us to the *Casimir interaction energy*,

$$E_{\text{Casimir}} := \mathcal{E}_{V_1+V_2+\dots} - \mathcal{E}_{V_1} - \mathcal{E}_{V_2} - \dots, \quad (3.17)$$

which serves as the potential energy for the Casimir force; i.e., Casimir forces (or torques, etc.) are obtained by the (negative) derivative of E_{Casimir} with respect to a distance (or angle) parameter. By this procedure, also any UV divergences of Eq. (3.15) are automatically removed and we can safely take the limit $\Lambda \rightarrow \infty$. Moreover, the interaction energy can thus be well defined even if the Casimir (self-)energy of a single surface is ill-defined in the ideal boundary-condition limit (“perfect conductivity”, infinitely thin surfaces, etc.) [66–70].

For the ideal limit of infinitely thin surfaces, the potential $V(\mathbf{x})$ becomes a δ function in space,

$$V(\mathbf{x}) = \lambda \int_{\Sigma} d\sigma \delta^{(d)}(\mathbf{x} - \mathbf{x}_{\sigma}). \quad (3.18)$$

The geometry of the Casimir configuration is defined by Σ , denoting a $d - 1$ dimen-

sional surface. The surface measure $d\sigma$ is assumed to be re-parametrisation invariant, and \mathbf{x}_σ denotes a vector pointing onto the surface. For a typical configuration, Σ consists of two disconnected objects (e.g., two disconnected plates), $\Sigma = \Sigma_1 \cup \Sigma_2$, with $\Sigma_1 \cap \Sigma_2 = \emptyset$. The positive coupling λ has mass dimension 1. In the ideal limit $\lambda \rightarrow \infty$, the potential imposes Dirichlet boundary conditions on the quantum field.

For the potential Eq. (3.18), the τ integral in the expectation value in Eq. (3.15) reads

$$I_\Sigma[\mathbf{x}(\tau)] := \int_0^T d\tau V(\mathbf{x}(\tau)) = \lambda \sum_{\{\tau_\sigma: \mathbf{x}(\tau_\sigma) \in \Sigma\}} \frac{1}{|\dot{\mathbf{x}}_\perp(\tau_\sigma)|}, \quad (3.19)$$

where the sum goes over all intersection points of the worldline $x(\tau_\sigma)$ and the surface Σ . In the denominator, $\dot{\mathbf{x}}_\perp(\tau_\sigma)$ denotes the component of the τ derivative perpendicular to the surface.

Computing the Casimir interaction energy Eq. (3.17) for two surfaces Σ_1 and Σ_2 , the argument of the expectation value in (3.15) becomes

$$\left(e^{-I_{\Sigma_1 \cup \Sigma_2}[\mathbf{x}(\tau)]} - 1 \right) - \left(e^{-I_{\Sigma_1}[\mathbf{x}(\tau)]} - 1 \right) - \left(e^{-I_{\Sigma_2}[\mathbf{x}(\tau)]} - 1 \right) \in [0, 1]. \quad (3.20)$$

Most importantly, Eq. (3.20) is nonzero only if the loop $\mathbf{x}(\tau)$ intersects both surfaces. In the Dirichlet limit $\lambda \rightarrow \infty$, this expression then equals one. Thus, for a massless scalar field with Dirichlet boundaries in $D = 3 + 1$, the worldline representation of the Casimir interaction energy boils down to [35, 53]

$$E_{\text{Casimir}} = -\frac{1}{2} \frac{1}{(4\pi)^2} \int_0^\infty \frac{dT}{T^3} \int d^3 x_{\text{CM}} \langle \Theta_\Sigma[\mathbf{x}(\tau)] \rangle_{\mathbf{x}}. \quad (3.21)$$

Here, the worldline functional $\Theta_\Sigma[\mathbf{x}(\tau)] = 1$ if the path $\mathbf{x}(\tau)$ intersects the surface $\Sigma = \Sigma_1 \cup \Sigma_2$ in both parts Σ_1 and Σ_2 , and $\Theta_\Sigma[\mathbf{x}(\tau)] = 0$ otherwise, analogous to the standard step function.

This compact formula has an intuitive interpretation: the worldlines can be viewed as the spacetime trajectories of the quantum fluctuations of the ϕ field. Any worldline that intersects the surfaces does not satisfy Dirichlet boundary conditions. All worldlines that intersect both surfaces thus should be removed from the ensemble of allowed fluctuations, thereby contributing to the negative Casimir interaction energy. One immediately realises the analogy to the mode selection process in conventional approaches, which we have explicitly performed for the parallel plates in chapter 2. However, compared to a field as profoundly non-local object, the one dimensional worldlines are remarkable simple objects, which allows for a comparatively easy

numerical evaluation.

The auxiliary integration parameter T , the so-called proptime, effectively governs the extent of a worldline in spacetime. Large T correspond to IR fluctuations with large worldlines, small T to UV fluctuations. Those T values for which the spatial extent of the worldlines is just big enough to intersect with both surfaces generically dominate the Casimir interaction energy. Within the worldline picture, it is already intuitively clear that for generic surfaces at a (suitably defined**) distance a the Casimir interaction energy for a Dirichlet scalar is negative and a monotonously increasing function of a ; therefore, the resulting force is always attractive in agreement with a recent theorem [71].

3.3 Worldline numerics

For the numerical evaluation of the expectation value Eq. (3.14), two discretisations are required: first, the path integral is approximated by a finite sum over an ensemble of n_L random paths $\mathbf{x}_\ell(\tau)$, $\ell = 1, \dots, n_L$, each of them forming a closed loop in space(-time). Second, the proptime which parametrises each path is discretised:

$$\mathbf{x}_\ell(\tau), \tau \in [0, T] \longrightarrow \mathbf{x}_{\ell k} := \mathbf{x}_\ell(k \cdot T/N), k = 1, \dots, N; \quad (3.22)$$

i.e., the paths themselves are represented by N points per loop (ppl). Thus, the ensemble is described by a two dimensional array of space vectors $(\mathbf{x}_{\ell k})$, with the indices ℓ and k specifying the loop and the point on the loop, respectively.

We generate the random paths using the *v-loop* algorithm [35]. This algorithm incorporates the Gaussian term $e^{-\frac{1}{4} \int_0^T d\tau \dot{\mathbf{x}}^2}$ as probability distribution, so that the path integral in Eq. (3.14) becomes an arithmetic mean:

$$\int_{\substack{\mathbf{x}(T)=\mathbf{x}(0), \\ \text{CM}}} \mathcal{D}\mathbf{x}(\dots) e^{-\frac{1}{4} \int_0^T d\tau \dot{\mathbf{x}}^2} \longrightarrow \frac{1}{n_L} \sum_{\ell=1}^{n_L} (\dots). \quad (3.23)$$

It is sufficient to generate only one so called *unit-loop* ensemble $(\mathbf{y}_{\ell k})$, i.e., an ensemble of loops with centre of mass $\mathbf{x}_{\text{CM}} = 0$ and $T = 1$. An ensemble with other values for

**A useful definition may be given by the following construction: let $a > 0$ be the maximally possible distance between two auxiliary parallel plates that can be placed in between the surfaces constituting the Casimir configuration without mutual intersection. This excludes pathological cases such as surfaces which are folded into each other. In this construction, it should also be understood that a change of a should not be accompanied by a rotation of one of the surfaces.

\mathbf{x}_{CM} and T is then simply obtained by computing

$$\mathbf{x}_{\ell k} = \mathbf{x}_{\text{CM}} + \sqrt{T} \mathbf{y}_{\ell k} \quad (3.24)$$

for all ℓ and k . At the same time, this technique provides for an analytic knowledge of the integrand's T dependence, which can be utilized for the T integration.

With this discretisation, the Casimir interaction energy Eq. (3.21) reads

$$E_{\text{Casimir}} = -\frac{1}{2} \frac{1}{(4\pi)^2} \int_0^\infty \frac{dT}{T^3} \int d^3x_{\text{CM}} \frac{1}{n_{\text{L}}} \sum_{\ell=1}^{n_{\text{L}}} \Theta_{\Sigma}[\mathbf{x}_{\text{CM}} + \sqrt{T} \mathbf{y}_{\ell}]. \quad (3.25)$$

The discretisation error is controlled by the two parameters n_{L} and N . The number of loops per ensemble n_{L} is related to a statistical error of the arithmetic mean in Eq. (3.23), which can be determined by jack-knife analysis. The number of points per loop N is chosen sufficiently large to achieve the desired precision by studying the convergence of the result. In this work, we have used ensembles with up to $n_{\text{L}} = 2.5 \cdot 10^5$ and $N = 4 \cdot 10^6$.

Let us emphasize that within the described discretisation spacetime is still treated as continuum, which is specifically advantageous for our studies of curvature and edge effects. To resolve the geometry of a smoothly curved or sharp-edged boundary with a discrete spacetime lattice, a tiny lattice spacing is required, demanding for a huge numerical effort. Consequently, in this context worldline numerics appears to be superior to conventional lattice computations.

Further advantages of worldline numerics are its scalability and its independence of the background (geometry). The computational effort scales only linearly with the parameters n_{L} , N , D , etc., and the algorithm can be formulated for any given background geometry. A disadvantage is that the statistical error decreases only with $1/\sqrt{n_{\text{L}}}$, as for any Monte-Carlo method. This implies that high-precision computations may require high statistics, in contrast to estimates with, say, a few-percent error which require very little computational effort.

For high-precision Casimir applications with an intended error of $\lesssim 0.1\%$, the CPU time needed for the evaluation of Eq. (3.25) can be reduced substantially by specializing the algorithm to the given Casimir geometry. Although this corresponds to a loss of generality, we believe that the strategies which we describe in the following, e.g., for the sphere-plate configuration, are examples for a general set of algorithmic tools which will be useful also for other Casimir configurations.

Chapter 4

Casimir curvature effects

We present worldline algorithms to examine the Casimir effect in a sphere-plate and cylinder-plate geometry for a fluctuating scalar field, obeying Dirichlet boundary conditions (“Dirichlet scalar”). We compute the Casimir interaction energies that give rise to forces between the rigid surfaces. This allows for a quantitative determination of validity bounds of approximation methods such as the PFA. We detail significant improvements of the numerical algorithms which facilitate high-precision calculations. Apart from numerical discretisation errors which are kept at or below the 0.1% level, no quantum-field-theoretic approximation is needed. Our results further strengthen the agreement with recently obtained analytic solutions for medium or larger curvature [38–40] and for small curvature [41]. The results of this chapter have been published in [53] and [54], the advanced worldline techniques we employ, in [72].

We emphasize that the Casimir energies for the Dirichlet scalar should generally not be taken as an estimate for those for the electromagnetic (EM) field, leaving especially the experimentally most used sphere-plate case as a pressing open problem. Nevertheless, a comparison with other techniques can meaningfully be performed, and the validity constraints that we derive, e.g., for the PFA hold independently of the type of boundary condition, since the PFA approach makes no reference to the nature of the fluctuating field. If an experiment is performed outside the PFA validity ranges determined below, any comparison of the data with theory using the PFA has no firm basis.

4.1 Introduction

Apart from only a few exceptions [26], most of the current efforts to measure the Casimir force do not employ parallel plates at all, but curved geometries such as spheres [3] and cylinders [73]. At first glance this is surprising and appears to be counterproductive for the following reason: The Casimir force is comparatively weak but scales linearly with the size of the plates. Using huge plates would result in a macroscopic manifestation of this force. By contrast, for the curved geometries the area where the boundaries are close to each other is much smaller, resulting in a much weaker attraction. But in practice, this drawback is outweighed by another practical consideration. Keeping two plates parallel at a distance on the nanometre scale is an enormous challenge, resulting in experimental errors which are in general significantly larger than for the curved geometries.

However, for the curved geometry experiments the insufficient theoretical understanding of the Casimir effect's geometry dependence means a lack of theoretical reference. In general one has to resort to the proximity force approximation. At this point the worldline-numeric approach presented in the previous chapter, chapter 3, comes into play. Its formulation is intrinsically independent of the Casimir geometry, therefore it is predestined to study geometries inaccessible to other approaches.

The procedure outlined in chapter 3 could be implemented straightforwardly, but the corresponding CPU time can be reduced dramatically by adjusting the algorithms to the given geometry. This will be demonstrated in the present chapter for the sphere-plate and for the cylinder-plate geometry. Also for the edge configurations in the next chapter we will use specialised, profoundly simplified algorithms. Self-evidently, the specialisations correspond to a loss of generality, but we believe that the specialisation strategies are conferable to other Casimir problems as well.

The general structure of a worldline algorithm for computing Casimir interaction energies is summarized by Eq. (3.25). The only part of the algorithm that depends on the geometry consists of a diagnostic routine which checks whether a given loop (for given \mathbf{x}_{CM} and T) intersects with (more than one of) the surfaces $\Sigma_1, \Sigma_2, \dots$. The result of this diagnostic routine immediately translates into the form of either the T or \mathbf{x}_{CM} integrand, depending on the actual order of integration. If the T integral is done first, the resulting loop-averaged \mathbf{x}_{CM} integrand can be viewed as the interaction energy density, the calculation of which is already an instructive intermediate step.* In principle, the T and \mathbf{x}_{CM} integration as well as the average over all worldlines can

*The \mathbf{x}_{CM} integrand actually corresponds to a static effective-action density in the present case. The relation to the true interaction energy density which corresponds to the 00 component of the interaction energy-momentum tensor is give by a total derivative [50, 74].

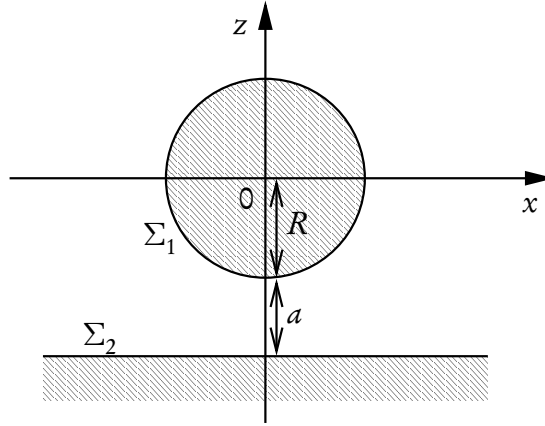


Figure 4.1: Geometry of the sphere-plate configuration

be done in arbitrary order, depending on numerical convenience.

There is, however, an important technical difference between taking the worldline average before or after the integrations. The apparent advantage of doing the worldline average first is that the resulting T and \mathbf{x}_{CM} integrands are smooth, despite the fact that the worldlines are fractal; this was exploited in many worldline numerical applications so far. In the present work, we nevertheless do the loop average at a later step. As a consequence, the resulting integrands can become complicated in the sense that the support of the integrand is a piecewise disconnected set. However, once the support is determined by special algorithms, at least one integral can be done analytically, since the integrand $\sim \Theta_{\Sigma} = 1$ and thus is extremely simple on the support. This leads to significant numerical acceleration, constituting the basic new ingredient of our improved algorithms.

4.2 Sphere above plate

The geometry of the sphere-plate configuration is illustrated in Fig. 4.1. It is rotationally symmetric with respect to the z axis, therefore the three dimensional \mathbf{x}_{CM} integration in Eq. (3.25) trivially reduces to a two dimensional integration. We choose the following order of remaining integrations/summations: first, we do the T integral for each worldline; then, we take the average over all loops, and finally integrate over the resulting energy density. For the first step, the numerically most challenging task is to determine the support \mathcal{S}_{ℓ} of $\Theta_{\Sigma}[\mathbf{x}_{\text{CM}} + \sqrt{T}\mathbf{y}_{\ell}]$ on the T axis to perform the T integration in Eq. (3.25). In the given geometry, $\Theta_{\Sigma}[\mathbf{x}_{\text{CM}} + \sqrt{T}\mathbf{y}_{\ell}]$ equals 1 if there exists a pair k, l , such that $\mathbf{x}_{\text{CM}} + \sqrt{T}\mathbf{y}_{\ell k}$ lies inside the sphere and $\mathbf{x}_{\text{CM}} + \sqrt{T}\mathbf{y}_{\ell l}$ lies

below the plate; otherwise it is zero.** To investigate the support \mathcal{S}_ℓ , it turns out to be useful to distinguish between \mathbf{x}_{CM} lying inside the sphere, $\mathbf{x}_{\text{CM}}^2 \leq R^2$, and \mathbf{x}_{CM} lying outside, $\mathbf{x}_{\text{CM}}^2 > R^2$, as the former case is much simpler than the latter.

4.2.1 Inside

Inside the sphere, the support \mathcal{S}_ℓ is a single T interval. The lower bound T_ℓ^{min} is given by the T value at which the loop $\mathbf{x}_{\text{CM}} + \sqrt{T}\mathbf{y}_\ell$ touches the plate,

$$T_\ell^{\text{min}} = \left(\frac{R + a + x_{\text{CM}z}}{\min_k y_{\ell kz}} \right)^2, \quad (4.1)$$

where $\min_k y_{\ell kz}$ is the minimal z coordinate of the unit loop \mathbf{y}_ℓ . The upper bound T_ℓ^{max} is the largest T value for which the loop intersects the sphere,

$$T_\ell^{\text{max}} = \max \left\{ T : \exists_k (\mathbf{x}_{\text{CM}} + \sqrt{T}\mathbf{y}_{\ell k})^2 = R^2 \right\} \quad (4.2)$$

$$= \max_k \left(-\frac{\mathbf{x}_{\text{CM}} \cdot \mathbf{y}_{\ell k}}{y_{\ell k}^2} + \sqrt{\left(\frac{\mathbf{x}_{\text{CM}} \cdot \mathbf{y}_{\ell k}}{y_{\ell k}^2} \right)^2 - \frac{\mathbf{x}_{\text{CM}}^2 - R^2}{y_{\ell k}^2}} \right)^2. \quad (4.3)$$

Performing the T integration, we obtain the Casimir interaction energy density $\varepsilon_{\text{Casimir}}$ inside the sphere, $E_{\text{Casimir}} = \int d^3x_{\text{CM}} \varepsilon_{\text{Casimir}}$,

$$\varepsilon_{\text{Casimir}}(\mathbf{x}_{\text{CM}}) = \frac{1}{64\pi^2} \frac{1}{n_L} \sum_{\ell=1}^{n_L} \left(\frac{1}{(T_\ell^{\text{max}})^2} - \frac{1}{(T_\ell^{\text{min}})^2} \right) \cdot \theta(T_\ell^{\text{max}} - T_\ell^{\text{min}}), \quad (4.4)$$

where the θ function takes care of the (non-generic) case that the loop never intersects both surfaces. This quantity is plotted in the contour plot Fig. 4.2 in the region inside the white circle. The contribution to the total Casimir interaction energy is small compared to the energy outside the sphere. The density of the latter is shown in the same figure outside the circle, obtained by the procedure described next.

**Strictly speaking, this criterion misses the rare case that the link between two neighbouring points which are both outside the sphere intersects the sphere. We neglect these contributions, since the verification of this pattern is much more time-consuming than simply increasing the amount of points per loop to reduce the corresponding systematic error.

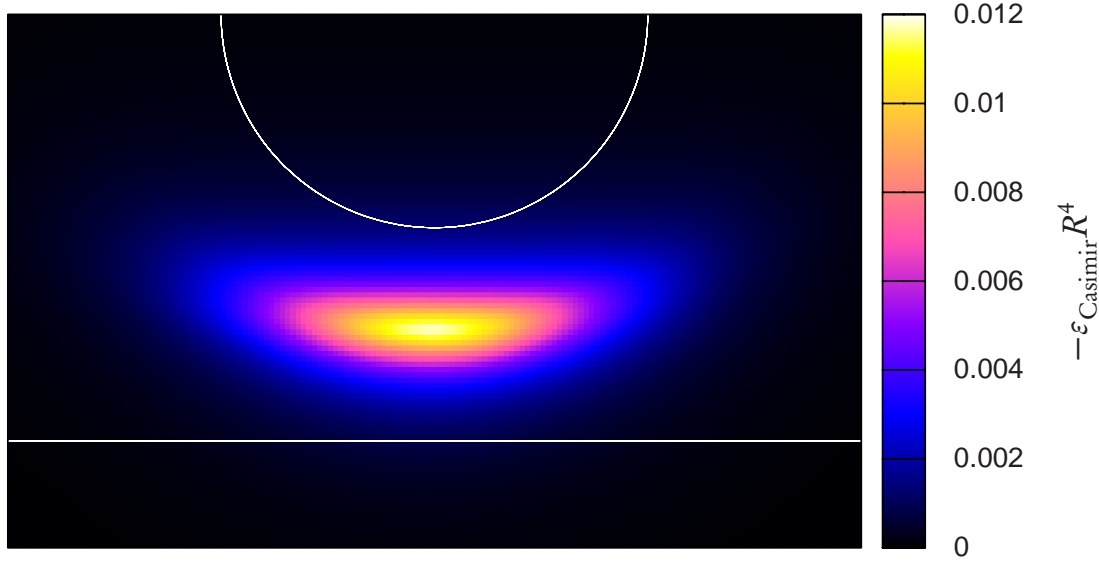


Figure 4.2: Contour plot of the negative Casimir interaction energy density $\varepsilon_{\text{Casimir}}$ for a sphere of radius R above an infinite plate; the sphere-plate separation a has been chosen as $a = R$ here.

4.2.2 Outside

Outside the sphere the support \mathcal{S}_ℓ is not merely one single interval as in the previous case, but a whole set of successive intervals. As illustrated in Fig. 4.3, for a unit loop \mathbf{y}_ℓ at a centre of mass \mathbf{x}_{CM} outside the sphere, the ray $\mathbf{x}_{\text{CM}} + \sqrt{T}\mathbf{y}_{\ell k}$ does not pierce the sphere for most indices k . The corresponding points on the loop are not relevant for the Casimir energy and the first step in our algorithm is to sort them out. Two conditions are evaluated for this purpose: a point $\mathbf{y}_{\ell k}$ is only relevant for further computations if

1. the vector $\mathbf{y}_{\ell k}$ points towards the sphere, implying

$$\mathbf{x}_{\text{CM}} \cdot \mathbf{y}_{\ell k} < 0, \quad (4.5)$$

2. the distance b between the ray $\mathbf{x}_{\text{CM}} + \sqrt{T}\mathbf{y}_{\ell k}$ and the centre of the sphere is smaller than the radius R ,

$$b^2 = \mathbf{x}_{\text{CM}}^2 - \left(\mathbf{x}_{\text{CM}} \cdot \frac{\mathbf{y}_{\ell k}}{|\mathbf{y}_{\ell k}|} \right)^2 < R^2. \quad (4.6)$$

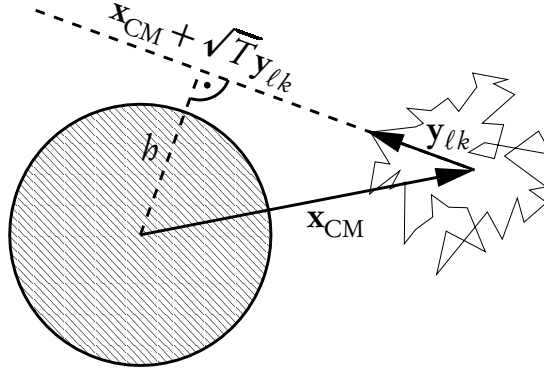


Figure 4.3: For any proptime T , the ray $\mathbf{x}_{\text{CM}} + \sqrt{T}\mathbf{y}_{\ell k}$ does not intersect the sphere. The corresponding point $\mathbf{y}_{\ell l}$ is thus not relevant for the interaction energy density at the given \mathbf{x}_{CM} and consequently sorted out in a first step of the algorithm.

If these conditions are fulfilled, the T values at which the ray intersects the sphere are determined by

$$(\mathbf{x}_{\text{CM}} + \sqrt{T}\mathbf{y}_{\ell k})^2 = R^2, \quad (4.7)$$

which has the solutions

$$T_{\ell k}^{\pm} = \left(-\frac{\mathbf{x}_{\text{CM}} \cdot \mathbf{y}_{\ell k}}{y_{\ell k}^2} \pm \sqrt{\left(\frac{\mathbf{x}_{\text{CM}} \cdot \mathbf{y}_{\ell k}}{y_{\ell k}^2} \right)^2 - \frac{\mathbf{x}_{\text{CM}}^2 - R^2}{y_{\ell k}^2}} \right)^2. \quad (4.8)$$

For $T \in [T_{\ell k}^-, T_{\ell k}^+]$ the point $\mathbf{x}_{\text{CM}} + \sqrt{T}\mathbf{y}_{\ell k}$ lies inside the sphere and consequently we know that the loop intersects the sphere. For a given loop, the total set of T values for which this is the case is the union of the intervals $[T_{\ell k}^-, T_{\ell k}^+]$ of all points $\mathbf{y}_{\ell k}$ in the unit loop, $\bigcup_k [T_{\ell k}^-, T_{\ell k}^+]$. Taking into account the minimal T value for which the loop intersects the plate, T_{ℓ}^{min} , the contribution of the unit loop to the proptime integrand has the support

$$\mathcal{S}_{\ell} = [T_{\ell}^{\text{min}}, \infty) \cap \bigcup_k [T_{\ell k}^-, T_{\ell k}^+]. \quad (4.9)$$

The set union can be determined efficiently by use of a sorting algorithm like *quicksort*, for example. Once \mathcal{S}_{ℓ} is determined, the T integration can be performed analytically. The worldline estimate for the Casimir interaction energy density outside the sphere therewith is

$$\varepsilon_{\text{Casimir}}(\mathbf{x}_{\text{CM}}) = -\frac{1}{32\pi^2} \frac{1}{n_{\text{L}}} \sum_{\ell=1}^{n_{\text{L}}} \int_{\mathcal{S}_{\ell}} \frac{dT}{T^3}, \quad (4.10)$$

which is plotted in Fig. 4.2 outside the white circle.

4.2.3 Optimization

The algorithm so far works well if the distance between sphere and plate a is of the same order of magnitude as the sphere's radius R , $a \approx R$. To improve the accuracy by increasing the number of loops n_L and the number of points per loop N , the algorithm can be parallelised as *embarrassingly parallel computation* by dividing the loop ensemble into independently processed sub-ensembles. However, if the two scales a and R differ significantly in size, additional improvements of our algorithm are advisable.

Large distances ($a \gg R$): if the distance a is large compared to the radius R , the algorithm described so far becomes inefficient due to the following reason: only loops with a minimal extent of the same order of magnitude as the distance between sphere and plate do contribute to the Casimir energy. For a loop $\mathbf{x}_{\text{CM}} + \sqrt{T}\mathbf{y}_\ell$ this means, that the unit loop \mathbf{y}_ℓ has to be scaled by a large factor \sqrt{T} . This implies that the distance between subsequent points on the loop increases, too. However, to ensure that the scaled loops still resolve the sphere, this distance should be significantly smaller than the sphere's radius. Thus, the number of points per loop N has to be increased with increasing a/R .

A rough measure for the extent of a loop is the variance of the coordinates of its points. The ensemble average of the variance for large N is $\langle (\sqrt{T}\mathbf{y}_{\ell k})^2 \rangle = T/6$. As a consequence we expect the T integral to be dominated by $T \approx 6a^2$, also because the contribution for large T is damped by the $1/T^3$ factor. The root-mean-square of the distance between two subsequent points on a loop for large N is $\sigma = \sqrt{2T/N}$. Using the dominating T value we obtain $\sigma \approx 2\sqrt{3/N}a$. We demand this value to be much smaller than the radius of the sphere, which implies $N \gg 12a^2/R^2$. For a distance $a = 10R$, already much more than 1000 ppl have to be used, for $a = 100R$ much more than 100 000 ppl.

A slight modification enables our algorithm to cope with this high resolution and the corresponding amount of data much more efficiently. So far, for all centre of masses \mathbf{x}_{CM} with a common z coordinate $\mathbf{x}_{\text{CM}z}$, the first interval on the right-hand side of Eq. (4.9), $[T_\ell^{\min}, \infty)$, is the same, which can be utilized to speed up the calculation. In contrast, the union in the same equation is different for all centres of masses. However, it is this part of the equation which consumes most of the CPU time. Modifying the transformation Eq. (3.24) reverses the circumstances: let us define the rotation

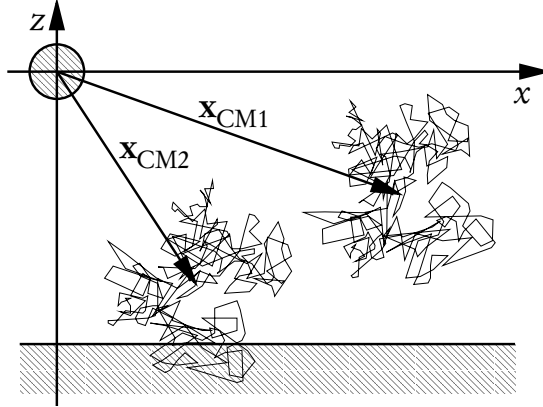


Figure 4.4: Sketch of a unit loop at different centres of masses x_{CM1} and x_{CM2} , as used for large a/R . The unit loop is rotated corresponding to the orientation of the centre of mass.

$R(\mathbf{x}_{CM}, \mathbf{e}_z)$ by $\mathbf{x}_{CM}/|\mathbf{x}_{CM}| = R(\mathbf{x}_{CM}, \mathbf{e}_z)\mathbf{e}_z$. By using

$$\mathbf{x}_{\ell k} = \mathbf{x}_{CM} + \sqrt{T}R(\mathbf{x}_{CM}, \mathbf{e}_z)\mathbf{y}_{\ell k} \quad (4.11)$$

(see Fig. 4.4), the union in Eq. (4.9) is the same for all centre-of-mass values x_{CM} with a given absolute value $|\mathbf{x}_{CM}|$ and can be computed once and for all. In turn, T_ℓ^{\min} is no longer degenerate with respect to some \mathbf{x}_{CM} coordinate. The important advantage is that this dependence can be computed much faster. For each loop, we generate an array of its minimal z coordinate as function of the angle between \mathbf{x}_{CM} and \mathbf{e}_z . The bound T_ℓ^{\min} then results from Eq. (4.1), where the minimum is read from the array. Note that the transformation (4.11) is a legitimate symmetry operation for ensemble-averaged quantities, owing to the rotational invariance of the exponential weight factor in Eq. (3.23).

There is a price to be paid for the desired feature of having a common set union in Eq. (4.9) for different centres of masses x_{CM} : without the transformation, all points of a given unit loop are equally involved in scanning the curvature of the sphere. With the transformation, always the same points of a unit loop are close to the sphere, independently of \mathbf{x}_{CM} . This corresponds to a loss of statistics, implying a slight increase of the statistical errors. However, this is by far compensated for by the gain in computation speed, which enables us to significantly reduce again the statistical error by brute force.

Small distances ($a \ll R$): the main contribution of the Casimir interaction energy density is localized between sphere and plate. If the distance a is much smaller than the sphere's radius R , the lower bound of the support \mathcal{S}_ℓ in that region is at very

small T values compared to the upper bound of the support's first interval. Since the T integrand falls off rapidly with $1/T^3$, the T integral is dominated by this lower bound. Therefore, a very good estimate is given by replacing \mathcal{S}_ℓ simply by the interval $[T_\ell^{\min}, \infty)$, resulting in

$$\varepsilon_{\text{Casimir}}(x_{\text{CM}}) \simeq -\frac{1}{64\pi^2} \frac{1}{n_L} \sum_{\ell=1}^{n_L} \frac{1}{(T_\ell^{\min})^2}. \quad (4.12)$$

In particular outside the sphere, the numerical evaluation of this expression is much faster than the evaluation of the full expression Eq. (4.10).

For a rough estimate of the validity range of this approximation, we use the ensemble's standard deviation of the point position, $\langle (\sqrt{T} \mathbf{y}_{\ell k})^2 \rangle = T/6$, to estimate the extent of a loop. Right between sphere and plate, where the energy density is largest, the lower bound of the proptime integral then is approximately $T_\ell^{\min} \approx 3a^2/2$. If the extent of the loop increases beyond $a/2 + 2R$, we expect the loop to intersect the sphere no longer for $T_1 \gtrsim 6(a/2 + 2R)^2$. By setting the value of T_1 to infinity instead, as done in Eq. (4.12), we introduce a systematic error $\Delta\varepsilon_{\text{Casimir}}/\varepsilon_{\text{Casimir}} \lesssim (1 + 4R/a)^{-4}$. For distances a smaller than $0.8R$ this error is smaller than one per mille. In this work, we have used Eq. (4.12) to compute high-precision values for $a < 0.02R$.

4.2.4 Results

Figure 4.5 presents a global view on the Casimir interaction energy for a wide range of the curvature parameter a/R ; the energy is normalized to the zeroth order of the PFA formula, $E_{\text{PFA}}^{(0)} := E_{\text{SP}}^{\text{PFA}}(a/R \ll 1)$, Eq. (A.6). For small a/R ("large spheres"), our worldline result (crosses with error bars) and the full sphere- and plate-based PFA estimates (dashed-dotted lines) show reasonable agreement, settling at the zeroth-order PFA $E_{\text{PFA}}^{(0)}$. The full PFA departs on the percent level from $E_{\text{PFA}}^{(0)}$ for $a/R \gtrsim 0.01$, exhibiting a relative energy decrease. By contrast, our worldline result first stays close to $E_{\text{PFA}}^{(0)}$ and then increases towards larger energy values relative to $E_{\text{PFA}}^{(0)}$. This observation confirms earlier worldline studies [35] and agrees with the optical approximation [36, 37] in this curvature regime.

For larger curvature $a/R \gtrsim 0.1$ ("smaller spheres"), we observe a strong increase relative to $E_{\text{PFA}}^{(0)}$ [53]. Here, our data satisfactorily agrees with the exact solution found recently for this regime [38, 39] (dashed line). The latter work also provides for an exact asymptotic limit for $a/R \rightarrow \infty$, resulting in $180/\pi^4$ for our normalization. Our worldline data confirms this limit in Fig. 4.5.

Two important lessons can be learned from this plot: first, the PFA already fails to

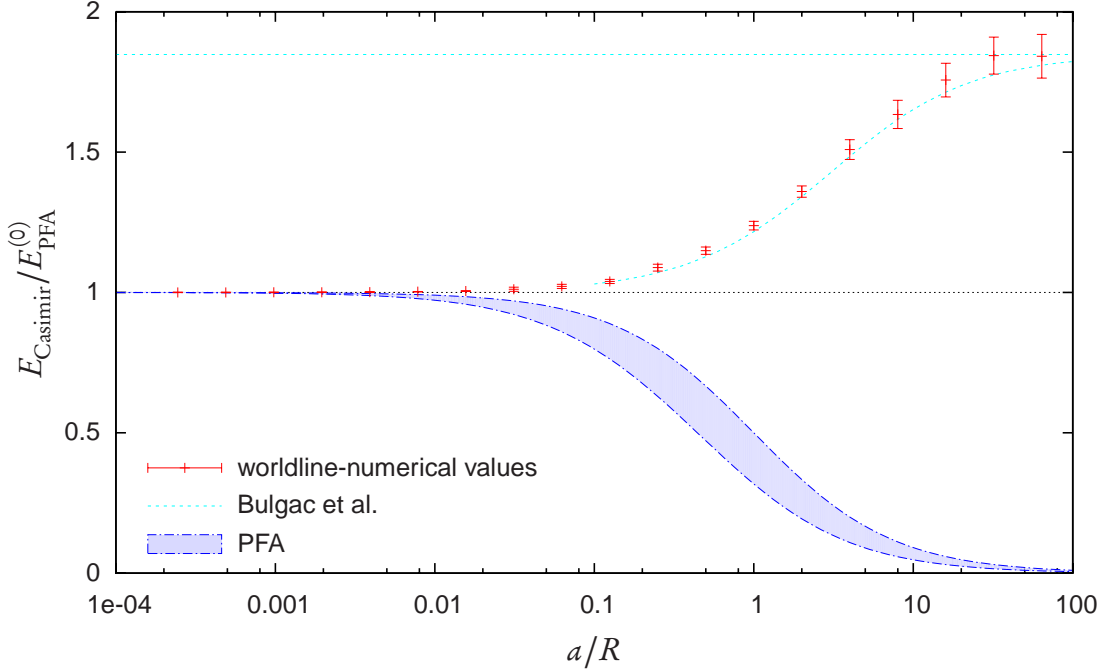


Figure 4.5: Casimir interaction energy of a sphere with radius R and an infinite plate vs. the curvature parameter a/R . The energy is normalized to the zeroth-order PFA formula Eq. (A.6), $E_{\text{PFA}}^{(0)}$. For larger curvature parameter, the PFA estimate (dot-dashed line) differs qualitatively from the worldline result (crosses with error bars). Here, we observe good agreement of our result with the exact solution of [38, 39] which is available for $a/R \gtrsim 0.1$ (dashed line).

predict the correct sign of the curvature effects beyond zeroth order, see also [75]. Second, the relation between the Casimir effect for Dirichlet scalars and that for the EM field is strongly geometry dependent. For the parallel-plate case, Casimir forces only differ by the number of degrees of freedom, cf. the coefficient c_{pp} in Eq. (A.3). For large curvature, the Casimir energy for the Dirichlet scalar scales with a^{-2} , whereas that for the EM field obeys the Casimir-Polder law $\sim a^{-4}$ [56, 76]. Already this difference demonstrates that simple approximation methods such as the PFA are highly problematic, since no reference to the nature of the fluctuating field other than the coefficient c_{pp} is made.

For a quantitative determination of the PFA validity limits, Fig. 4.6 displays the zeroth-order normalized energy for small curvature parameter a/R . Here, our result has an accuracy of 0.1% (jack-knife analysis). The error is dominated by the Monte Carlo sampling and the ordinary-integration accuracy; the error from the worldline discretisation is found negligible in this regime, implying a sufficient proximity to the continuum limit.

In addition to our numerical error band, we consider the region between the sphere-

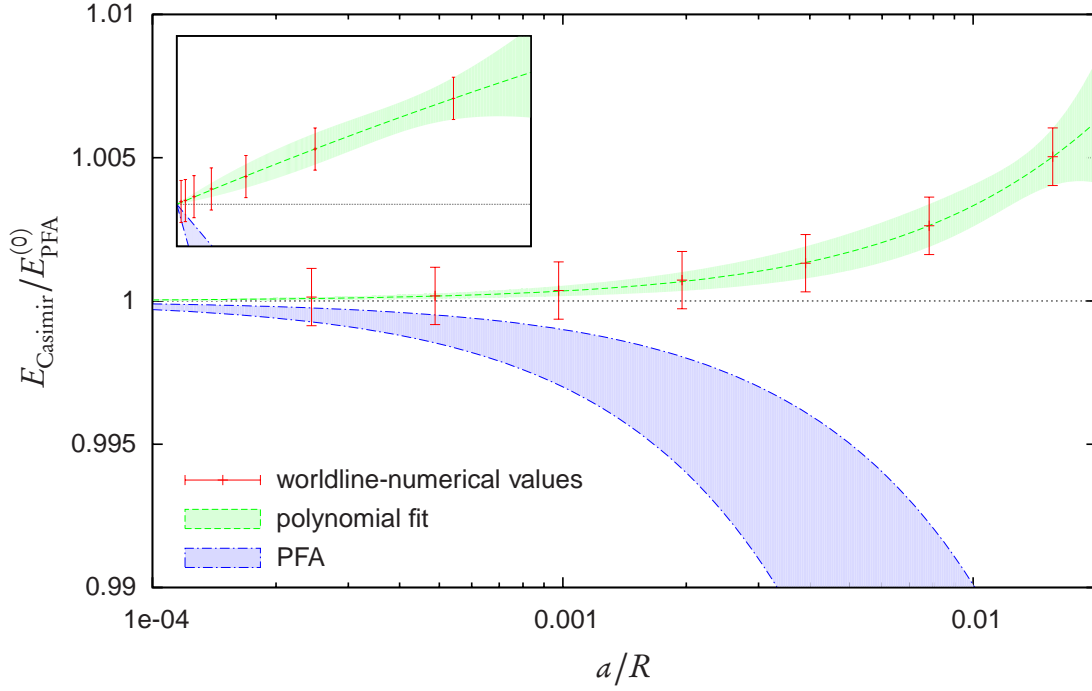


Figure 4.6: Magnified view of Fig. 4.5 for small a/R . The 0.1% validity range of the PFA is characterized by curvature parameters, where the error band of our worldline results and the PFA band (blue-shaded/in between the dot-dashed lines) overlap, see Eq. (4.13). The dashed line depicts a constraint polynomial fit of the worldline result, $p(a/R) = 1 + 0.35(a/R) - 1.92(a/R)^2$, and its standard deviation, see Eq. (4.15). The inlay displays the same curves with a linear a/R axis.

and the plate-based PFA as the PFA error band. We identify the 0.1% accuracy limit of the PFA with the curvature parameter $a/R|_{0.1\%}$ where the two bands do no longer overlap. We obtain

$$\frac{a}{R} \Big|_{0.1\%}^{\text{PFA}} \leq 0.00073 \quad (4.13)$$

as the corresponding validity range for the curvature parameter. For instance, for a typical sphere with $R = 200\mu\text{m}$ and an experimental accuracy goal of 0.1%, the PFA should not be used for $a \gtrsim 150\text{nm}$. We conclude that the PFA should be dropped from the analysis of future experiments.

For the 1% accuracy limit of the PFA, we increase the band of our worldline estimate by this size and again determine the curvature parameter for which there is no intersection with the PFA band any more. We obtain

$$\frac{a}{R} \Big|_{1\%}^{\text{PFA}} \leq 0.00755. \quad (4.14)$$

For a sphere with $R = 200\mu\text{m}$ and an experimental accuracy goal of 1%, the PFA holds for $a < 1.5\mu\text{m}$. This result confirms the use of the PFA for the data analysis of the corresponding experiments performed so far.

In order to study the asymptotic expansion of the normalized energy, we fit our worldline numerical data to a second-order polynomial for $a/R < 0.1$ and include the exactly known result for $a/R \rightarrow 0$. We obtain

$$E_{\text{WN data fit}}^{\text{sphere-plate}} = -c_{\text{PP}} \frac{\pi^3 R}{1440 a^2} \times \left(1 + 0.35 \frac{a}{R} - 1.92 \frac{a^2}{R^2} \pm 0.19 \frac{a}{R} \sqrt{1 - 137.2 \frac{a}{R} + 5125 \frac{a^2}{R^2}} \right), \quad (4.15)$$

valid for $a/R < 0.1$; here, $c_{\text{PP}} = 1$ for the real and $c_{\text{PP}} = 2$ for a complex Dirichlet scalar. The fit result is plotted in Fig. 4.6 (dashed lines), which illustrates that $E \simeq E_{\text{WN data fit}}$ is a satisfactory approximation to the Casimir energy for $a/R < 0.1$, replacing the PFA (A.7). The inlay of Figure 4.6 displays the same curves with a linear a/R axis, illustrating that the lowest-order curvature effect is linear in a/R . A more direct result for the linear curvature coefficient can be obtained by a constraint linear fit; in this simpler case, the fit polynomial yields $p_{\text{fit}}(a/R) = 1 + (0.33 \pm 0.06) \frac{a}{R}$ instead of the expression in parentheses in Eq. (4.15). Given the results of the PFA (A.7), the semiclassical approximation [29, 30], $p_{\text{sc}}(a/R) \simeq 1 - 0.17 \frac{a}{R}$, cf. [38, 39], and the optical approximation [36, 37], $p_{\text{opt}}(a/R) \simeq 1 + 0.05 \frac{a}{R}$, the latter appears to estimate curvature effects more appropriately; but all these approximations are not quantitatively reliable for beyond-zeroth-order curvature effects.

4.3 Cylinder above plate

The cylinder-plate configuration is a promising tool for high-precision experiments [77], since the force signal increases linearly with the cylinder length. The numerics is very similar to the sphere-plate configuration, even less computing power is required, because only two dimensional loops have to be processed due to the translational symmetry. Figure 4.7 shows the corresponding Casimir interaction energy versus the curvature parameter. The energy axis is again normalized to the zeroth-order PFA result, Eq. (A.10) [78]

$$E_{\text{PFA}}^{(0)}(a, R) := E_{\text{CP}}^{\text{PFA}}(a/R \ll 1) = -c_{\text{PP}} \frac{\pi^3}{1920\sqrt{2}} \frac{R^{1/2}}{a^{5/2}}. \quad (4.16)$$

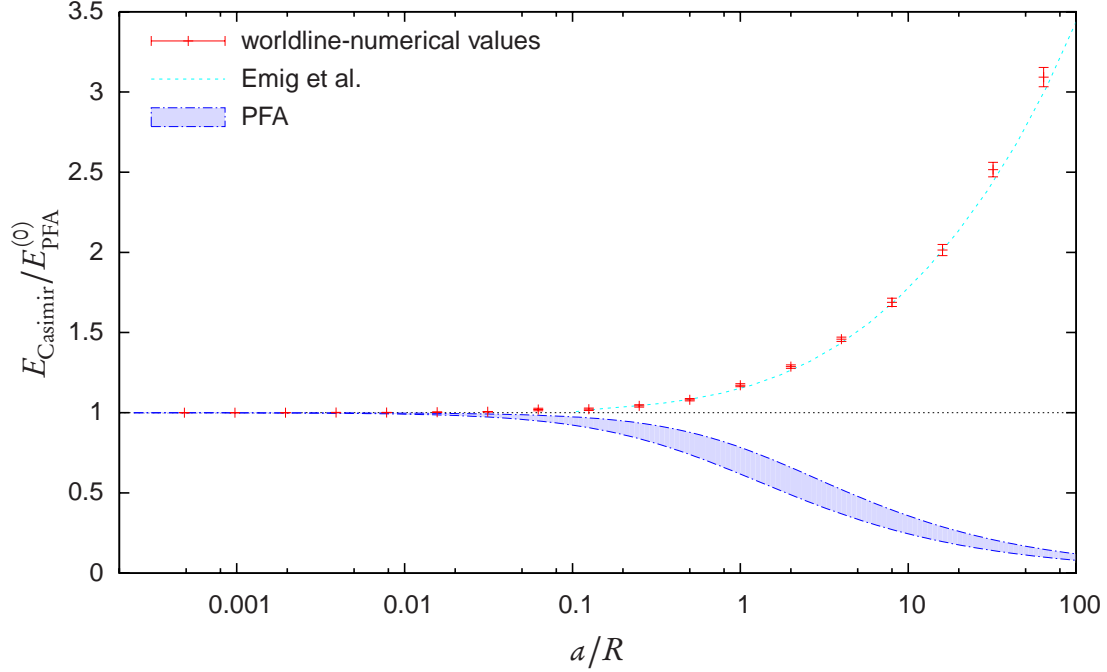


Figure 4.7: Casimir interaction energy (normalized to $E_{\text{PFA}}^{(0)}$) of an infinitely long cylinder with radius R at a distance a above an infinite plate vs. the curvature parameter a/R . We observe good agreement of our result with the exact solution of [40] which is available for $a/R \gtrsim 0.1$ (dashed line).

A magnified view of the small curvature region in Fig. 4.7 is shown in Fig. 4.8. As for the sphere-plate configuration, we fit our data to a second-order polynomial in this range, including the exactly known result for $a/R \rightarrow 0$, yielding

$$E_{\text{WN data fit}}^{\text{cylinder-plate}} = -\frac{c_{\text{PP}}\pi^3}{1920\sqrt{2}} \frac{R^{1/2}}{a^{5/2}} \times \left(1 + 0.21\frac{a}{R} - 0.66\frac{a^2}{R^2} \pm 0.097\frac{a}{R} \sqrt{1 - 68.60\frac{a}{R} + 1282\frac{a^2}{R^2}} \right), \quad (4.17)$$

for $a/R < 0.1$. The inlay of Fig. 4.8 shows the same data with a linear a/R axis. As for the sphere-plate geometry, this plot demonstrates that the lowest-order curvature effect is linear in a/R . A simpler linear fit to our data results in $p_{\text{fit}}(x) \simeq 1 + (0.195 \pm 0.028)\frac{a}{R}$. This is in remarkable agreement with the recently found analytical result $p(a/R) = 1 + 0.194\frac{a}{R} + \mathcal{O}(a^2/R^2)$ [41], which represents a strong confirmation for both methods.

The qualitative conclusions for the validity of the PFA are similar to that for the

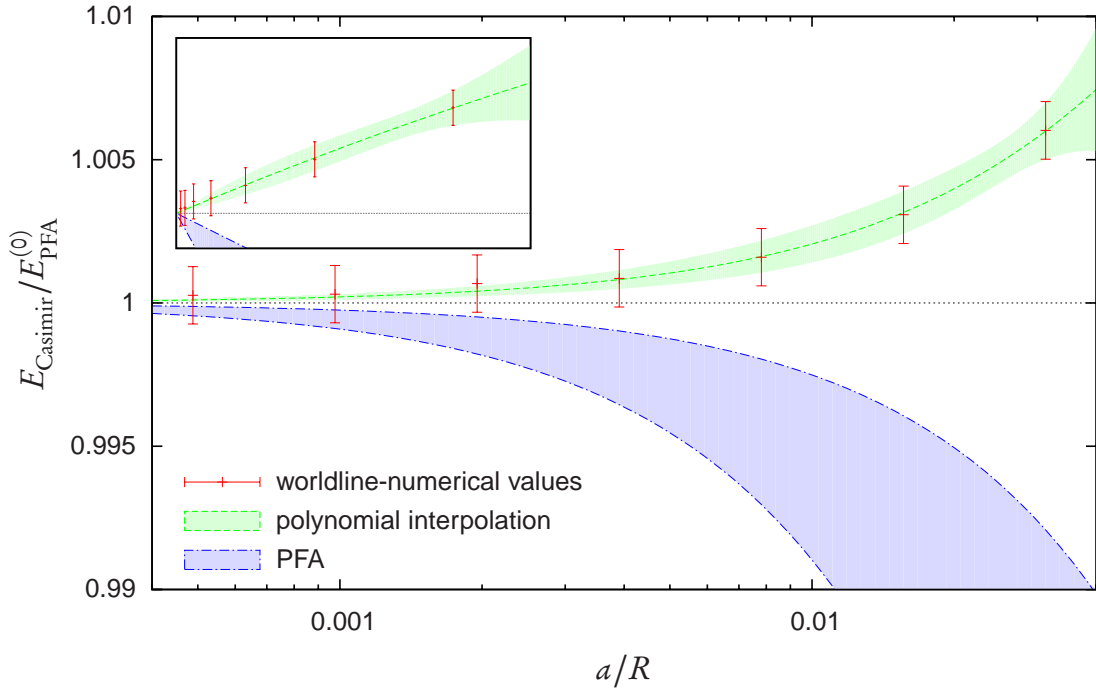


Figure 4.8: Magnified view of Fig. 4.7 for small values of a/R . The dashed line with error band depicts a constraint polynomial fit to the numerical data, $p(a/R) = 1 + 0.21(a/R) - 0.66(a/R)^2$, and its standard deviation. The inlay displays the same curves with a linear a/R axis.

sphere above a plate: beyond leading order, the PFA even predicts the wrong sign of the curvature effects. Quantitatively, the PFA validity limits are a factor ~ 3 larger than Eqs. (4.13),(4.14), owing to the absence of curvature along the cylinder axis. The most important difference to the sphere-plate case arises for large a/R . Here, the data is compatible with a log-like increase relative to $E_{\text{PFA}}^{(0)}$, implying a surprisingly weak decrease of the Casimir force for large curvature $a/R \rightarrow \infty$. Our result agrees nicely with the recent exact result [40] which is available for $a/R \gtrsim 0.1$. The data thus confirms the observation of [40] that the resulting Casimir force has the weakest possible decay, $F \sim 1/[a^3 \ln(a/R)]$, for asymptotically large curvature parameter $a/R \rightarrow \infty$.

Chapter 5

Casimir edge effects

In this chapter, we compute Casimir forces in open geometries with edges, involving parallel as well as perpendicular semi-infinite plates. We focus on Casimir configurations which are governed by a unique dimensional scaling law with a universal coefficient* as it is the case for the parallel-plate configuration. Even though this configuration does not involve any edges, we will revisit this classic example, too, first because our algorithmic strategies can easily be illustrated here; and second, we thereby obtain a mapping between the D dimensional Casimir effect and characteristic properties of a random-chain polymer ensemble (say, in 3 space dimensions), due to the use of path integrals in the worldline method [72].

With the aid of worldline numerics, we determine the universal coefficients for various geometries for the case of scalar-field fluctuations with Dirichlet boundary conditions (“Dirichlet scalar”). As in the previous chapter our results do not apply directly for Casimir configurations probing the electromagnetic fluctuation field, the results for the universal coefficients may quantitatively differ, but our values can be used for an order-of-magnitude estimate of the error induced by edges of a finite configuration, thus providing an important ingredient for the data analysis of future experiments. The Casimir edge effects for finite parallel plates, for instance, can be reformulated as an increase of the effective area of the configuration. In addition, our results can directly be applied to Casimir configurations in ultracold-gas systems [79] where massless scalar fluctuations exist near the phase transition.

The results of this chapter can be found in [80]. The details of our calculations are still unpublished and will therefore be described at length in the following.

*While this is no necessity for our computational method, the results for these special cases give rise to a better qualitative understanding of edge effects

5.1 Introduction

Casimir's prediction for the force F per unit area A between two perfectly conducting infinite parallel plates at a distance a [1] has the remarkable property, that a straightforward dimensional analysis already fixes the powers of \hbar , c , and a uniquely: Using \hbar as unit for actions we can write

$$\hbar = [S] = [tE] = [tFl], \quad (5.1)$$

where l denotes an arbitrary length. With c as unit speed, $[l/t] = c$, we obtain

$$\left[\frac{F}{l^2} \right] = \frac{\hbar c}{[l]^4} \quad (5.2)$$

and thus for the parallel plates the Casimir force per unit area has the units

$$\left[\frac{F_{\parallel}}{A} \right] = \frac{\hbar c}{[l]^4}. \quad (5.3)$$

In other words,

$$\frac{F_{\parallel}}{A} = \gamma_{l,\text{par.}} \frac{\hbar c}{l^4} \quad (5.4)$$

where the length l is arbitrary, but has to be considered by the choice of the dimensionless quantity $\gamma_{l,\text{par.}}$, which also depends on the parameters describing the configuration. With the choice $l = a$ and exploiting that a is the only parameter, the factor may only depend on the distance a , $\gamma_{l,\text{par.}} = \gamma_a$. But as γ_a is a pure number, in contrast to the length a , we reason that it is even independent of a and thus a constant, pure number. By convention we denote this number by $-\gamma_{\parallel}$ and end up with the expression

$$\frac{F_{\parallel}}{A} = -\gamma_{\parallel} \frac{\hbar c}{a^4}. \quad (5.5)$$

Except for the still unspecified constant γ_{\parallel} , this is already Casimir's classic result Eq. (2.18).

We conclude: In absence of any other dimensionful quantity, the effects of quantum fluctuations in this geometry can be summarized by a simple number: γ_{\parallel} . This coefficient is universal in the sense that it does not depend on the microscopic details of the interactions between the fluctuating field and the constituents of the surfaces. It is completely fixed by specifying the geometry, the nature of the fluctuating field

and the type of boundary conditions. For instance, for a fluctuating real scalar field with Dirichlet boundary conditions, the parallel-plate coefficient is

$$\gamma_{\parallel} = \frac{\pi^2}{480} \simeq 2.056 \times 10^{-2}, \quad (5.6)$$

which can easily be extracted from Eq. (2.19) with $D = 4$. For an electromagnetic field and two perfectly conducting plates, the coefficient is exactly twice as large, the factor of 2 can be traced back to the two polarization modes of the electromagnetic field (cf. chapter 2).

At this point the question arises, if the distance a really is the only scale and the previous arguments are valid at all. After all, in case of the electromagnetic field at least two further scales should enter the computation via the QED Lagrangian: the electron mass m and the electron charge e . Moreover, the conducting plates are characterised by the surface charge density. But all these quantities are integrated in the boundary conditions, which in fact do depend on them, as long as the plates cannot be regarded as *perfect* conductors. Strictly speaking, only in the limit $e \rightarrow \infty$ (with fixed electron mass and charge density) the conductors are perfect and the boundary conditions do not depend on dimensionful quantities any more. However, this limit is sufficiently achieved for realistic values [57].

Beside from finite conductivity, corrections to Eq. (5.5) arise from surface roughness, thermal fluctuations and deviations from the ideal geometry. All these come with additional dimensionful scales, such as plasma frequency, length scales of roughness variation, temperature or surface-curvature radii. The corrections generically cannot be predicted from dimensional analysis, but its functional dependence on the further parameters has to be computed [16–22, 24, 59].

This chapter is devoted to an investigation of the Casimir force between disconnected rigid surfaces, which exhibits properties similar to Casimir's classic parallel-plate configuration: unique dimensional scale dependencies and universal coefficients. The first property implies that the geometry is characterized by only one length scale, such as the distance parameter a . New Casimir configurations therefore necessarily involve edges, whose influence on the Casimir effect is an interesting and difficult question in itself. In view of the rapid progress in the fabrication and use of micro- and nano-scale mechanical devices, accompanied by precision measurements of the Casimir forces in these systems [2–7, 14, 15], a detailed understanding of Casimir edge effects is indispensable.

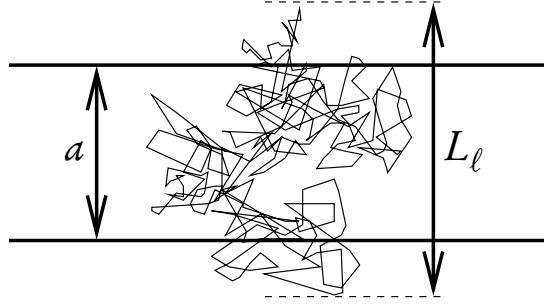


Figure 5.1: Geometry of Casimir's parallel-plate configuration. A loop contributes to the Casimir interaction energy if its extent L_ℓ along the z direction is larger than the plate distance a .

5.2 Casimir edge configurations

Before we study three different Casimir edge configurations, let us initially revisit Casimir's classic parallel-plate configuration. On the one hand, this configuration is simpler than the succeeding examples but technically very similar, thus yielding a good introduction to the true edge configurations. On the other hand, it will reveal an unexpected mapping between the D -dimensional Casimir effect and standard polymer physics.

5.2.1 Parallel plates revisited

Let us reconsider Casimir's classic parallel-plate configuration in $D = d + 1$ dimensional spacetime, doing the \mathbf{x}_{CM} integral first and keeping the ensemble average till the very end.

In d space dimensions, the surface or area volume A of the Casimir plates is taken as $d - 1$ dimensional. The two (hyper-)plates are separated by a distance a along the z direction which is normal to the plates, see Fig. 5.1. For this configuration, the Casimir interaction energy for the massless Dirichlet scalar boils down to

$$E_{\text{Casimir}} = -A \frac{1}{2(4\pi)^{D/2}} \frac{1}{n_L} \sum_{\ell=1}^{n_L} \int_0^\infty \frac{dT}{T^{1+D/2}} \int_{-\infty}^\infty dz_{\text{CM}} \Theta[z_{\text{CM}} + \sqrt{T}y_{z\ell}], \quad (5.7)$$

where $y_{z\ell}$ denotes the z coordinate of the ℓ th unit loop. Let us denote the extent of the ℓ th unit loop in the z direction by L_ℓ ,

$$L_\ell := \max_{i,k} (|y_{z\ell i} - y_{z\ell k}|), \quad (5.8)$$

see Fig. 5.1. A scaled unit loop intersects both plates if $\sqrt{T}L_\ell \geq a$. For a given

unit loop with extent L_ℓ and for a given proptime value T , the support of the z_{CM} integral corresponds to an interval $I_z(T, L_\ell) = \sqrt{T}L_\ell - a$. Independently of the precise location of this interval on the z_{CM} axis, the z_{CM} integral yields,

$$\int_{-\infty}^{\infty} dz_{\text{CM}} \Theta[z_{\text{CM}} + \sqrt{T}y_{z\ell}] = (\sqrt{T}L_\ell - a)\theta(\sqrt{T}L_\ell - a). \quad (5.9)$$

Now, also the T integral can be done analytically, resulting in

$$\begin{aligned} E_{\text{Casimir}} &= -\frac{A}{a^{D-1}} \frac{1}{D(D-1)(4\pi)^{D/2}} \frac{1}{n_L} \sum_{\ell=1}^{n_L} L_\ell^D \\ &= -\frac{A}{a^{D-1}} \frac{1}{D(D-1)(4\pi)^{D/2}} \langle L_\ell^D \rangle. \end{aligned} \quad (5.10)$$

We observe that the Casimir interaction energy of the parallel-plate configuration in $D = d + 1$ spacetime dimensions is proportional to the D th moment of the ensemble-averaged extent of a unit loop. This ensemble average could easily be performed, which would lead us back to the results of [35].

Here, we will be satisfied by highlighting Eq. (5.10) from a different perspective, namely, in the language of polymer physics. The Gaussian velocity distribution of our worldlines is identical to the Hamiltonian of a polymer, i.e., the continuum limit of a random chain, without self-avoidance or excluded-volume effect [81] in the limit of zero end-to-end distance. In this language, L_ℓ corresponds to the maximum spatial extent of the closed polymer measured in units of $\sqrt{l_p c / (2D_p)}$. Here, $l_p = Nc$ denotes the total length of the polymer, c is the chain length, and D_p is the number of dimensions in which the polymer can move; the latter is completely arbitrary and independent of the dimensionality of the Casimir system. Since L_ℓ is a highly non-local object, its ensemble average is actually not so easily computable by standard methods. Our result Eq. (5.10) now maps the problem of computing any D th moment of L_ℓ on the D -dimensional Casimir problem for parallel plates. Using the standard result for the latter, Eq. (2.19), [58, 82, 83],

$$E_{\text{Casimir}} = -\frac{A}{(4\pi)^{D/2} a^{D-1}} \Gamma(D/2) \zeta(D). \quad (5.11)$$

we obtain by comparison with Eq. (5.10),

$$\langle L_\ell^D [y] \rangle = D(D-1) \Gamma(D/2) \zeta(D), \quad (5.12)$$

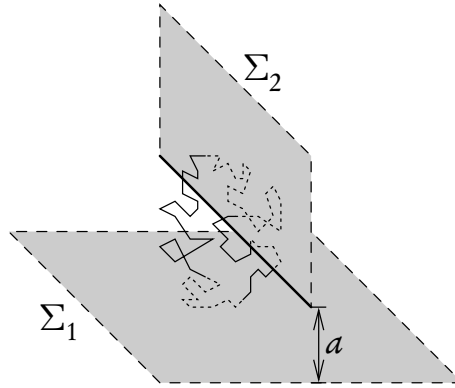


Figure 5.2: Sketch of the perpendicular-plates configuration. The minimal distance a between the edge of the upper semi-infinite plate (thick solid line) and the lower infinite plate represents the only dimensionful length scale in the problem.

a result that we have so far not been able to find in the literature of polymer physics. Even the limit $D \rightarrow 1$ can be taken, corresponding to the Casimir effect in zero space dimensions: this results in $\langle L_\ell[\gamma] \rangle = \sqrt{\pi}$ for the average extent of a closed polymer.

5.2.2 Perpendicular Plates

Let us now analyse a perfectly thin semi-infinite plate perpendicularly above an infinite plate at a minimal distance a , as first proposed in [53]. This configuration is illustrated in Fig. 5.2 together with a worldline which contributes to the Casimir interaction energy, since it intersects both plates. This configuration is translationally invariant only in the direction pointing along the edge with a being the only dimensionful length scale. The Casimir force per unit length L along the edge direction is thus unambiguously fixed by dimensional analysis,

$$\frac{F_\perp}{L} = -\gamma_\perp \frac{\hbar c}{a^3}. \quad (5.13)$$

We assume the infinite plate to be parallel to the x - y plane at $z = -a$, the semi-infinite plate to cover the y - z plane for positive z values,

$$\Sigma_1 = \{\mathbf{x} : z = -a\} \quad (5.14)$$

$$\Sigma_2 = \{\mathbf{x} : x = 0 \wedge z \geq 0\}. \quad (5.15)$$

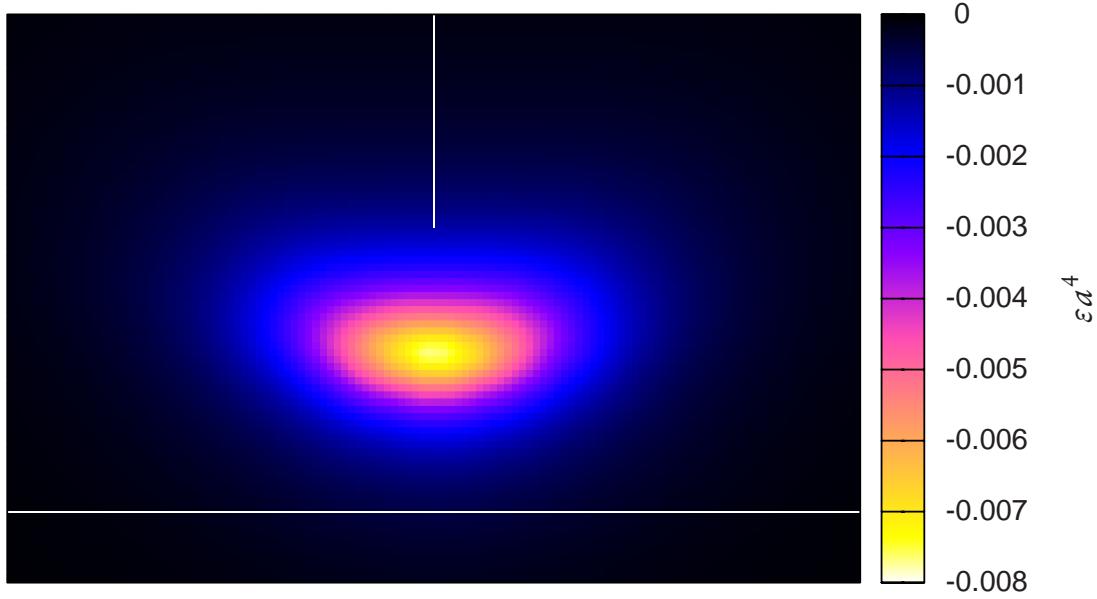


Figure 5.3: Contour plot of the Casimir interaction energy density ε for the perpendicular-plate configuration. The white lines mark the position of the plates to guide the eye. Ensemble parameters: 2000 loops with 10 000 ppl.

The Casimir interaction-energy is, similar to Eq. (5.7),

$$E_{\text{Casimir}} = -L \frac{1}{2(4\pi)^{D/2}} \frac{1}{n_L} \sum_{\ell=1}^{n_L} \int_0^\infty \frac{dT}{T^{1+D/2}} \times \int_{-\infty}^\infty dx_{\text{CM}} \int_{-\infty}^\infty dz_{\text{CM}} \Theta_{\perp}[\gamma(t)](T, x_{\text{CM}}, y_{\text{CM}}). \quad (5.16)$$

Omitting the spatial integrations and the factor L , straightforward worldline numerics results in the Casimir interaction-energy density $\varepsilon(\mathbf{x})$ plotted in Fig. 5.3.

When computing the total interaction-energy, two of the three integrations can be performed analytically as described in the following. The Θ function can be written as product of two θ functions, probing the intersection of the unit loop $\gamma(t)$ with the infinite and the semi-infinite plate, respectively:

$$\Theta_{\perp}[\gamma(t)](T, x_{\text{CM}}, z_{\text{CM}}) = \theta(-((z_{\text{CM}} + \sqrt{T}y_{z_{\min}}) + a)) \times \theta(z_{\text{CM}} + \sqrt{T}y_{z_{\max}}(-\frac{x_{\text{CM}}}{\sqrt{T}})) \quad (5.17)$$

Here, $y_{z_{\min}}$ denotes the minimal z value of the unit loop, $y_{z_{\max}}(x')$ the maximal value

$x' := -x_{\text{CM}}/\sqrt{T}$:

$$\int_0^\infty \frac{dT}{T^{1+D/2}} \int_{-\infty}^\infty dx' \sqrt{T} \left(-\sqrt{T}y_{z\text{min}} - a + \sqrt{T}y_{z\text{max}}(x') \right) \times \\ \times \theta(-\sqrt{T}y_{z\text{min}} - a + \sqrt{T}y_{z\text{max}}(x')) \quad (5.21)$$

After interchanging x' and T integral, the θ function translates to a lower bound of the T integral:

$$\int_{-\infty}^\infty dx' \int_{a^2/(y_{z\text{max}}(x')-y_{z\text{min}})^2}^\infty dT \left(\frac{y_{z\text{max}}(x')-y_{z\text{min}}}{T^{D/2}} - \frac{a}{T^{(1+D)/2}} \right) \\ = \frac{2}{(D-1)(D-2)} \frac{1}{a^{D-2}} \int_{-\infty}^\infty dx' (y_{z\text{max}}(x')-y_{z\text{min}})^{D-1} \quad (5.22)$$

Restoring the prefactors of Eq. (5.16) and interchanging the ensemble average with the x' integral, we finally obtain for the interaction energy per length

$$E_{\text{Casimir}\perp} = -\frac{L}{(4\pi)^{D/2}(D-1)(D-2)a^{D-1}} \int_{-\infty}^\infty dx' \langle (y_{z\text{max}}(x')-y_{z\text{min}})^{D-1} \rangle \quad (5.23)$$

The numerical effort for determining the function $y_{z\text{max}}(x')$ and the value $y_{z\text{min}}$ for all loops, performing the averaging and the x' integral is comparatively small. Without difficulty a standard PC handles the computation for a path ensemble of 40 000 loops with 200 000 points per loop (ppl) each. For the universal coefficient, we obtain

$$\gamma_\perp = 1.200(4) \times 10^{-2}. \quad (5.24)$$

The error is below the 1% level. This coefficient is in agreement with the Casimir interaction energy computed in [53].

5.2.3 Semi-infinite plate parallel to an infinite plate

Next we consider a first variant of the parallel-plate configuration, where one of the thin plates is only semi-infinite with an edge on one side; see Fig. 5.5. This configuration can be viewed as an idealized limit of a real experimental situation where a smaller controllable finite plate is kept parallel above a larger fixed substrate. In this case, the dominant contribution to the force is given by the universal classic parallel-plate result of Eq. (5.5) with A being the surface area of the smaller plate. In the ideal limit of A as well as the edge length L going to infinity, the sub-leading

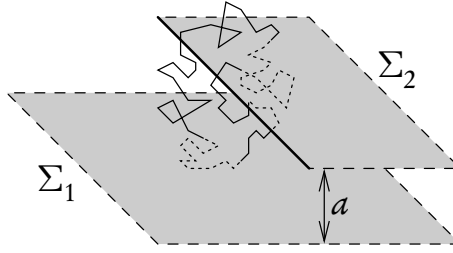


Figure 5.5: Sketch of the configuration of a semi-infinite plate parallel to an infinite plate at a distance a . A worldline can intersect both plates even if its centre of mass is located outside the two plates.

Casimir edge effect is also universal. Dimensional analysis requires the exact force to be of the form

$$F = F_{\parallel} - \gamma_{1\text{si}} \frac{\hbar c}{a^3} L, \quad (5.25)$$

where F_{\parallel} denotes the parallel-plate force for the Dirichlet scalar, i.e., without the factor 2 in Eq. (5.5). A priori, the universal coefficient $\gamma_{1\text{si}}$ can be positive or negative. The sign can easily be guessed within the worldline picture: owing to their spatial extent, a sizeable fraction of worldlines can intersect both plates even if their centre of mass is located outside the plates. This can quantitatively be verified by the energy density, which is obtained using the same expression as for the perpendicular plates, Eq. (5.16), with a suitable function $\Theta_{1\text{si}}$ instead of Θ_{\perp} . The resulting density plot is shown in Fig. 5.6. Indeed, the peak of the density extends into the outside region of the plates. This peak contributes to the total interaction energy, implying an increase of the Casimir force compared to the pure parallel-plate formula. Therefore, the Casimir edge effect leads to further attraction, and the sign of the universal coefficient $\gamma_{1\text{si}}$ must be positive.

To verify this quantitatively, we evaluate Eq. (5.16). Again, two integrations can be performed analytically. First of all, we specify the geometry, which is the same as in the previous example, but with the semi-infinite plate Σ_2 rotated into the x - y plane:

$$\Sigma_1 = \{\mathbf{x} : z = -a\} \quad (5.26)$$

$$\Sigma_2 = \{\mathbf{x} : z = 0 \wedge x \geq 0\}. \quad (5.27)$$

Again, the function $\Theta_{1\text{si}}$ separates into θ functions, probing the intersection with the

plates:

$$\Theta_{1\text{si}}[y(t)](T, x_{\text{CM}}, z_{\text{CM}}) = \theta(-(z_{\text{CM}} + \sqrt{T}y_{z\text{min}} + a)) \times \\ \times \theta(z_{\text{CM}} + \sqrt{T}y_{z\text{max}}) \theta(x_{\text{CM}} + \sqrt{T}y_{x\text{max}}(-\frac{z_{\text{CM}}}{\sqrt{T}})), \quad (5.28)$$

where $y_{z\text{min}}$ and $y_{z\text{max}}$ denote the minimal and maximal z value of the unit loop, $y_{x\text{max}}(z')$ the maximal value of $y_z(t)$ under the constraint $y_z(t) = z'$ (see Fig. 5.7). The first θ function probes if the loop intersects the lower, infinite plate; the product of the other θ functions is one if and only if the loop intersects the upper, semi-infinite plate. Only the last θ function depends on x_{CM} and translates to a lower bound of the x_{CM} integration, which thus runs from $-\sqrt{T}y_{x\text{max}}(-z_{\text{CM}}/\sqrt{T})$ to infinity. We split this integral into two parts, one going from $-\sqrt{T}y_{x\text{max}}(-z_{\text{CM}}/\sqrt{T})$ to zero, the other one from zero to infinity. The contribution of the latter to the interaction energy is

$$E_{1\text{si},\parallel} = -L \frac{1}{2(4\pi)^{D/2}} \frac{1}{n_L} \sum_{\ell=1}^{n_L} \int_0^\infty \frac{dT}{T^{1+D/2}} \int_{-\infty}^\infty dz_{\text{CM}} \times \\ \times \theta(-(z_{\text{CM}} + \sqrt{T}y_{z\text{min}} + a)) \theta(z_{\text{CM}} + \sqrt{T}y_{z\text{max}}) \frac{L}{2} \quad (5.29)$$

$$= -\frac{A}{2} \frac{1}{2(4\pi)^{D/2}} \frac{1}{n_L} \sum_{\ell=1}^{n_L} \int_0^\infty \frac{dT}{T^{1+D/2}} \int_{-\sqrt{T}y_{z\text{max}}}^{-\sqrt{T}y_{z\text{min}}+a} dz_{\text{CM}} \times \\ \times \theta(\sqrt{T}(y_{z\text{max}} - y_{z\text{min}}) - a) \quad (5.30)$$

$$= -\frac{A}{2} \frac{1}{2(4\pi)^{D/2}} \frac{1}{n_L} \sum_{\ell=1}^{n_L} \int_0^\infty \frac{dT}{T^{1+D/2}} (\sqrt{T}(y_{z\text{max}} - y_{z\text{min}}) - a) \times \\ \times \theta(\sqrt{T}(y_{z\text{max}} - y_{z\text{min}}) - a) \quad (5.31)$$

Comparing this expression with Eq. (5.7) and Eq. (5.9) reveals it to be just the infinite-plates result divided by two and thus the PFA approximation. The negative derivative of this energy with respect to the distance yields the force F_{\parallel} in Eq. (5.25). Accordingly, the second part of the right hand side in the same equation—that means the edge effect—is described by the x_{CM} integral from $-\sqrt{T}y_{x\text{max}}(-z_{\text{CM}}/\sqrt{T})$ to zero. The

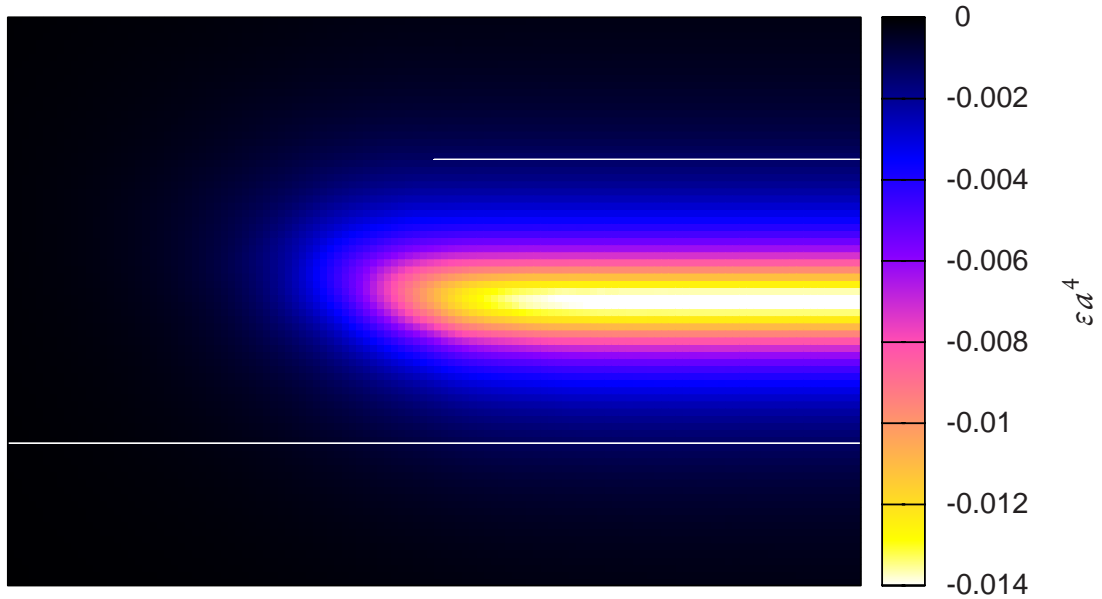


Figure 5.6: Contour plot of the Casimir interaction energy density ε for a semi-infinite plate parallel to an infinite plate. The white lines mark the position of the plates to guide the eye. The energy-density peak extends into the outside region, since worldlines can intersect both plates even if their centre of mass is in the outside region. Ensemble parameters: 1000 loops, 10 000 ppl.

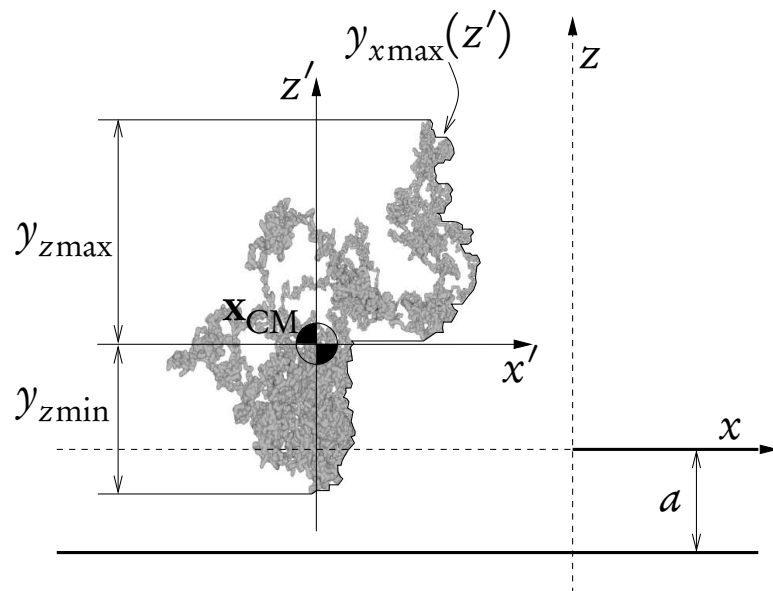


Figure 5.7: Geometry of the semi-infinite plate parallel to an infinite plate with a unit loop. All relevant information of the unit loop is encoded in the values y_{zmin} and y_{zmax} (the former is negative), and the function $y_{xmax}(z')$.

contribution of this part to the interaction energy reads

$$\begin{aligned}
E_{1\text{si,edge}} = & -L \frac{1}{2(4\pi)^{D/2}} \frac{1}{n_L} \sum_{\ell=1}^{n_L} \int_0^\infty \frac{dT}{T^{1+D/2}} \int_{-\infty}^\infty dz_{\text{CM}} \times \\
& \times \theta(-(z_{\text{CM}} + \sqrt{T}y_{z\text{min}} + a))\theta(z_{\text{CM}} + \sqrt{T}y_{z\text{max}}) \times \\
& \times \sqrt{T}y_{x\text{max}}(-z_{\text{CM}}/\sqrt{T}) \quad (5.32)
\end{aligned}$$

Substituting $z' := -z_{\text{CM}}/\sqrt{T}$, we obtain

$$\begin{aligned}
E_{1\text{si,edge}} = & -L \frac{1}{2(4\pi)^{D/2}} \frac{1}{n_L} \sum_{\ell=1}^{n_L} \int_0^\infty \frac{dT}{T^{1+D/2}} \int_{-\infty}^\infty dz' \sqrt{T} \times \\
& \times \theta(\sqrt{T}(z' - y_{z\text{min}}) - a)\theta(-\sqrt{T}(z' - y_{z\text{max}}))\sqrt{T}y_{x\text{max}}(z') \quad (5.33)
\end{aligned}$$

$$\begin{aligned}
= & -L \frac{1}{2(4\pi)^{D/2}} \frac{1}{n_L} \sum_{\ell=1}^{n_L} \int_{-\infty}^\infty dz' \int_0^\infty \frac{dT}{T^{D/2}} \times \\
& \times \theta(\sqrt{T}(z' - y_{z\text{min}}) - a)\theta(y_{z\text{max}} - z')y_{x\text{max}}(z') \quad (5.34)
\end{aligned}$$

$$\begin{aligned}
= & -L \frac{1}{2(4\pi)^{D/2}} \frac{1}{n_L} \sum_{\ell=1}^{n_L} \int_{-\infty}^{y_{z\text{max}}} dz' \int_{a^2/(z'-y_{z\text{min}})^2}^\infty \frac{dT}{T^{D/2}} \times \\
& \times \theta(z' - y_{z\text{min}})y_{x\text{max}}(z'). \quad (5.35)
\end{aligned}$$

The remaining θ function comes from the first θ function in the previous line, which is non-zero if $z' - y_{z\text{min}}$ is positive and $T > a^2/(z' - y_{z\text{min}})^2$. Performing the T integral, we obtain

$$E_{1\text{si,edge}} = -L \frac{1}{2(4\pi)^{D/2}} \frac{1}{n_L} \sum_{\ell=1}^{n_L} \int_{y_{z\text{min}}}^{y_{z\text{max}}} dz' \int_{a^2/(z'-y_{z\text{min}})^2}^\infty \frac{dT}{T^{D/2}} y_{x\text{max}}(z') \quad (5.36)$$

$$= -L \frac{1}{2(4\pi)^{D/2}} \frac{1}{n_L} \sum_{\ell=1}^{n_L} \int_{y_{z\text{min}}}^{y_{z\text{max}}} dz' \frac{2}{D-2} \left(\frac{z' - y_{z\text{min}}}{a} \right)^{D-2} y_{x\text{max}}(z') \quad (5.37)$$

$$= -\frac{L}{(4\pi)^{D/2}(D-2)a^{D-2}} \int_{y_{z\text{min}}}^{y_{z\text{max}}} dz' (z' - y_{z\text{min}})^{D-2} \langle y_{x\text{max}}(z') \rangle. \quad (5.38)$$

Finally, we differentiate with respect to a and obtain, in $D = 4$ dimensions, the Casimir force

$$F_{1\text{si}} = F_{\parallel} - \frac{1}{4(4\pi)^{D/2}} \int_{y_{z\text{min}}}^{y_{z\text{max}}} dz' (z' - y_{z\text{min}})^{D-2} \langle y_{x\text{max}}(z') \rangle \frac{L}{a^3} \quad (5.39)$$

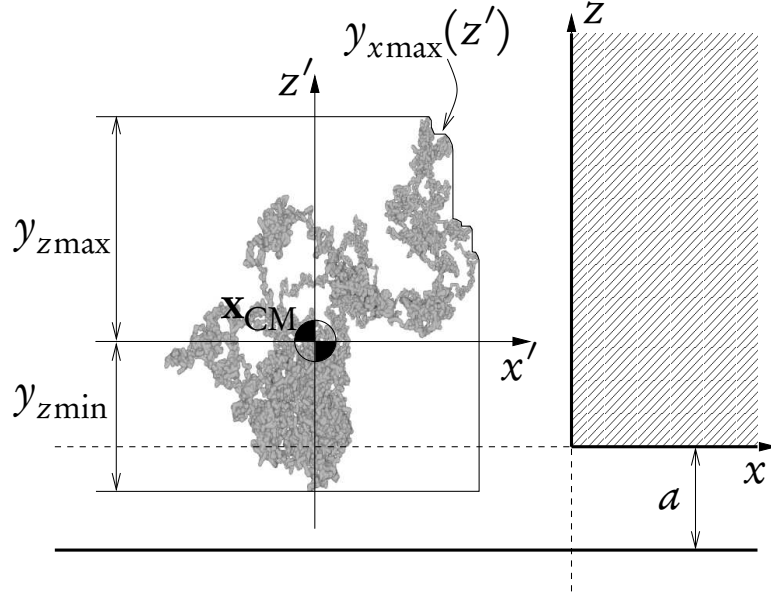


Figure 5.8: Geometry of the infinite thick semi-infinite plate above an infinite plate with a unit loop. Since the interior (hatched) of the plates has no influence on the force, this configuration corresponds to a combination of the previous two configurations in Fig. 5.4 and Fig. 5.7. Accordingly, the function $y_{x\max}(z')$ is an intermediate of the two corresponding previous functions. Again, all relevant information of the unit loop is encoded in the values $y_{z\min}$ and $y_{z\max}$ (the former is negative), and the function $y_{x\max}(z')$.

with the universal coefficient

$$\gamma_{1\text{si}} = \frac{1}{4(4\pi\epsilon)^{D/2}} \int_{y_{z\min}}^{y_{z\max}} dz' (z' - y_{z\min})^{D-2} \langle y_{x\max}(z') \rangle. \quad (5.40)$$

Quantitatively, we find with 40 000 loops and 200 000 ppl

$$\gamma_{1\text{si}} = 5.23(2) \times 10^{-3}. \quad (5.41)$$

5.2.4 Thick plates

At this point, let us again emphasize that whereas the geometries we study are carefully chosen to provide the most qualitative understanding of Casimir edge-effects, which means that we keep the number of scales small, this is no restriction by worldline numerics. The shape of the boundaries can be arbitrary. Of course, not for all geometries we can perform some integrals analytically. But since the computations in this section do not require much CPU time, from the numerical point of view this is not harmful.

Thus, with worldline numerics it is very easy to study more realistic configurations

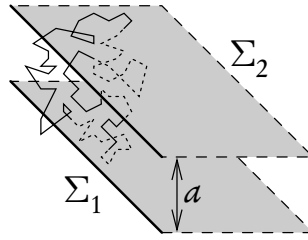


Figure 5.9: Sketch of the configuration with two parallel semi-infinite plates at a distance a .

in which the plates are not infinitely thin. Obviously, in the previous configuration the thickness of the infinite plate has no influence on the Casimir force. By contrast, the thickness of the semi-infinite plate is important and introduces a further scale to the configuration. Instead of computing the interaction energy for a given ratio of the two scales, thickness and distance, we consider the semi-infinite plate to be infinitely thick, the result for finite thickness then interpolates between infinite thin and infinite thick plates. This configuration is again characterised by only one scale, the distance. Therefore, dimensional analysis specifies the form of the force to be the same as in the previous configuration, Eq. 5.25, with an appropriate $\gamma_{1\text{si},t}$ instead of $\gamma_{1\text{si}}$.

Since the interior of the plates has no influence on the force, the infinite thick-plate configuration corresponds to combining the boundaries of the two previous Casimir configurations in one single configuration. The only difference to the previous computation is a different function $y_{x\text{max}}(z')$, which is illustrated in Fig. 5.8, and we can evaluate Eq. (5.40) to obtain the universal coefficient $\gamma_{1\text{si},t} = 6.45(3) \times 10^{-3}$. This represents an increase by 23% compared to $\gamma_{1\text{si}}$, Eq. (5.41). More worldlines from outside can now intersect the thick plate also away from the edge, such that the energy density extends further into the outside region.

5.2.5 Parallel semi-infinite plates

Another variant of the parallel-plate configuration is given by two parallel semi-infinite plates with parallel edges; see Fig. 5.9. This configuration corresponds to an idealized parallel-plate experiment where both plates have the same area size A . In the ideal limit of infinite A as well as infinite edge length L , the exact form of the force is again given by dimensional analysis,

$$F = F_{\parallel} - \gamma_{2\text{si}} \frac{\hbar c}{a^3} L, \quad (5.42)$$

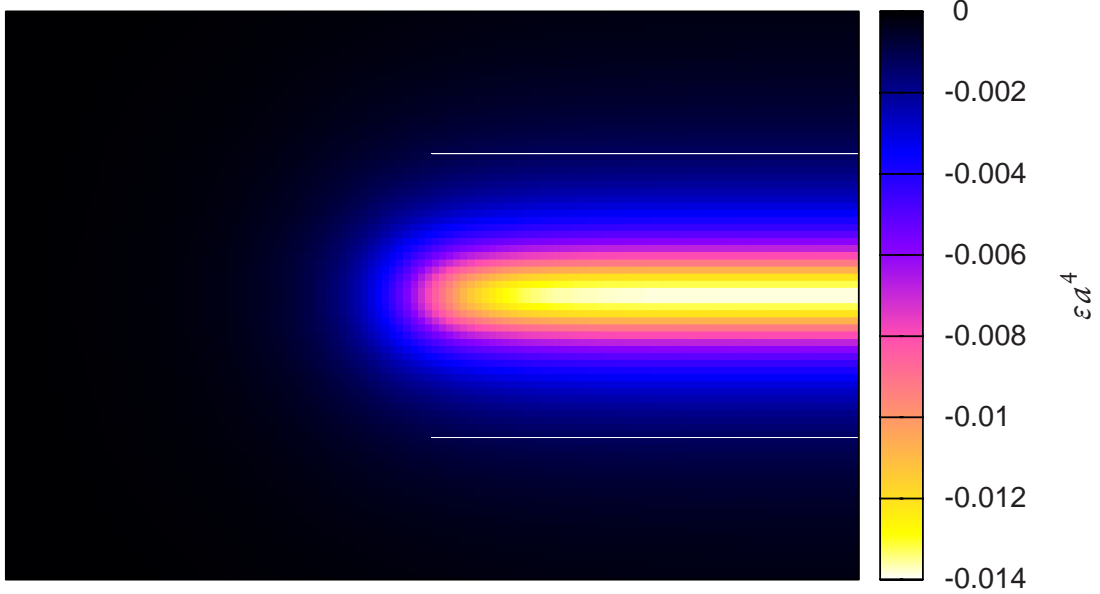


Figure 5.10: Contour plot of the Casimir interaction energy density ε for two parallel semi-infinite plates. The energy-density peak extends into the outside region, since worldlines can intersect both plates even if their centre of mass is in the outside region. Ensemble parameters: 2000 loops, 10 000 ppl.

equivalent to Eq. (5.25). Qualitatively, the situation is similar to the preceding one with one semi-infinite plate. Quantitatively, fewer worldlines in the outside as well as the inside region near the edge intersect both plates. Both aspects are visible in the plot of the interaction energy density in Fig. 5.10: the peak height and width is reduced near the edge both inside and outside the plates.

When computing the universal coefficient, a significant difference prevents us from performing as many integrals as in the previous examples (that means two) analytically. Probing the intersection of a loop with an infinite plate, as in the previous configurations, allows to boil down the information of a loop to a single number, the extend perpendicular to the plate. Only the contribution of the semi-infinite plate, and in particular of its edge, is sensitive to more detailed properties of the loop's geometry. This properties have been encoded in the function $y_{z_{\max}}(x')$ for all three previous cases. Now that we have two edges, we will have to deal with two corresponding functions, and accordingly two numerical integrations.

Instead of following the prior procedure of specifying the function $\Theta[y(t)](T, x_{\text{CM}}, z_{\text{CM}})$ and successively performing the T , x_{CM} and y_{CM} integrations, we will now use a slightly different but equivalent approach, which is exemplary for other more complicated configurations. We exploit that in Eq. (5.16) the x_{CM} and y_{CM} integrations over the function $\Theta[y(t)](T, x_{\text{CM}}, z_{\text{CM}})$ for a given unit loop $y(t)$ and proptime T

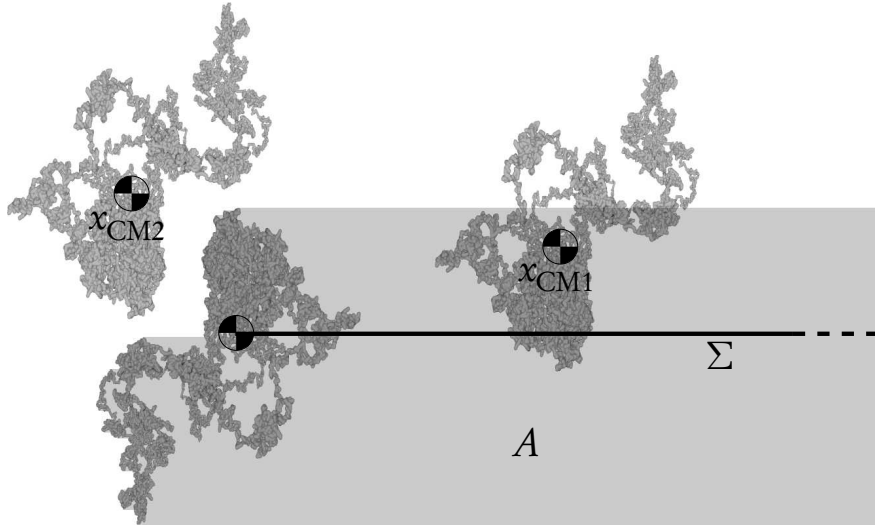


Figure 5.11: For a given loop, the area defined by all possible centres of mass for which the loop intersects a semi-infinite plate can be determined by positioning the loop rotated by 180° on the edge of the plate: loops with centre of mass inside the shaded area (e.g. x_{CM1}) do intersect the plate, in contrast to loops with centre of mass outside (e.g. x_{CM2}).

yield the size of an area in the x - z plane. This area can often be determined very easily from the shape of the boundaries and the loop. It is the set of centres of mass for which a loop intersects both boundaries. It is convenient to determine for each boundary Σ the area A defined by all centres of mass for which the loop intersects this single boundary (cf. Fig. 5.11) and determine the intersection A_\cap afterwards (cf. Fig. 5.12). In terms of A_\cap , Eq. (5.16) reads

$$E_{\text{Casimir}} = -L \frac{1}{2(4\pi)^{D/2}} \frac{1}{n_L} \sum_{\ell=1}^{n_L} \int_0^\infty \frac{dT}{T^{1+D/2}} A_\cap[y(t)](T). \quad (5.43)$$

In case of the two semi-infinite plates, the shape of the area A for each plate has to be determined only once for all proper times T , since it is the same for all values T , only the size is scaled by a factor of \sqrt{T} . To determine this set for a given loop, we position the loop on the edge of the plate and rotate it by 180° around the edge. The coordinates of this rotated loop define the boundaries of the set as illustrated in Fig. 5.11. Loops with centre of mass inside the shaded area (e.g. x_{CM1}) do intersect the plate, in contrast to loops with centre of mass outside (e.g. x_{CM2}). In practice, we can omit the rotation and use the original loops. This corresponds to rotating the whole loop ensemble before any computation, which is legitimised by the rotation invariance of the loop ensemble's statistical properties.

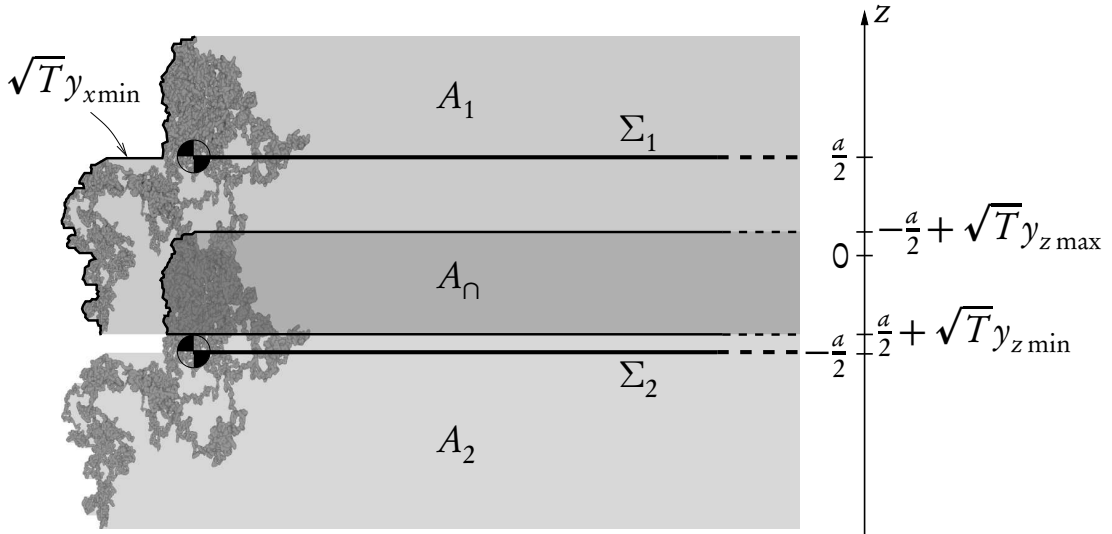


Figure 5.12: A loop only contributes to the Casimir force, if it intersects both plates. The centres of mass for which this is the case can be determined by the intersection of the areas illustrated in Fig. 5.11 corresponding to each plate.

In the following, we assume the semi infinite plates to be parallel to the x - y plane, with the edge parallel to the y axis, at $z = a/2$ and $z = -a/2$, respectively:

$$\Sigma_1 = \{\mathbf{x} : z = a/2 \wedge x > 0\}, \quad (5.44)$$

$$\Sigma_2 = \{\mathbf{x} : z = -a/2 \wedge x > 0\}. \quad (5.45)$$

For each unit loop, we define $y_{x\min}(z')$ as the minimal x value of all loop points with a given z value,

$$y_{x\min}(z') := \min\{x' : \exists_t x' = y_x(t) \wedge z' = y_z(t)\}, \quad (5.46)$$

see Fig. 5.12, and the smallest and largest z values, $y_{z\min}$ and $y_{z\max}$, respectively. With this notation, we can write the intersection set A_\cap as

$$\begin{aligned} A_\cap[y(t)](T) = & \int_0^\infty dx \left(\sqrt{T}(y_{z\max} - y_{z\min}) - a \right) \theta(\sqrt{T}(y_{z\max} - y_{z\min}) - a) \\ & + \int_{a/2 + \sqrt{T}y_{z\min}}^{-a/2 + \sqrt{T}y_{z\max}} dz \max \left(\sqrt{T}y_{x\min}\left(\frac{z+a/2}{\sqrt{T}}\right), \sqrt{T}y_{x\min}\left(\frac{z-a/2}{\sqrt{T}}\right) \right). \end{aligned} \quad (5.47)$$

The infinite x integral leads the proximity force approximation (cf. Eq. 5.9). The effect of the edge is encoded in the second term, which we denote by ΔA_\cap in the

following:

$$\begin{aligned} \Delta A_{\cap}[\gamma(t)](T, a) \\ := \int_{a/2+\sqrt{T}y_{z\min}}^{-a/2+\sqrt{T}y_{z\max}} dz \max \left(\sqrt{T}y_{x\min}\left(\frac{z+a/2}{\sqrt{T}}\right), \sqrt{T}y_{x\min}\left(\frac{z-a/2}{\sqrt{T}}\right) \right). \end{aligned} \quad (5.48)$$

With this definition, we can write the correction to the PFA result of the interaction energy as

$$\begin{aligned} E_{2\text{si},\text{edge}} = \left\langle -\frac{L}{2(4\pi)^{D/2}} \int_{a^2/(y_{z\max}-y_{z\min})^2}^{\infty} \frac{dT}{T^{1+D/2}} \int_{a/2+\sqrt{T}y_{z\min}}^{-a/2+\sqrt{T}y_{z\max}} dz \times \right. \\ \left. \times \max \left(\sqrt{T}y_{x\min}\left(\frac{z+a/2}{\sqrt{T}}\right), \sqrt{T}y_{x\min}\left(\frac{z-a/2}{\sqrt{T}}\right) \right) \right\rangle \end{aligned} \quad (5.49)$$

$$= \left\langle -\frac{L}{2(4\pi)^{D/2}} \int_{a^2/(y_{z\max}-y_{z\min})^2}^{\infty} \frac{dT}{T^{1+D/2}} \Delta A_{\cap}(T, a) \right\rangle. \quad (5.50)$$

For the numerical evaluation, it is suitable to translate the scaling of the unit loops with the factor \sqrt{T} and the corresponding scaling of its argument to a translation in z direction. For this, we substitute $z' := z/\sqrt{T}$,

$$\begin{aligned} E_{2\text{si},\text{edge}} = \left\langle -\frac{L}{2(4\pi)^{D/2}} \int_{a^2/(y_{z\max}-y_{z\min})^2}^{\infty} \frac{dT}{T^{D/2}} \int_{a/(2\sqrt{T})+y_{z\min}}^{-a/(2\sqrt{T})+y_{z\max}} dz' \times \right. \\ \left. \times \max \left(y_{x\min}\left(z' + \frac{a}{2\sqrt{T}}\right), y_{x\min}\left(z' - \frac{a}{2\sqrt{T}}\right) \right) \right\rangle \end{aligned} \quad (5.51)$$

$$= \left\langle -\frac{L}{2(4\pi)^{D/2}} \int_{a^2/(y_{z\max}-y_{z\min})^2}^{\infty} \frac{dT}{T^{D/2}} \Delta A_{\cap}(1, a/\sqrt{T}) \right\rangle. \quad (5.52)$$

For a given unit loop, the set ΔA_{\cap} is now computed without scaling the loop, but with a varying plate distance a/\sqrt{T} . To make the expression even more convenient for numerical evaluation, we finally substitute $\xi := a/\sqrt{T}$, so that the distance scales

linearly with the integration variable,

$$E_{2\text{si,edge}} = \left\langle -\frac{L}{(4\pi)^{D/2}a^{D-2}} \int_0^{y_{z\text{max}}-y_{z\text{min}}} d\xi \xi^{D-3} \int_{\xi/2+y_{z\text{min}}}^{-\xi/2+y_{z\text{max}}} dz' \times \right. \\ \left. \times \max\left(y_{x\text{min}}\left(z' + \frac{\xi}{2}\right), y_{x\text{min}}\left(z' - \frac{\xi}{2}\right)\right) \right\rangle \quad (5.53)$$

$$= \left\langle -\frac{L}{(4\pi)^{D/2}a^{D-2}} \int_0^{y_{z\text{max}}-y_{z\text{min}}} d\xi \xi^{D-3} \Delta A_{\cap}(1, \xi) \right\rangle. \quad (5.54)$$

The corresponding Casimir force is obtained by derivation with respect to $-a$. For the coefficient $\gamma_{2\text{si}}$ in Eq. (5.42) we obtain with $D = 4$

$$\gamma_{2\text{si}} = \frac{1}{8\pi^2 a^3} \left\langle \int_0^{y_{z\text{max}}-y_{z\text{min}}} d\xi \xi \Delta A_{\cap}(1, \xi) \right\rangle \quad (5.55)$$

This expression can be easily computed numerically: For each unit loop we compute a table of $y_{x\text{min}}(z')$ with a suitable number of values z' . From this, one can easily derive a table of the maximum in Eq. (5.53) versus z' for a discrete set of plate distances ξ between 0 and $y_{z\text{max}} - y_{z\text{min}}$. Both, the z' and the ξ integral, are then computed by summing over tabulated values.

We still observe a positive universal coefficient,

$$\gamma_{2\text{si}} = 2.30(1) \times 10^{-3} \quad (5.56)$$

(93 000 loops, 500 000 ppl), which is a bit less than half as big as the preceding case with one semi-infinite plate. Again, the Casimir edge effect increases the force in comparison with the pure parallel-plate estimate F_{\parallel} .

5.3 Edge-configuration estimates

The universal results for the idealized configurations presented above can immediately be used to derive estimated predictions for further Casimir configurations without performing a full worldline-numeric computation.

5.3.1 Casimir comb

Replicating the perpendicular-plate configuration in the horizontal direction of Figs. 5.2 and 5.3, we obtain a stack of semi-infinite plates (a ‘‘Casimir comb’’) per-

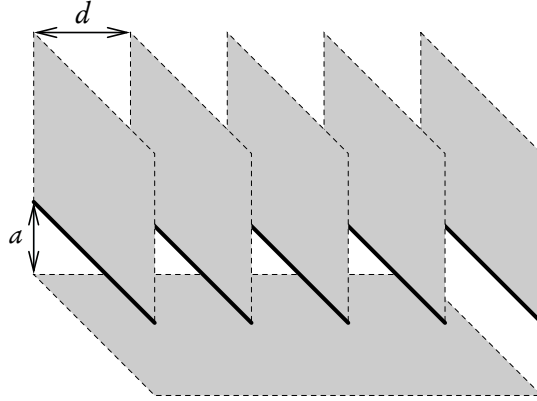


Figure 5.13: Replicating the perpendicular-plate configuration in the horizontal direction of Figs. 5.2 and 5.3, we obtain a stack of semi-infinite plates (a “Casimir comb”) perpendicularly above an infinite plate. If the distance a is small compared to the distance d , the Casimir force can be computed by summing over the result for configuration Fig. 5.2.

pendicularly above an infinite plate as illustrated in Fig. 5.13. Let d be the distance between two neighbouring semi-infinite plates, i.e., the distance between two teeth of the comb. In the limit $d \gg a$, we obtain the Casimir force between the Casimir comb and the infinite plate by simply adding the forces for the individual perpendicular plates. The reliability of this approximation is obvious from Fig. 5.3, which shows that the dominant contribution to the energy is peaked inside a region with length scale $\sim a$. The resulting force is

$$F_{\text{comb}} = -\gamma_{\perp} \frac{\hbar c}{a^3 d} A, \quad (5.57)$$

with $A = Lnd$ being the total area of a comb with n teeth. For a fixed comb, i.e., fixed d , the short-distance Casimir force thus has a weaker dependence on a than for the parallel-plate case. In the opposite limit $d \ll a$, we expect the force between the comb and the plate to rapidly approach that of the parallel-plate case (5.5). This is because a generic worldline contributing to the force will have a spatial extent of order a , such that the finer comb scale $d \ll a$ will not be resolved by the worldline ensemble to first approximation. A similar observation has been made in studies of periodic corrugations [32, 33].

5.3.2 Finite parallel-plate configurations

In a real parallel-plate experiment, the finite extent of the plates induces edge effects. If the typical length scale L of a plate (such as the edge length of a square plate or the

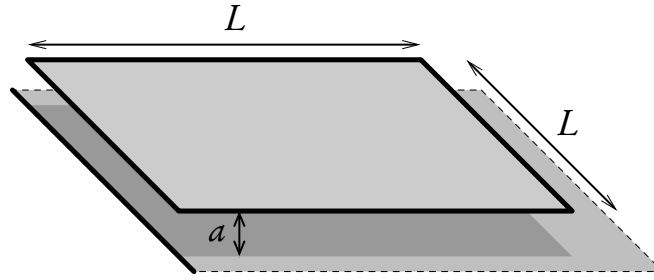


Figure 5.14: A casimir configuration similar to the one used in the experiment of reference [26]. The left edge of the square plate faces an edge of the substrate. Since the distance a is much smaller than the edge length L , the result can be estimated with our prior results for the configurations Fig. 5.5 and Fig. 5.9.

radius of a circular disc) is much larger than the plate distance a , our results for the idealized limits studied above can be used within a good approximation. The force law can then be summarized as

$$F = -\gamma_{\parallel} \frac{\hbar c}{a^4} A_{\text{eff}}, \quad (5.58)$$

where the effective area A_{eff} also carries the information about the edge effects. For the case of a smaller plate with area A and circumference C above a much larger substrate, the effective area is given by

$$A_{\text{eff}} = A + \frac{\gamma_{1\text{si}}}{\gamma_{\parallel}} a C, \quad (5.59)$$

e.g., $C = 4L$ for a square plate with edge length L . For the case of two parallel plates of equal size and shape with area A and circumference C , Eq. (5.59) holds with $\gamma_{1\text{si}}$ replaced by $\gamma_{2\text{si}}$. Obviously, the effective area A_{eff} is larger than the physical area in either case. Finite-thickness corrections can lead to a further increase, as discussed below Eq. (5.41).

Consider, for instance, a square plate of edge length L above a larger substrate: the Casimir edge effects induce a correction on the 1% level if $a \gtrsim 1\%$ of L . In the experiment of reference [26], the edge length is $L = 1.2\text{mm}$ and the distance goes up to $a = 3\mu\text{m}$. One of the edges faces an edge of the substrate, similar to Fig. 5.5, whereas the other three correspond to Fig. 5.9. The resulting configuration is illustrated in Fig. 5.14. For the Dirichlet scalar this results in a correction of 0.2%, which is much smaller than the 15% precision level of the experiment.

Chapter 6

Conclusions (Part I)

We have presented improved worldline numerical algorithms that can efficiently deal with Casimir configurations involving curved surfaces and edges, respectively.

In chapter 4, we have used these algorithms to compute Casimir interaction energies for the sphere-plate and cylinder-plate configuration induced by a scalar field with Dirichlet boundary conditions. These computations are done from first principles for a wide range of curvature parameters a/R . In general, we observe that curvature effects and geometry dependencies are intriguingly rich, implying that naive estimates can easily be misleading. In particular, predictions based on the PFA are only reliable in the asymptotic no-curvature limit with quantitative validity bounds given above. We have constructed polynomial fits of our results which can be used in the small-curvature regime, $a/R \lesssim 0.1$, as a well-founded substitute for the PFA formulas. Given the size of the true curvature corrections for the Dirichlet scalar, we expect that genuine Casimir curvature effects are in reach of currently planned experiments. In this spirit, the so-called lateral Casimir force for corrugated surfaces has recently been proposed as a suitable candidate for identifying non-trivial geometry dependences beyond the PFA [84].

Beyond the Dirichlet scalar investigated here, it is well possible, e.g., for the EM field, that some cancellation of curvature effects occurs between modes obeying different boundary conditions. In fact, such a partial cancellation between TE and TM modes of the separable cylinder-plate geometry can be observed in the recent exact result for the EM field for medium curvature [40]; for small curvature, curvature effects can even reverse sign [41]. More quantitatively, the TM mode in the cylinder-plate case obeys Dirichlet boundary condition and thus contributes, e.g., to the linear curvature correction with a coefficient $\simeq 0.194$, as discussed below Eq. (4.17); the TE mode obeys Neumann boundary conditions, giving a negative contribution which in total

turns this linear coefficient for the EM field into $\simeq -0.48$ [41]. The latter result, in fact, lies in the broad range of $[-0.92, -0.25]$ spanned by the PFA; since the PFA does not make any reference to the nature of the fluctuating field, this rough coincidence is, of course, purely accidental. This strong dependence of Casimir curvature effects on the nature of the fluctuating fields alone demonstrates already that approximations ignoring this difference such as the PFA cannot be trusted. We emphasize again that Casimir calculations for the EM field in non-separable geometries, such as the important sphere-plate case, remain a prominent open problem.

In chapter 5, we have performed a detailed quantitative study of Casimir edge effects induced by a fluctuating scalar field obeying Dirichlet boundary conditions. All of our results exhibit a uniquely fixed dependence on dimensionful scales, as for Casimir's classic result. The effect of quantum fluctuations is quantitatively encoded in a universal dimensionless coefficient, which only depends on the geometry, the nature of the fluctuating field and the boundary conditions. From the perspective of a scattering-theory approach, Casimir edge effects are dominated by diffractive contributions to the correlation functions which are difficult to handle for direct approximation techniques [29, 30, 36, 37]; hence, our results give an important first insight into the properties of diffractive contributions to Casimir forces. For Casimir measurements involving electromagnetic fluctuations, our results serve as a first order-of-magnitude estimate of the error induced by edges of finite configurations – an error that any parallel-plate experiment has to deal with.

Our algorithmic strategies also revealed an unexpected mapping between the D -dimensional parallel-plate Casimir effect and aspects of a random-chain polymer ensemble. The origin of this mapping, of course, lies in the fact that both quantum fluctuations in Casimir systems as well as a polymer ensemble can be described by Feynman path integrals. In the present case, the mapping can be utilized to transform a comparatively difficult polymer problem into a field-theoretic Casimir problem which can be solved by a variety of techniques. We believe that this mapping is just a special case of a more general class of mappings with potentially fruitful applications in both directions.

From a technical point of view, we would like to stress that our results demonstrate the capability of worldline numerics for performing high-precision computations with comparatively little computing power. The simple scalability of the algorithms and the flexibility for adapting them to arbitrary geometries makes worldline numerics a unique tool for computing quantum energies.

Appendix A

The proximity force approximation (PFA)

An intriguing property of the Casimir effect has always been its geometry dependence. As long as the typical curvature radii R_i of the surfaces are large compared to the surface separation a , the PFA is assumed to provide for a good approximation. This method is still the standard tool for treating Casimir geometries different from the parallel plates and generally used for comparison with experimental data. In this theses we will refer to PFA results for comparison with our own results several times. Thereby the inability of the PFA to take non-local aspects of the Casimir effect into account will become clear.

The PFA is a conceptually very simple approach. It is directly related to the parallel plates result (chapter 2); the curved surfaces are viewed as a superposition of infinitesimal parallel plates (Fig. A.1) [19, 27, 28]. The Casimir interaction energy is obtained

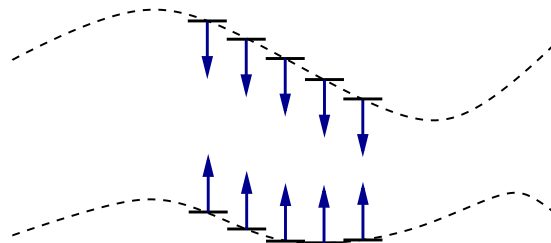


Figure A.1: Proximity force approximation (PFA). The Casimir force between two surfaces (dashed lines) is obtained by an integration of the parallel-plates force (arrows) of the infinitesimal elements (solid lines). The orientation of the infinitesimal elements is not well-defined.

by an integration of the parallel-plates energy applied to the infinitesimal elements,

$$E^{\text{PFA}} = \int_{\Sigma} E_{\text{pp}}(d) d\sigma. \quad (\text{A.1})$$

Here, Σ denotes a “suitable” auxiliary surfaces in between the Casimir surfaces Σ_1 and Σ_2 , and $d\sigma$ is the corresponding surface element of Σ . The distance d between two points on Σ_1 and Σ_2 has to be measured along the normal to Σ . Obviously, the definition of E^{PFA} is ambiguous, owing to possible different choices of Σ [36, 37]. In Fig. A.1, for example, Σ is a horizontal plane. The two extreme cases are $\Sigma = \Sigma_1$ or $\Sigma = \Sigma_2$. The difference in E^{PFA} for these two cases will provide us with a rough error estimate of the PFA. In the above formula, E_{pp} denotes the classic parallel-plates result for the energy per unit area,

$$E_{\text{pp}}(a) = \frac{c_{\text{PP}}}{a^3}, \quad (\text{A.2})$$

with a denoting the plate separations and Casimir’s classic coefficient reads

$$c_{\text{PP}} = -\frac{\pi^2}{720} \times \begin{cases} 1 & \text{for a complex scalar field or the Maxwell field} \\ \frac{1}{2} & \text{for a real scalar field} \end{cases} \quad (\text{A.3})$$

A.1 Sphere above plate

For the configuration of a sphere above a plate (SP), we can choose Σ equal to the plate (plate-based PFA), or equal to the sphere (sphere-based PFA), see Fig. A.2. The corresponding results of the integral of Eq. (A.1) are

$$E_{\text{SP,plate-based}}^{\text{PFA}} = \pi c_{\text{PP}} \frac{R}{a^2} \frac{1}{1 + \frac{a}{R}}, \quad (\text{A.4})$$

and

$$E_{\text{SP,sphere-based}}^{\text{PFA}} = \pi c_{\text{PP}} \frac{R}{a^2} \left(1 - 3\frac{a}{R} - 6\left(\frac{a}{R}\right)^2 \left(1 + \left(1 + \frac{a}{R}\right) \ln \frac{a}{a+R} \right) \right), \quad (\text{A.5})$$

for a denoting the minimal plate-sphere separation and R being the radius of the sphere. In the limit of small distances, $a/R \ll 1$, both PFA’s agree,

$$E_{\text{SP}}^{\text{PFA}}(a/R \ll 1) = \pi c_{\text{PP}} \frac{R}{a^2}, \quad (\text{A.6})$$

demonstrating that (if at all) the PFA is reliable in this limit. It is useful to display the resulting Casimir energies normalized to this small-separation PFA limit:

$$\begin{aligned} \frac{E_{\text{SP,plate-based}}^{\text{PFA}}(a, R)}{E_{\text{SP}}^{\text{PFA}}(a/R \ll 1)} &\simeq 1 - \frac{a}{R} + \mathcal{O}((a/R)^2) \\ \frac{E_{\text{SP,sphere-based}}^{\text{PFA}}(a, R)}{E_{\text{SP}}^{\text{PFA}}(a/R \ll 1)} &\simeq 1 - 3\frac{a}{R} + \mathcal{O}((a/R)^2). \end{aligned} \quad (\text{A.7})$$

Obviously, the PFA predicts in either case that curvature effects reduce the interaction energy ratio. (In fact, the worldline result predicts the opposite).

A.2 Cylinder above plate

For the configuration of a cylinder above a plate (CP), we can choose Σ equal to the plate (plate-based PFA), or equal to the cylinder (cylinder-based PFA), again see Fig. A.2. The corresponding results of the integral of Eq. (A.1) for the energy per unit length in z direction (which points along the cylinder axis) are

$$\begin{aligned} \frac{E_{\text{CP,plate-based}}^{\text{PFA}}}{L_z} &= \frac{2}{R^2} c_{\text{PP}} \int_0^1 d\lambda \frac{1 - \lambda}{\sqrt{2\lambda - \lambda^2} (\frac{a}{R} + \lambda)^3} \\ &= \frac{3\pi}{4\sqrt{2}} c_{\text{PP}} \frac{R^{1/2}}{a^{5/2}} \left(1 - \frac{1}{4} \frac{a}{R} - \frac{5}{32} \left(\frac{a}{R} \right)^2 + \dots \right). \end{aligned} \quad (\text{A.8})$$

and

$$\begin{aligned} \frac{E_{\text{CP,cylinder-based}}^{\text{PFA}}}{L_z} &= \frac{2}{R^2} c_{\text{PP}} \int_0^1 d\lambda \frac{(1 - \lambda)^3}{\sqrt{2\lambda - \lambda^2} (\frac{a}{R} + \lambda)^3} \\ &= \frac{3\pi}{4\sqrt{2}} c_{\text{PP}} \frac{R^{1/2}}{a^{5/2}} \left(1 - \frac{11}{12} \frac{a}{R} + \frac{75}{32} \left(\frac{a}{R} \right)^2 + \dots \right). \end{aligned} \quad (\text{A.9})$$

(NB: both integrals can be evaluated analytically by means of special functions.) Again a denotes the minimal plate-cylinder separation and R is the radius of the cylinder. In the limit of small distances, $a/R \ll 1$, both PFA's agree,

$$E_{\text{CP}}^{\text{PFA}}(a/R \ll 1) = \frac{3\pi}{4\sqrt{2}} c_{\text{PP}} \frac{R^{1/2}}{a^{5/2}}, \quad (\text{A.10})$$

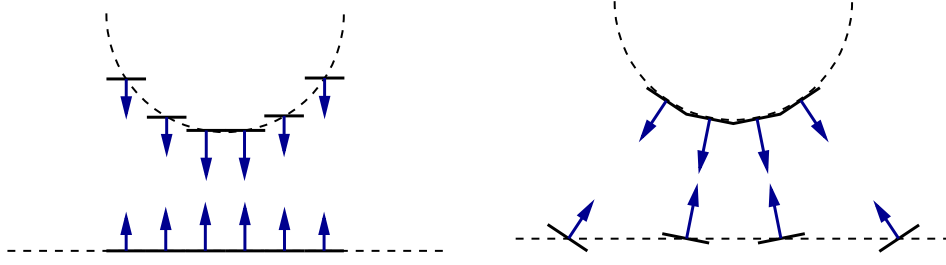


Figure A.2: Plate (left) and sphere/cylinder (right) based PFA. The infinitesimal elements are chosen parallel to the plate and to the sphere/cylinder, respectively.

demonstrating that the PFA is reliable in this limit. The resulting Casimir energies normalized to this small-separation PFA limit are:

$$\begin{aligned} \frac{E_{\text{CP,plate-based}}^{\text{PFA}}(a, R)}{E_{\text{CP}}^{\text{PFA}}(a/R \ll 1)} &\simeq 1 - \frac{1}{4} \frac{a}{R} + \mathcal{O}((a/R)^2) \\ \frac{E_{\text{CP,cylinder-based}}^{\text{PFA}}(a, R)}{E_{\text{CP}}^{\text{PFA}}(a/R \ll 1)} &\simeq 1 - \frac{11}{12} \frac{a}{R} + \mathcal{O}((a/R)^2). \end{aligned} \quad (\text{A.11})$$

Again, the PFA predicts in either case that curvature effects reduce the interaction energy ratio. (And the worldline result predicts the opposite again).

The first field-theoretic confirmation of the zeroth-order result $E_{\text{PFA}}^{(0)}(a, R)$ has been obtained within the semi-classical approximation in [29, 30]. We will use this zeroth-order interaction energy as a normalizer for our numerical estimates. As an advantage, any deviation from this result can be interpreted as a true quantum-induced Casimir curvature effect. Future experiments are indeed expected to become sensitive to the first-order curvature correction, which therefore is of particular interest to us.

Conceptually, the PFA is in contradiction with Heisenberg's uncertainty principle, since the quantum fluctuations are assumed to probe the surfaces only locally at each infinitesimal element. However, fluctuations are not localisable, but at least probe the surface in a whole neighbourhood. In this manner, the curvature information enters the fluctuation spectrum. This quantum mechanism is immediately visible in the worldline formulation of the Casimir problem. Therein, the sum over fluctuations is mapped onto a Feynman path integral, see chapter 3. Each path (worldline) can be viewed as a random spacetime trajectory of a quantum fluctuation. Owing to the generic spatial extent of the worldlines, the path integral directly samples the curvature properties of the surfaces [35].

Part II

Gross-Neveu model

Chapter 7

Introduction

Hot and dense matter, as for example in the early universe, in the centre of a neutron star or in heavy-ion collisions, is still poorly understood. Quantum chromodynamics (QCD), the underlying theory of the dominating force in these systems, the strong interaction, is well known. However, it is very difficult to employ this theory to make predictions about the matter from first principles. Perturbative approaches fail, due to the large coupling at densities and temperatures of greatest physical interest. The fermion sign problem prohibits the use of lattice computations at high densities. By contrast, qualitative understanding can be obtained by studying simplified models which resemble the full QCD, such as the Nambu-Jona-Lasinio (NJL) model [85, 86]. In this model, the gluon interaction is replaced by a four-fermion interaction.

Closely related to the NJL model is the Gross-Neveu model, proposed by David J. Gross and André Neveu in 1974 [87]. Their two dimensional model, also with four-fermion interaction, is solvable in the limit of an infinite number of fermion flavours N and exhibits several properties of QCD, such as asymptotic freedom, baryon bound states, dynamical breaking of chiral symmetry (as well as its restoration at high temperatures) and dimensional transmutation. Besides, the model shares similarities with the description of electrons in polymers, allowing a fruitful exchange between high energy and condensed matter physics [88].

For quite a long time, the ground state of the Gross-Neveu model at large N was believed to be a translation invariant fermion condensate for any chemical potential and temperature. Despite the simplicity of this assumption, the structure of the resulting phase diagram is remarkably rich, showing phases with broken and restored chiral symmetry, separated by phase transitions of first and second order [89].

Only recently, a third phase at finite chemical potential and low temperatures has been discovered [90]. In this phase, the translation symmetry of the ground state is

broken, the vacuum state is a periodic array of bound fermions, a “baryon” lattice. An intriguing question is, if such lattice solutions exist for higher dimensional models and in particular in QCD. An obvious step towards an answer is the extension of the Gross-Neveu model to $2 + 1$ dimensions. But in two dimensions, the periodic ground state has been found by a carefully constructed ansatz, which could be proven to be self-consistent. This method cannot simply be transferred to higher dimensions.

The action of the Gross-Neveu model can be rewritten in terms of an auxiliary, in the large N limit classical, scalar field. The action for the auxiliary field contains a functional trace over the fermion fields. In the work at hand, we evaluate this trace with worldline-numeric techniques. The power of this approach is its universality: once established in the two dimensional model, the extension to higher dimensions should be primarily a matter of required computing power.

The worldline numeric approach to the Gross-Neveu model is still under active development. For this reason, the following chapters are predominantly of technical nature, describing difficulties and progress, to provide a comprehensive snapshot of the ongoing research. Many aspects presented here are of importance for worldline numerics in general: we perform first worldline-numeric computations of fermionic determinants and the introduction of finite temperature is transferable to other worldline numeric computations. In particular, to study the Casimir effect at finite temperature the technique used in this part of the theses will be exceedingly valuable.

This part of the thesis is organised in the following way: In chapter 8 we briefly present the Minkowskian and Euclidean Lagrangian of the Gross Neveu model. After introducing the auxiliary scalar field and its corresponding action, we derive the worldline expression of this action. Chapter 9 is devoted to testing the numerical evaluation of the worldline expression in two dimensions with zero temperature and chemical potential. For that purpose, the worldline expression is renormalised and computed for spatially varying scalar fields involving kinks and antikinks. Finite temperature is introduced into our formalism in chapter 10, which is then employed to compute the critical temperature at which chiral symmetry is restored. In chapter 11, we also incorporate a finite chemical potential, so that we can compute a first phase diagram in chapter 12. There, we (partially) rediscover the phase diagram for the constant scalar field and finally glimpse at the current state of a worldline algorithm for the search of crystal phases in the Gross-Neveu model. We close this part with some conclusions in chapter 13.

Chapter 8

The Gross-Neveu model on the worldline

8.1 Euclidean action

The model, as it has been introduced in its simplest form by David J. Gross and André Neveu in 1974 [87], is described by the Minkowskian Lagrangian

$$\mathcal{L}_M = \bar{\psi} i \not{\partial} \psi + \frac{g^2}{2N} (\bar{\psi} \psi)^2 \quad (8.1)$$

$$\equiv \sum_{\alpha=1}^N \bar{\psi}_{\alpha} i \not{\partial} \psi_{\alpha} + \frac{g^2}{2N} \left(\sum_{\alpha=1}^N \bar{\psi}_{\alpha} \psi_{\alpha} \right)^2 \quad (8.2)$$

The fermion field is supposed to have N components (flavours) ψ_{α} . Here, we have explicitly scaled the coupling of the four-fermion interaction by the number of components, so that the coupling constant g can be kept constant when taking the 't Hooft limit $N \rightarrow \infty$. Note that the Lagrangian is symmetric regarding the discrete chiral transform $\psi \rightarrow \gamma^5 \psi$. This symmetry would be explicitly broken by a mass term $\propto \bar{\psi} \psi$, which, under the given transform, passes into $-\bar{\psi} \psi$.

To apply worldline numerics, the Euclidian action in terms of Euclidean quantities is required. Notwithstanding the original studies in $D = 1 + 1$ dimensions, aiming at the $D = 2 + 1$ dimensional model, we let the number of dimensions initially unspecified, $D = d + 1$. We Wick rotate the time integral in the Minkowskian action from the real axis onto the imaginary axis,

$$S_M = \int_{-\infty}^{\infty} dx^0 \int d^d x \mathcal{L}_M = \int_{i\infty}^{-i\infty} dx^0 \int d^d x \mathcal{L}_M, \quad (8.3)$$

and introduce the Euclidean time $x_D := ix^0$:

$$S_M = -i \int d^d x \int_{-\infty}^{\infty} dx_D \left(\bar{\psi} i \not{\partial} \psi + \frac{g^2}{2N} (\bar{\psi} \psi)^2 \right) \quad (8.4)$$

$$= -i \int d^D x_E \left(\psi^\dagger \gamma^0 i (\gamma^0 \partial_0 - \dots) \psi + \frac{g^2}{2N} (\psi^\dagger \gamma^0 \psi)^2 \right). \quad (8.5)$$

With the Euclidean counterpart of the γ_0 matrix, $\gamma_D := -i\gamma^0$, this reads

$$S_M = i \int d^D x_E \left(- \underbrace{\psi^\dagger \gamma_D}_{\not{\psi}_E} (\dots + \underbrace{\gamma_D \partial_D}_{\not{\partial}_E}) \psi + \frac{g^2}{2N} (\psi^\dagger \gamma_D \psi)^2 \right), \quad (8.6)$$

so that we finally obtain the Euclidean action

$$S_E = -i S_M = \int d^D x_E \left(- \not{\psi}_E \not{\partial}_E \psi + \frac{g^2}{2N} (\not{\psi}_E \psi)^2 \right). \quad (8.7)$$

In the following, we exclusively use Euclidean quantities and omit the subscript E.

8.2 Auxiliary field

In order to perform a Hubbard-Stratonovich transformation, we introduce an auxiliary scalar field into the quantum field theoretic description of the fermion field, provided by the functional integral

$$Z = \int \mathcal{D}\bar{\psi} \mathcal{D}\psi e^{-S} \quad (8.8)$$

$$= \int \mathcal{D}\bar{\psi} \mathcal{D}\psi e^{-\int d^D x \left(-\bar{\psi} \not{\partial} \psi + \frac{g^2}{2N} (\bar{\psi} \psi)^2 \right)}. \quad (8.9)$$

For that purpose, we use the identity (assuming the path integral to be suitably normalised)

$$1 \equiv \int \mathcal{D}\sigma e^{-\int d^D x \left(\frac{\sqrt{N}}{\sqrt{2g}} \sigma - \frac{ig}{\sqrt{2N}} \bar{\psi} \psi \right)^2} \quad (8.10)$$

$$= \int \mathcal{D}\sigma e^{-\int d^D x \left(\frac{N}{2g^2} \sigma^2 - i\sigma \bar{\psi} \psi - \frac{g^2}{2N} (\bar{\psi} \psi)^2 \right)}, \quad (8.11)$$

so that we can rewrite the coupling term in Eq. (8.9) as

$$e^{-\int d^D x \frac{g^2}{2N} (\bar{\psi}\psi)^2} = \int \mathcal{D}\sigma e^{-\int d^D x \left(\frac{N}{2g^2} \sigma^2 - i\sigma \bar{\psi}\psi \right)}. \quad (8.12)$$

Therewith, the generating functional reads

$$Z = \int \mathcal{D}\bar{\psi} \mathcal{D}\psi \mathcal{D}\sigma e^{-\int d^D x \left(-\bar{\psi} \not{\partial} \psi + \frac{N}{2g^2} \sigma^2 - i\sigma \bar{\psi}\psi \right)} \quad (8.13)$$

$$= \int \mathcal{D}\sigma e^{-\int d^D x \frac{N}{2g^2} \sigma^2} \int \mathcal{D}\bar{\psi} \mathcal{D}\psi e^{-\int d^D x \bar{\psi} (-\not{\partial} - i\sigma) \psi}. \quad (8.14)$$

Actually, we have broken up the four fermion interaction and introduced a force-mediating field. The functional integral over the original fermion field now is Gaussian and the fermion field can be integrated out,

$$Z = \int \mathcal{D}\sigma e^{-\int d^D x \frac{N}{2g^2} \sigma^2} \det(-\not{\partial} - i\sigma)^N \quad (8.15)$$

$$= \int \mathcal{D}\sigma e^{-N \left(\int d^D x \frac{1}{2g^2} \sigma^2 - \text{tr} \ln(-\not{\partial} - i\sigma) \right)}. \quad (8.16)$$

We conclude that the scalar field σ has the action

$$S[\sigma] = \int d^D x \frac{N}{2g^2} \sigma^2 - N \text{tr} \ln(-\not{\partial} - i\sigma). \quad (8.17)$$

This action, and therewith the exponent in Eq. (8.16), scale linearly with the number of fermion components N . That means, in the limit $N \rightarrow \infty$ only the classical field, the minimum of the Euclidean action Eq. (8.17), contributes to the functional integral in Eq. (8.16) and the quantum theoretic description passes into a classical one. In general, the classical field is non-zero and thus the action in the exponent of Eq. (8.13) obtains a mass term for the fermion field. Consequently, the chiral symmetry of the Lagrangian Eq. (8.2) can be spontaneously broken in the large N limit.

The expectation value of the scalar field is

$$\langle \sigma \rangle = \int \mathcal{D}\sigma \, \sigma \, e^{-S[\sigma]} \quad (8.18)$$

$$= \int \mathcal{D}\sigma \, \sigma \, e^{-\int d^D x \frac{N}{2g^2} \sigma^2} \int \mathcal{D}\bar{\psi} \mathcal{D}\psi \, e^{-\int d^D x \bar{\psi}(-\not{\partial} - i\sigma)\psi} \quad (8.19)$$

$$= \int \mathcal{D}\sigma \, \left(-\frac{g^2}{N} \frac{\delta}{\delta \sigma} e^{-\int d^D x \frac{N}{2g^2} \sigma^2} \right) \int \mathcal{D}\bar{\psi} \mathcal{D}\psi \, e^{-\int d^D x \bar{\psi}(-\not{\partial} - i\sigma)\psi} \quad (8.20)$$

and integrating by parts yields

$$\langle \sigma \rangle = \int \mathcal{D}\sigma \, e^{-\int d^D x \frac{N}{2g^2} \sigma^2} \int \mathcal{D}\bar{\psi} \mathcal{D}\psi \, \frac{g^2}{N} \frac{\delta}{\delta \sigma} e^{-\int d^D x \bar{\psi}(-\not{\partial} - i\sigma)\psi} \quad (8.21)$$

$$= \int \mathcal{D}\sigma \, e^{-\int d^D x \frac{N}{2g^2} \sigma^2} \int \mathcal{D}\bar{\psi} \mathcal{D}\psi \, \frac{g^2}{N} i \bar{\psi} \psi \, e^{-\int d^D x \bar{\psi}(-\not{\partial} - i\sigma)\psi} \quad (8.22)$$

$$= i \frac{g^2}{N} \int \mathcal{D}\bar{\psi} \mathcal{D}\psi \, \bar{\psi} \psi \, e^{-S[\bar{\psi}, \psi]} \quad (8.23)$$

$$= i \frac{g^2}{N} \langle \bar{\psi} \psi \rangle. \quad (8.24)$$

Thus,

$$\langle \sigma \rangle = i \frac{g^2}{N} \langle \bar{\psi} \psi \rangle \equiv \frac{g^2}{N} \langle \bar{\psi}_M \psi \rangle. \quad (8.25)$$

In the large- N limit, the σ field and its expectation value are identical and we can replace $\langle \sigma \rangle$ by σ .

Our aim is to evaluate the $\text{tr} \ln$ term in the action Eq. (8.17) with worldline numerics to study the classical field σ , which acts as a classical background potential, interacting with the fluctuating fermion field. As a constant (though infinite) prefactor of the action, the flavour number N has no effect on the dynamics of the classical field and will be omitted in the following.

8.3 Worldline formalism

The argument of the logarithm in Eq. (8.17) is linear in the “kinetic” term $-\not{\partial}$. For worldline numerics, the kinetic term in the functional trace has to be quadratic, since only in that case it will translate into the Gaussian weight factor for the loop ensemble. However, the operator $-\not{\partial} - i\sigma$ has the same spectrum as $\not{\partial} - i\sigma$, as can be verified

by applying γ_5 on both sides of the Eigenvalue equation. Consequently, the trace in Eq. (8.17) has the same value, if the sign of the kinetic term is switched and we can reason

$$\text{tr} \ln(-\not{\partial} - i\sigma) = \text{tr} \ln(\not{\partial} - i\sigma) \quad (8.26)$$

$$= \frac{1}{2} (\text{tr} \ln(-\not{\partial} - i\sigma) + \text{tr} \ln(\not{\partial} - i\sigma)) \quad (8.27)$$

$$= \frac{1}{2} \text{tr} \ln((-\not{\partial} - i\sigma)(\not{\partial} - i\sigma)) \quad (8.28)$$

$$\stackrel{\{\gamma_k, \gamma_l\} = -2\delta_{kl}}{=} \frac{1}{2} \text{tr} \ln(\partial^2 - \sigma^2 + i\not{\partial}\sigma - i\sigma\not{\partial}) \quad (8.29)$$

$$= \frac{1}{2} \text{tr} \ln(\partial^2 - \sigma^2 + i(\not{\partial}\sigma)) \quad (8.30)$$

$$= \frac{1}{2} \text{tr} \ln(\partial^2 - V). \quad (8.31)$$

Here, we have abbreviated the potential formed by the σ dependent terms with $V(x) := \sigma^2 - i(\not{\partial}\sigma)$. After shifting the whole expression by the σ independent term $-(1/2)\text{tr} \ln(\partial^2)$, so that it vanishes for $V \equiv 0$, a comparison with Eq. (3.9) in chapter 3 allows us to immediately write down the corresponding worldline expression, Eq. (3.15) with $m = 0$:

$$\frac{1}{2} \text{tr} \ln\left(\frac{-\partial^2 + V}{-\partial^2}\right) = -\frac{1}{2} \frac{1}{(4\pi)^{D/2}} \int_{1/\Lambda^2}^{\infty} \frac{dT}{T^{1+D/2}} \int d^D x_{\text{CM}} \text{tr}_{\gamma} \langle \mathbf{P} e^{-\int_0^T d\tau V(x(\tau))} - 1 \rangle. \quad (8.32)$$

Two fermion-specific peculiarities have been taken into account here: the γ trace tr_{γ} remains when rewriting the trace as in Eq. (3.10) and the path ordering, denoted by \mathbf{P} , has to be obeyed when introducing the path integral as in Eq. (3.12), since the potential now contains the non-commuting Dirac matrices. The expectation value again is the path integral over closed paths with centre of mass x_{CM} (cf. Eq. (3.14)),

$$\langle \dots \rangle = \int \mathcal{D}x \dots e^{-\int_0^T d\tau \dot{x}^2/4}, \quad (8.33)$$

which is supposed to be normalised to $\langle 1 \rangle = 1$. Reinserting the definition of the potential V into Eq. (8.32) yields

$$\begin{aligned} & \frac{1}{2} \text{tr} \ln \left(\frac{-\partial^2 + V}{-\partial^2} \right) \\ &= -\frac{1}{2} \frac{1}{(4\pi)^{D/2}} \int_{1/\Lambda^2}^{\infty} \frac{dT}{T^{1+D/2}} \int d^D x_{\text{CM}} \langle e^{-\int_0^T d\tau \sigma^2} \text{tr}_\gamma \mathbf{P} e^{i \int_0^T d\tau (\not{\partial} \sigma)} - d_\gamma \rangle, \end{aligned} \quad (8.34)$$

where $d_\gamma = \text{tr}_\gamma 1$ is the dimensionality of the Dirac algebra (in even dimensions and for irreducible representations $d_\gamma = 2^{D/2}$). Since the γ trace over any product of an odd number of γ matrices is zero, only even powers of the second exponential function do contribute to the final result and it is convenient to replace it by a hyperbolic cosine:

$$\begin{aligned} & \frac{1}{2} \text{tr} \ln \left(\frac{-\partial^2 + V}{-\partial^2} \right) \\ &= -\frac{1}{2} \frac{1}{(4\pi)^{D/2}} \int_{1/\Lambda^2}^{\infty} \frac{dT}{T^{1+D/2}} \int d^D x_{\text{CM}} \langle e^{-\int_0^T d\tau \sigma^2} \text{tr}_\gamma \mathbf{P} \cosh \left(i \int_0^T d\tau (\not{\partial} \sigma) \right) - d_\gamma \rangle. \end{aligned} \quad (8.35)$$

Finally, we restore the integral expression in Eq. (8.17) (but, as discussed, omit the overall factor N) to obtain the full unrenormalised action for the scalar field σ ,

$$\begin{aligned} S[\sigma] = & \int d^D x \left(\frac{1}{2g^2} \sigma^2 + \right. \\ & \left. + \frac{1}{2} \frac{1}{(4\pi)^{D/2}} \int_{1/\Lambda^2}^{\infty} \frac{dT}{T^{1+D/2}} \langle e^{-\int_0^T d\tau \sigma^2} \text{tr}_\gamma \mathbf{P} \cosh \left(i \int_0^T d\tau (\not{\partial} \sigma) \right) - d_\gamma \rangle \right), \end{aligned} \quad (8.36)$$

where we have dropped the subscript CM from the centre of mass x_{CM} .

This worldline expression is explicitly valid for an arbitrary number of dimensions D . Of course, the actual number has to be taken into account for renormalisation. Beyond the original studies in 1 + 1 dimensions, the Gross-Neveu model is renormalisable to all orders in a $1/N$ expansion in 2 + 1 dimensions [91]. An intriguing question is, whether an equally rich phase diagram as for the 1 + 1 dimensional model and in particular a crystalline phase can be found for the 2 + 1 dimensional model. The worldline expression Eq. (8.36) is a promising starting point for further studies in this regard.

Chapter 9

Worldline numerics in two dimensions

The Gross-Neveu model in two dimensions has been a long-serving object of study and is well understood today. We use the two dimensional model as benchmark for the numerical evaluation of the worldline expression derived in the previous chapter.

9.1 Renormalisation

The ultra-violet behaviour of the theory is determined by the proptime integrand at small proptimes T . Since the spatial extension of the loop ensembles scales with the factor \sqrt{T} , the worldline expectation-value for small proptimes is determined by very condensed loop clouds. Thus, in the limit $T \rightarrow \infty$, a given loop ensemble does only probe the local value of the potential σ . For this reason, without loss of generality, we can renormalise the worldline expression Eq. (8.36) in $D = 2$ considering a constant σ potential.

The hyperbolic-cosine term in Eq. (8.36) then is equal to one, so that (with $D = 2$) the action becomes

$$S[\sigma] = \int d^2x \left(\frac{1}{2g^2} \sigma^2 + \frac{1}{4\pi} \int_{1/\Lambda^2}^{\infty} \frac{dT}{T^2} \langle e^{-\int_0^T d\tau \sigma^2} - 1 \rangle \right). \quad (9.1)$$

Obviously, the τ integral in the exponent is equal to $T\sigma^2$ for any path of the expectation value, which therefore is obsolete,

$$S[\sigma] = \int d^2x \left(\frac{1}{2g^2} \sigma^2 + \frac{1}{4\pi} \int_{1/\Lambda^2}^{\infty} \frac{dT}{T^2} (e^{-T\sigma^2} - 1) \right). \quad (9.2)$$

We integrate the T integral by parts to obtain

$$S[\sigma] = \int d^2x \left(\frac{1}{2g^2} \sigma^2 + \frac{1}{4\pi} \left(\Lambda^2 (e^{-\frac{\sigma^2}{\Lambda^2}} - 1) - \sigma^2 \int_{1/\Lambda^2}^{\infty} \frac{dT}{T} e^{-T\sigma^2} \right) \right) \quad (9.3)$$

$$= \int d^2x \left(\frac{1}{2g^2} \sigma^2 + \frac{1}{4\pi} \left(\Lambda^2 (e^{-\frac{\sigma^2}{\Lambda^2}} - 1) + \sigma^2 \text{Ei}\left(-\frac{\sigma^2}{\Lambda^2}\right) \right) \right). \quad (9.4)$$

Expanding the Λ dependent terms,

$$\Lambda^2 (e^{-\frac{\sigma^2}{\Lambda^2}} - 1) = -\sigma^2 + \frac{1}{2} \frac{\sigma^4}{\Lambda^2} + \dots \quad (9.5)$$

$$\sigma^2 \text{Ei}\left(-\frac{\sigma^2}{\Lambda^2}\right) = \sigma^2 \left(C + \ln\left(\frac{\sigma^2}{\Lambda^2}\right) - \frac{\sigma^2}{\Lambda^2} + \dots \right), \quad (9.6)$$

we obtain the action for $\Lambda^2 \gg \sigma^2$:

$$S = \int d^2x \left(\frac{1}{2g^2} \sigma^2 + \frac{1}{4\pi} \sigma^2 \left(-1 + C + \ln\left(\frac{\sigma^2}{\Lambda^2}\right) \right) \right). \quad (9.7)$$

We introduce the scale μ ,

$$S = \int d^2x \left(\frac{1}{2g_\Lambda^2} \sigma^2 + \frac{1}{4\pi} \sigma^2 \left(-1 + C + \ln\left(\frac{\sigma^2}{\mu^2}\right) + \ln\left(\frac{\mu^2}{\Lambda^2}\right) \right) \right), \quad (9.8)$$

and define the running coupling $g(\mu)$ by Coleman-Weinberg renormalisation conditions,

$$\left. \frac{\partial^2 \mathcal{L}}{\partial \sigma^2} \right|_{\sigma=\mu} = \frac{1}{g(\mu)^2}, \quad (9.9)$$

where \mathcal{L} is the integrand in Eq. (9.8), $S = \int d^2x \mathcal{L}$. The running coupling evaluates to

$$\frac{1}{g(\mu)^2} = \left. \frac{\partial^2}{\partial \sigma^2} \left(\frac{1}{2g_\Lambda^2} \sigma^2 + \frac{1}{4\pi} \sigma^2 \left(-1 + C + \ln\left(\frac{\sigma^2}{\Lambda^2}\right) \right) \right) \right|_{\sigma=\mu} \quad (9.10)$$

$$= \left. \frac{\partial}{\partial \sigma} \left(\frac{1}{g_\Lambda^2} \sigma + \frac{1}{2\pi} \sigma \left(C + \ln\left(\frac{\sigma^2}{\Lambda^2}\right) \right) \right) \right|_{\sigma=\mu} \quad (9.11)$$

$$= \frac{1}{g_\Lambda^2} + \frac{1}{2\pi} \left(C + \ln \frac{\mu^2}{\Lambda^2} \right) + \frac{1}{\pi} \quad (9.12)$$

$$= \frac{1}{g_\Lambda^2} + \frac{1}{2\pi} \left(C + 2 + \ln \frac{\mu^2}{\Lambda^2} \right). \quad (9.13)$$

Differentiating with respect to the scale μ ,

$$\partial_\mu \frac{1}{g(\mu)^2} = -\frac{1}{g(\mu)^4} \partial_\mu g(\mu)^2 = \frac{1}{\pi\mu}, \quad (9.14)$$

we obtain the β function:

$$\beta_{g^2} \equiv \mu \partial_\mu g(\mu)^2 = -\frac{1}{\pi} g(\mu)^4, \quad (9.15)$$

which is negative, reflecting asymptotic freedom. Inserting the running coupling into the action Eq. (9.8) yields the renormalised action

$$S = \int d^2x \left(\frac{1}{2g(\mu)^2} \sigma^2 + \frac{\sigma^2}{4\pi} \left(\ln \frac{\sigma^2}{\mu^2} - 3 \right) \right). \quad (9.16)$$

The minimum of the action with respect to the value σ defines the fermion mass, which, exploiting the minimum condition $\partial S / \partial \sigma|_{\sigma=m} = 0$, evaluates to

$$m = \mu e^{-\pi/g(\mu)^2+1}. \quad (9.17)$$

This mass is independent of the scale μ , $\mu \partial_\mu m_0^2 = 0$, and defines our physical scale. Writing μ^2 in Eq. (9.16) in terms of m , the renormalised action finally reads

$$S = \int d^2x \left(\frac{1}{2g(\mu)^2} \sigma^2 + \frac{\sigma^2}{4\pi} \left(\ln \frac{\sigma^2}{m} - 1 - \frac{2\pi}{g(\mu)^2} \right) \right) \quad (9.18)$$

$$= \int d^2x \frac{\sigma^2}{4\pi} \left(\ln \frac{\sigma^2}{m^2} - 1 \right). \quad (9.19)$$

At the minimum, $\sigma = m$, the integrand has the value $-m^2/(4\pi)$. To obtain a finite minimal action it can be convenient to subtract this field independent term:

$$S = \int d^2x \left(\frac{\sigma^2}{4\pi} \left(\ln \frac{\sigma^2}{m^2} - 1 \right) + \frac{m^2}{4\pi} \right). \quad (9.20)$$

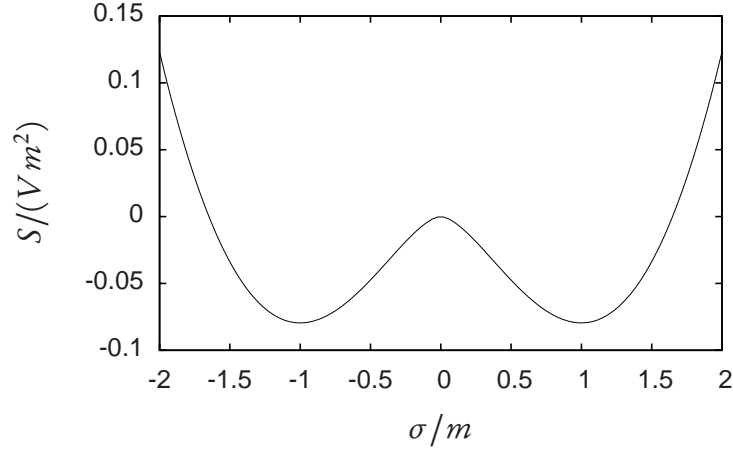


Figure 9.1: The renormalised Euclidean action for the constant potential versus the potential's value.

In Fig. 9.1, the integrand S/V is plotted (without the subtraction), showing the typical Mexican hat shape (in one dimension) responsible for spontaneous symmetry breaking.

The cut-off dependent coupling in terms of the mass m is

$$\frac{1}{g_\Lambda^2} = \frac{1}{2\pi} \left(\ln \frac{\Lambda^2}{m^2} - C \right). \quad (9.21)$$

It follows, up to order m^2/Λ^2 ,

$$\frac{1}{g_\Lambda^2} = \frac{1}{2\pi} \int_{1/\Lambda^2}^{\infty} \frac{dT}{T} e^{-m^2 T} \quad (9.22)$$

$$= -\frac{1}{2\pi} \left(1 + \frac{1}{m^2} \int_{1/\Lambda^2}^{\infty} \frac{dT}{T^2} (e^{-m^2 T} - 1) \right). \quad (9.23)$$

Insertion into the general, unrenormalised worldline expression Eq. (8.36) at $D = 2$ yields

$$S = \int d^2x \frac{1}{4\pi} \left(-\sigma^2 + \int_0^\infty \frac{dT}{T^2} \left(\frac{1}{2} \left\langle e^{-\int_0^T d\tau \sigma^2} \text{tr}_\gamma \text{P} \cosh \left(i \int_0^T d\tau (\not{D}\sigma) \right) \right\rangle - \frac{\sigma^2}{m^2} (e^{-m^2 T} - 1) - 1 \right) \right). \quad (9.24)$$

We have sent $\Lambda \rightarrow \infty$ here, since all divergencies have been removed.

9.2 Spatially varying potentials

For a potential varying in x_1 direction, we make the following considerations: With $\partial_2 \sigma = 0$ the path ordering in Eq. (11.17) is redundant. Exploiting $\gamma_\mu^2 = -1$, the tr_γ term reads

$$\text{tr}_\gamma P \cosh(i \int_0^T d\tau (\not{\partial} \sigma)) = 2 \cosh(\int_0^T d\tau \sigma'(x(\tau))) \quad (9.25)$$

and the complete renormalised action

$$S = \int d^2x \frac{1}{4\pi} \left(-\sigma^2 + \int_0^\infty \frac{dT}{T^2} \times \right. \\ \left. \times \left(\left\langle e^{-\int_0^T d\tau \sigma^2} \cosh(\int_0^T d\tau \sigma'(x(\tau))) \right\rangle - \frac{\sigma^2}{m_0^2} (e^{-m_0^2 T} - 1) - 1 \right) \right). \quad (9.26)$$

It is convenient to combine exponential and hyperbolic function in the expectation value by defining $V_\pm := \sigma^2 \pm \sigma'$ and writing

$$S = \frac{1}{2} \int d^2x (\mathcal{L}_+ + \mathcal{L}_-), \quad (9.27)$$

where

$$4\pi \mathcal{L}_\pm := -V_\pm + \int_0^\infty \frac{dT}{T^2} \left(\left\langle e^{-\int d\tau V_\pm} \right\rangle - \frac{V_\pm}{m^2} (e^{-m^2 T} - 1) - 1 \right). \quad (9.28)$$

If common-point (CP) loops are used to evaluate the expectation value, i.e. if we employ loop ensembles, in which all loops have a common starting and end point instead of a common centre of mass,* we can write the expectation value as quantum mechanical transition amplitude at imaginary time,

$$\left\langle e^{-\int d\tau V_\pm} \right\rangle = \frac{\langle x | e^{-T(-\partial_1^2 + V_\pm)} | x \rangle}{\langle x | e^{-T(-\partial_1^2)} | x \rangle} = \sqrt{4\pi T} \langle x | e^{-TH_\pm} | x \rangle, \quad (9.29)$$

*This just corresponds to a different splitting of the path integral over *any* closed loops: $\int_{x(o)=x(T)} d^D x_{\text{CM}} \mathcal{D}x = \int d^D x_{\text{CM}} \int_{x(o)=x(T), \text{CM } x_{\text{CM}}} \mathcal{D}x = \int d^D x \int_{x(o)=x(T)=x} \mathcal{D}x$.

where $H_{\pm} = -\partial_1^2 + V_{\pm}$ and x is the common point. The transition amplitude in turn can be written as sum over the eigen modes ψ_n of the Hamiltonian H_{\pm} :

$$\langle x|e^{-TH_{\pm}}|x\rangle = \sum_n \langle x|e^{-TH_{\pm}}|\psi_n\rangle \langle \psi_n|x\rangle \quad (9.30)$$

$$= \sum_n \langle x|\psi_n\rangle \langle \psi_n|x\rangle e^{-TE_{\pm n}} \quad (9.31)$$

$$= \sum_n |\psi_n(x)|^2 e^{-TE_{\pm n}}, \quad (9.32)$$

where $E_{\pm n}$ denotes the eigenvalues of the Hamiltonian. From this, we learn about the large T behaviour of the worldline expectation value, which depends on the existence of a zero mode. If the Hamiltonian H_{\pm} has no zero mode, all terms of the sum are exponentially damped and the expectation value vanishes. In contrast, if a zero mode exists, the transition amplitude Eq. (9.32) goes to the constant value $|\psi_0(x)|^2$ and the expectation value is proportional to \sqrt{T} ,

$$\langle e^{-\int d\tau V_{\pm}} \rangle \xrightarrow{T \rightarrow \infty} \sqrt{4\pi T} |\psi_0(x)|^2 \quad (9.33)$$

As we will see below, it is not easy to reproduce this increase numerically.

9.3 Single kink

Potentials involving kinks have been studied soon after the Gross-Neveu model has been introduced [92] and even the crystalline phase found only recently [90] is a lattice, composed of kink-antikink pairs.

At first, we study the single kink potential. Following up the last section, this is a simple example for a potential with zero mode. The potential (in units of m) is given by

$$\sigma = \tanh(x). \quad (9.34)$$

The corresponding V_{\pm} potentials are

$$V_- = 1 - \frac{2}{\cosh^2(x)} \quad (9.35)$$

$$V_+ = 1. \quad (9.36)$$

The V_- potential probes a precarious aspect of the worldline numerical evaluation: Close to the origin, the potential is negative, see Fig. 9.2, and consequently the

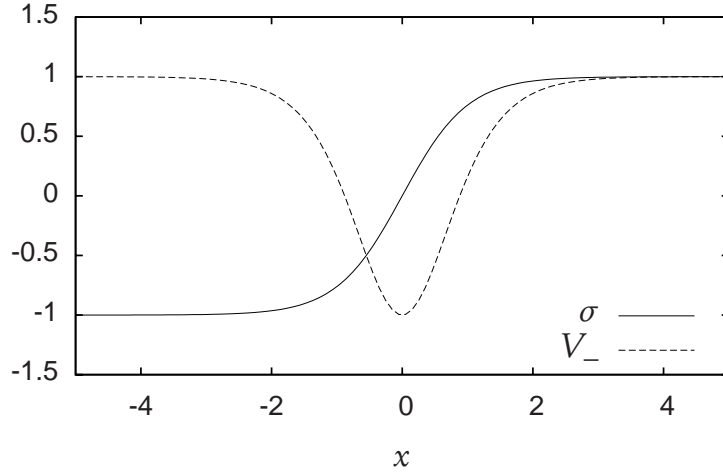


Figure 9.2: The kink potential σ and the corresponding V_- potential. A small loop sitting at the origin V_- gathers only negative V_- values.

exponent in Eq. (9.29) is positive for certain loops. The expectation value in terms of unit loops,

$$\langle e^{-\int_0^T d\tau V_-(x(\tau))} \rangle = \langle e^{-T \int_0^1 dt V_-(x_{\text{CM/CP}} + \sqrt{T}y(t))} \rangle, \quad (9.37)$$

raises the suspicion, that a small loop, for which the scaled loop $\sqrt{T}y(t)$ is still small and close to the origin, even if the T value is relatively large, could dominate the expectation value. A similar overlap problem has been studied in [93].

The analytically known transition amplitude [94],

$$\langle e^{-\int d\tau V_-} \rangle = \sqrt{\pi T} \operatorname{sech}^2 x (1 - \operatorname{erfc}(\sqrt{T})) + e^{-T}, \quad (9.38)$$

is, as expected, proportional to \sqrt{T} in the large propertime limit. Due to the large T behaviour of the argument in Eq. (9.37), it is immediately clear that this proportionality cannot be recovered using a finite and discrete loop ensemble. Any unit loop, scaled by a sufficiently large factor \sqrt{T} , will not resolve the negative peak of V_- . In that case, the exponent in Eq. (9.37) will evaluate to $-T$. Thus, for any finite, discrete loop ensemble the expectation value decreases exponentially in the large T limit.

In Fig. 9.3 the analytical result for the expectation value at the origin is compared to the worldline numeric result for two loop ensembles with different numbers of loops. For small propertimes, the results agree nicely. However, for large T values, the numerical results do indeed decrease exponentially; the values obtained using a smaller loop ensemble decrease more rapidly than the result computed with more loops. In this large T region, the statistical errors are much smaller than the real error, which is typical for an overlap problem.

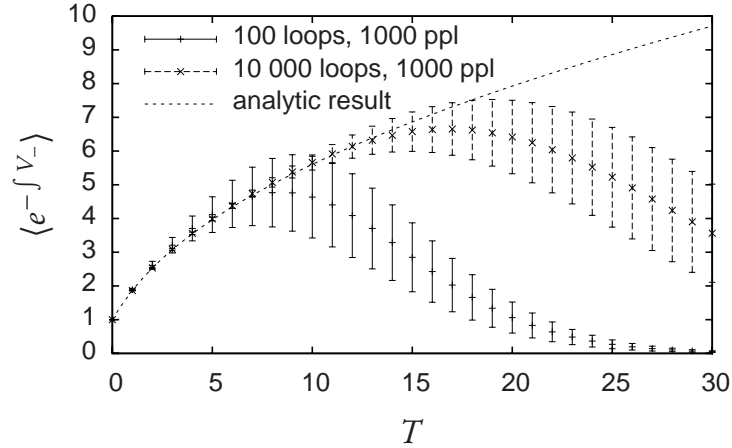


Figure 9.3: The CP-loop expectation value at the centre of a kink potential versus the proper time T . For large proper times, the analytic result is proportional to \sqrt{T} . This is rediscovered by worldline numerics only up to a certain proper time value, depending on the number of loops employed.

We conclude, at least for large proper time values the overlap problem becomes manifest and can only be shifted to larger T values by using a larger loop ensemble, but it cannot be eliminated within the unit-loop construction.

The question arises, if this has an impact on the further computations. In the complete expression for \mathcal{L}_- , Eq. (9.28), the proper time integrand is multiplied by the factor of $1/T^2$, which suppresses the integrand for large T , even despite the \sqrt{T} increase of the expectation value.

This question can be studied carefully considering a kink-antikink pair. The single kink potential is a special case of this more general potential, it is recovered in the limit of an infinite distance between kink and antikink. Regarding the large T behaviour, the single kink turns out to represent the worst case of all kink-antikink configurations.

9.4 Kink-antikink

A kink and an antikink separated by the distance b are given by the potential

$$\sigma(x) = \kappa(\tanh(\kappa x_1) - \tanh(\kappa x_1 + b) + \coth(b)). \quad (9.39)$$

The parameter κ defines the width of kink and antikink, respectively. It has the unit of a mass, but throughout this section, all quantities are supposed to be given in units of the physical mass m , defined by the constant-field solution, so that any quantity can be treated as pure number. For $|x_1| \rightarrow \infty$, the potential goes to $\kappa \coth(b)$. As discussed

below, it is convenient to restrict our studies to potentials with $\kappa \coth(b) \equiv 1$. In the limit $b \rightarrow \infty$ we obtain a single kink, $\sigma(x) = \kappa \tanh(\kappa x_1)$, which in turn is equal to the kink potential of the previous section, Eq. (9.34), if $\kappa = 1$. The potentials V_+ and V_- differ only by a spatial shift,

$$V_{\pm} = \kappa^2 \coth(b)^2 - 2\kappa^2 \left\{ \begin{array}{l} \text{sech}^2(\kappa x_1 + b) \\ \text{sech}^2(\kappa x_1) \end{array} \right\}, \quad (9.40)$$

consequently

$$S = \int d^2x \mathcal{L}_-. \quad (9.41)$$

Analytical evaluation of the expectation value Eq. (9.29) yields [94]

$$\langle e^{-\int d\tau V_-} \rangle = \kappa \text{sech}^2(\kappa x_1) \sqrt{\pi T} \text{erf}(\kappa \sqrt{T}) e^{-(\coth^2(b)-1)\kappa^2 T} + e^{-\kappa^2 \coth^2(b)T}, \quad (9.42)$$

where x_1 denotes the spatial coordinate of the common point. Insertion into Eq. (9.28) yields

$$4\pi \mathcal{L}_- = \kappa^2 \coth^2(b) \left(\ln \left(\kappa^2 \coth^2(b) \right) - 1 \right) + \kappa \text{sech}^2(\kappa x_1) \times \\ \times \left(2\kappa + \int_0^\infty \frac{dT}{T^2} \left(\sqrt{\pi T} \text{erf}(\kappa \sqrt{T}) e^{-(\coth^2(b)-1)\kappa^2 T} + 2\kappa (e^{-T} - 1) \right) \right). \quad (9.43)$$

The x_1 integral over the first, x_1 independent term on the right hand side is divergent, whereas the integral over the sech term is finite. Consequently, to minimize the action with respect to the parameters κ and b , one has to minimize the first summand in the first place. This term is minimal for $\kappa \coth(b) = 1$ and has the minimal value -1 , which is consistent with the fact that for large x_1 values the kink-antikink potential is a constant field with value $\kappa \coth(b)$ and with the constant field result (Eq. 9.19).

Under the assumption that $\kappa \coth(b) = 1$ is fulfilled, we can write b in terms of κ and Eq. (9.43) simplifies to

$$4\pi \mathcal{L}_- = -1 + \kappa \text{sech}(\kappa x_1) \times \\ \times \left(2\kappa + \int_0^\infty \frac{dT}{T^2} \left(\sqrt{\pi T} \text{erf}(\kappa \sqrt{T}) e^{-(1-\kappa^2)T} + 2\kappa (e^{-T} - 1) \right) \right). \quad (9.44)$$

As we have done in Eq. (9.20) in the constant field case, it is convenient to subtract

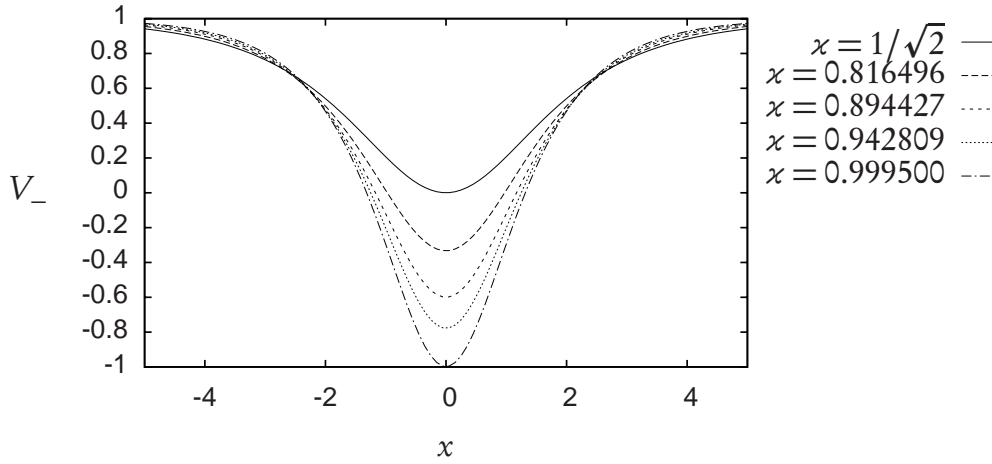


Figure 9.4: The potential V_- of the kink-antikink pair for five different values χ ; $\chi \coth(b) \equiv 1$ is kept fixed.

the constant -1 (which corresponds to $-m^2$):

$$4\pi\mathcal{L}_- = \chi \operatorname{sech}(\chi x_1) \left(2\chi + \int_0^\infty \frac{dT}{T^2} \left(\sqrt{\pi T} \operatorname{erf}(\chi\sqrt{T}) e^{-(1-\chi^2)T} + 2\chi (e^{-T} - 1) \right) \right). \quad (9.45)$$

The remaining free parameter χ determines the depth of the V_- potential. As we have already mentioned, $\chi = 1$ corresponds to the single kink potential. A value $\chi = 0$ yields a constant, positive potential. Intermediate values interpolate between both extremes; if χ is larger than $1/\sqrt{2}$, the potential becomes negative at the origin. But only for $\chi = 1$, there is a zero mode and the integrand in Eq. (9.45) is proportional to \sqrt{T} in the limit $T \rightarrow \infty$. Figure 9.4 shows the potential for five different χ values between $1/\sqrt{2}$ and 1.

The result of a worldline numeric computation for the five potentials in Fig. 9.4 is shown in Fig. 9.5. The computed value corresponds to the proptime integral in Eq. (9.45). In general, the negative peak of the potential is not an issue. Only for the largest χ value, $\chi = 0.995$, the algorithm has a severe problem to achieve convergence. The influence of the zero mode at $\chi = 1$ becomes noticeable, the exponential factor in the integrand of Eq. (9.45) decreases only weakly and the integral is dominated by large proptime values, at which the worldline numerical evaluation of the expectation value suffers from the overlap problem, as we have seen in Fig. 9.3.

Figure 9.6 shows the analytic proptime integral for all χ values between 0 and 1. Along with the overlap problem close to $\chi = 1$, the curve becomes very steep and the derivative finally diverges at $\chi = 1$. This means that a small change in the input parameter has a large impact on the final result. For example, the lowest potential

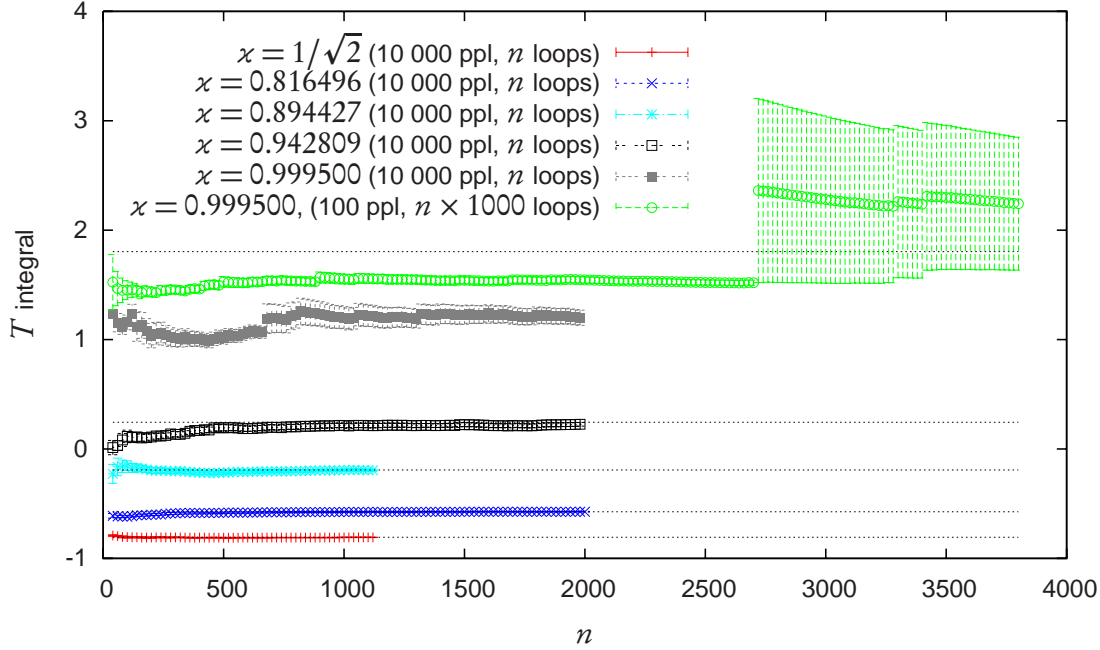


Figure 9.5: Convergence behaviour of the worldline-numerical result. The plot shows the numerical values corresponding to the proper-time integral Eq. (9.45) versus the number of loops employed, for the χ values in Fig. 9.4. The topmost values (green circles) are for the same χ value as the values immediately below (solid grey squares), but with the number of loops multiplied by a factor of 1000 (the number of points per loops is smaller, but in the smooth potential this has little impact). The dotted horizontal lines represent the analytic values. The error bars are the jackknife estimates and should provide reasonable values if the number of loops is larger than 1000. Evidently, this is not the case for the largest χ value. This indicates an overlap problem. At about 2 750 000 loops ($n = 2750$), we observe a huge jump of the result, apparently caused by the occurrence of one single very small loop.

in Fig. 9.4 ($\chi = 0.9995$) yields an integral value of 1.8044, compared to a value of 2 for $\chi = 1$. This amplification by a factor of 200 demands for a very precise numerical evaluation.

So far we have learnt that the worldline numerical evaluation of the action for a kink-antikink becomes difficult in the single-kink limit, mainly due to the zero mode of the single kink potential. However, even in the single-kink limit, the proper-time integrand can be computed very precisely up to a certain value, depending on the number of worldlines involved. Thus, a general solution to the zero-mode problem is the following: For a given coordinate x , the worldline expectation value has to be computed for proper-time values, at which the contribution of all non-zero modes in Eq. (9.32) is sufficiently suppressed. This may require a large loop ensemble, but has no principle limitation. To these values, we fit the simple function $a\sqrt{T}$ with only one fitting parameter a . Due to Eq. (9.33), the resulting value $a_{\text{fit}}(x)$ directly translates

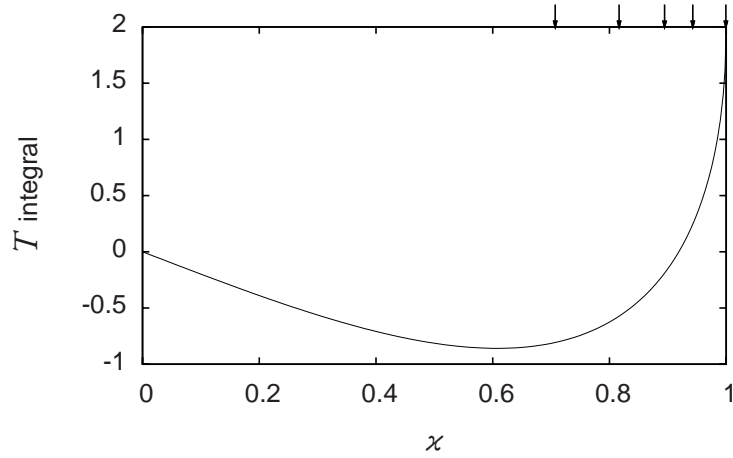


Figure 9.6: The analytical result for the T integral in Eq. (9.45) vs. the parameter χ . For $\chi = 1$, the integral is equal to 2, for larger values it diverges. The χ values of Fig. 9.4 and Fig. 9.5 are marked by small arrows at the top.

into the zero-mode value,

$$|\psi_0(x)|^2 = \frac{a_{\text{fit}}(x)}{\sqrt{4\pi}}. \quad (9.46)$$

For proper time values beyond the range of the fit, we can now use the fitted function,

$$\langle e^{-\int d\tau V_{\pm}} \rangle \xrightarrow{T \rightarrow \infty} a_{\text{fit}}(x_{\text{CP}}) \sqrt{T}, \quad (9.47)$$

and perform the proper time integral analytically.

A different approach to solve the overlap problem at large proper times is the use of hybrid Monte Carlo (HMC) methods [95, 96] to create loop ensembles, in which the distribution of the loops does not only take the kinetic term $\exp(-\int \dot{x}^2/4)$ into account, but also the potential term $\exp(-\int V_-)$ [97]. This guaranties that the ensemble contains only loops which dominantly contribute to the final result; for large proper times, these are small loops in the centre of the V_- potential.

We conclude, the presence of a zero mode is a solvable problem. However, we are mainly interested in periodic, crystal-like potentials, where kinks and antikinks have a finite distance and there is no zero mode at all. For those potentials, straight forward worldline numerics seems to be sufficient.

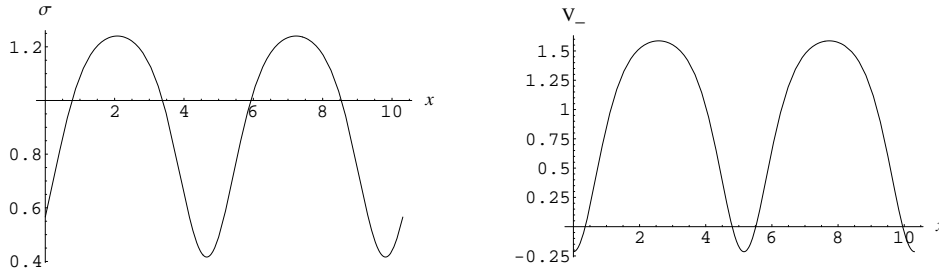


Figure 9.7: The potentials σ (Eq. (9.48)) and V_- (Eq. (9.49)) for $b = 1$, $\nu = 0.9$ and $m = \coth(1)$, in units of x .

9.5 Periodic array of kink-antikink pairs

Let us now consider a periodic array of kink-antikink pairs:

$$\sigma(x) = x^2 \left(\frac{\text{cn}(b; \nu) \text{dn}(b; \nu)}{\text{sn}(b; \nu)} + \nu \text{sn}(b; \nu) \text{sn}(xx; \nu) \text{sn}(xx + b; \nu) \right). \quad (9.48)$$

The functions cn , dn and sn are the basic Jacobi elliptic functions. The period is $2K(\nu)/x$, with the complete elliptic integral of the first kind K . It goes to infinity for $\nu \rightarrow 1$. In that case we recover the the simple kink-antikink potential.

The crystal phase of the Gross-Neveu model at finite temperature and chemical potential is of exactly this form, the values of the parameters b , x and ν depend on the temperature, the chemical potential and the fermion mass [90].

Again, the potentials V_+ and V_- differ only by a spatial shift:

$$V_{\pm} = x^2 \left(\frac{1}{\text{sn}^2(b; \nu)} - 1 + \nu - 2\nu \left\{ \begin{array}{c} \text{cn}^2(xx + b; \nu) \\ \text{cn}^2(xx; \nu) \end{array} \right\} \right). \quad (9.49)$$

In Fig. 9.7, the potentials σ and V_- are plotted for, in units of x , $m = \coth(1)$, $b = 1$ and $\nu = 0.9$. The CP-loop expectation value $\langle e^{-\int V_{\pm}} \rangle$ can be written in a closed analytic form [94]:

$$\langle e^{-\int V_{\pm}} \rangle = \sqrt{4\pi T} \left(\alpha(T) + \beta(T) \left\{ \begin{array}{c} \text{cn}^2(xx + b; \nu) \\ \text{cn}^2(xx; \nu) \end{array} \right\} \right) \quad (9.50)$$

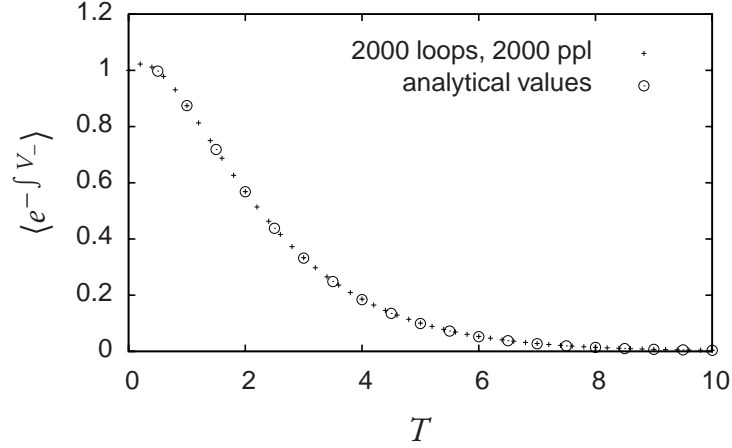


Figure 9.8: The worldline expectation-value versus the proptime in a minimum of the potential V_- of Fig. 9.7. The statistical error is too tiny to be plotted. Due to the lacking zero mode, the values decrease exponentially very early in contrast to the corresponding values for a single kink, Fig. 9.3.

with

$$\alpha(T) := e^{-x^2 \left(\frac{dn(b;\nu)}{sn(b;\nu)} \right)^2 T} \left(\frac{1}{\sqrt{4\pi T}} - \frac{x^2}{\sqrt{4\pi}} \int_0^T du \frac{1}{2\sqrt{T-u}} e^{-x^2(\nu-1/2)u} \times \right. \\ \left. \times \left((2\nu-1)I_0\left(\frac{x^2}{2}u\right) - I_1\left(\frac{x^2}{2}u\right) \right) \right) \quad (9.51)$$

and

$$\beta(T) := \frac{\nu x^2}{2} e^{-x^2 \left(\frac{dn(b;\nu)}{sn(b;\nu)} \right)^2 T} \int_0^T du \frac{e^{-x^2(\nu-1/2)u}}{\sqrt{\pi(T-u)}} I_0\left(\frac{x^2}{2}u\right). \quad (9.52)$$

Figure 9.8 shows the expectation value Eq. (9.50) versus the proptime in a minimum of the potential V_- of Fig. 9.7. Due to the lacking zero mode, the values decrease exponentially already for small proptimes, in contrast to the corresponding single kink result Fig. 9.3, and numeric and analytic results agree nicely. Even a small loop ensemble yields tiny errors.

The complete renormalised action reads [94]

$$S = \int d^2x \mathcal{L}_- = \frac{1}{4\pi} \int d^2x (-V_-(x) + A + B \operatorname{cn}^2(x)), \quad (9.53)$$

with

$$A := \chi^2 \left[2\nu - 1 + (ds^2 + 2\nu - 1) \ln \left(\frac{ds^2 \chi^2}{m^2} \right) + 2 \int_0^1 d\xi \frac{\sqrt{1-\xi}}{\xi} \times \right. \\ \left. \times \left(-ds^2 + (\nu - 1/2)\xi + \frac{ds^4}{\sqrt{(ds^2 - (1-\nu)\xi)(ds^2 + \nu\xi)}} \right) \right], \quad (9.54)$$

where

$$ds = \frac{\operatorname{dn}(b; \nu)}{\operatorname{sn}(b; \nu)}, \quad (9.55)$$

and

$$B := -2\nu\chi^2 \left[1 + \ln \left(\frac{ds^2 \chi^2}{m^2} \right) + \int_0^1 d\xi \frac{\sqrt{1-\xi}}{\xi} \times \right. \\ \left. \times \left(1 - \frac{ds^4}{\sqrt{(ds^2 - (1-\nu)\xi)(ds^2 + \nu\xi)}} \right) \right]. \quad (9.56)$$

Omitting the trivial integration along the x_2 axis in Eq. (9.53) and integrating over one period of the potential σ in x_1 direction, we obtain in units of χ for $b = 1$, $\nu = 0.9$ and $m = \operatorname{coth}(1)$

$$\int_0^{2K(0.9)} dx \mathcal{L}_- = -\frac{1}{4\pi} \left\{ \begin{array}{l} 6.81704 \\ 6.818 \pm 0.001 \end{array} \right\}. \quad (9.57)$$

where the upper value in braces is the analytic result, the lower one a worldline-numerical estimate with 20 000 CM loops of 2000 ppl each. In units of m , the spatial average of \mathcal{L}_- then is

$$\overline{\mathcal{L}_-} := \frac{\chi}{2K(0.9)} \int_0^{2K(0.9)/\chi} dx \mathcal{L}_- = -\frac{1}{4\pi} \left\{ \begin{array}{l} 0.766857 \\ 0.7669 \pm 0.0001 \end{array} \right\}. \quad (9.58)$$

Note that this is well above the corresponding value of the constant field solution, $-1/(4\pi)$ (cf. Eq. (9.19)).

With the same loop ensemble we study the slightly more challenging configuration $b = 2$, $\nu = 0.9$ and $m = \operatorname{coth}(2)$, which has deeper minima (see Fig. 9.9), and obtain

$$\int_0^{2K(0.9)} dx \mathcal{L}_- = -\frac{1}{4\pi} \left\{ \begin{array}{l} 0.499945 \\ 0.49 \pm 0.03 \end{array} \right\}, \quad (9.59)$$

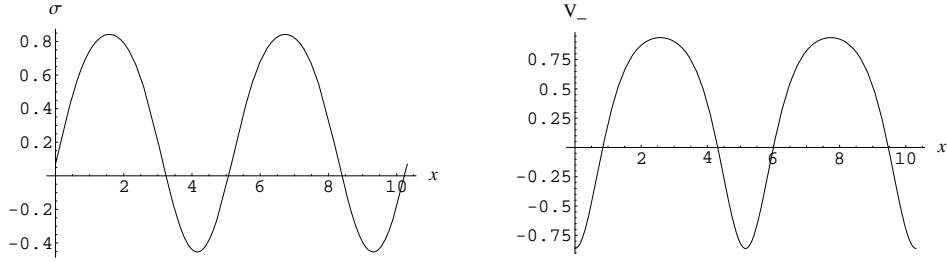


Figure 9.9: The potentials σ (Eq. (9.48)) and V_- (Eq. (9.49)) for $b = 2$, $\nu = 0.9$ and $m = \coth(2)$, in units of x .

with the spatial average (in units of m)

$$\overline{\mathcal{L}_-} = -\frac{1}{4\pi} \left\{ \begin{array}{l} 0.0901099 \\ 0.088 \pm 0.005 \end{array} \right\}. \quad (9.60)$$

The statistical error is larger, as one might have expected, but can be improved using a larger worldline ensemble. The agreement is still nice. The result is even further away from the minimal solution, the constant field with $\overline{\mathcal{L}_-} = -1/(4\pi)$.

So far, worldline numerics has turned out to perform well in computing actions of spatially varying potentials in the two dimensional Gross-Neveu model, in particular for periodic potentials without a zero mode. We will now introduce finite temperature and later finite chemical potential into our formalism.

Chapter 10

Temperature

Due to the fact that we already perform all computations in Euclidean time, introducing temperature in our formalism merely means to compactify our time x_2 (in D dimensions x_D). We restrict the Euclidean time x_2 to the interval $[0, \beta]$ and apply (due to the fermionic nature of the quantum field) anti-periodic boundary conditions. The figurative association, the cylinder with circumference β , formed from the x_1 - x_2 plane with coiled time dimension x_2 , is illustrated in Fig. 10.1.

For the *closed* worldlines on the cylindrical surface, this has a topological impact: a given loop now can be closed after being wrapped around the cylinder. That means, beside the “usual” loops with no winding, we now have to take all loops with any non-zero winding number n , which can be positive or negative, into account.

For this purpose, it is useful to write a given loop as sum of a loop with no winding, denoted by $\tilde{x}(\tau)$, and a translation in time direction which is linear in the proper time τ

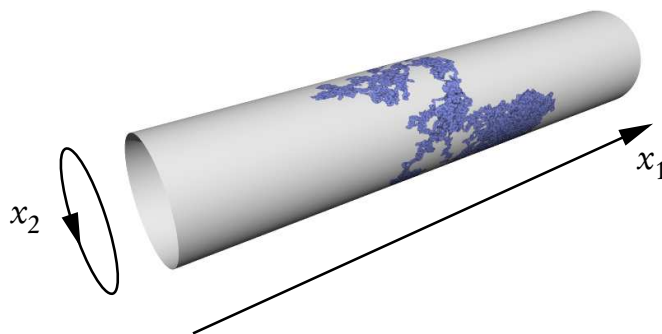


Figure 10.1: The Euclidean x_1 - x_2 plane with compactified time x_2 , illustrated as cylinder with circumference β . A closed worldline on the cylinder has a characteristic number of windings around the cylinder.

and runs from zero to a multiple of β ,

$$x(\tau) = (x_i(\tau)) = \left(\tilde{x}_i(\tau) + n\beta \frac{\tau}{T} \delta_{iD} \right). \quad (10.1)$$

The path integral over *all* closed worldlines can then be written as a path integral over loops with no winding and a sum over all winding numbers n :

$$\begin{aligned} \int_{x(0)=x(T)} \mathcal{D}x e^{-\int_0^T d\tau \frac{\dot{x}^2}{4}} \dots &= \sum_{n=-\infty}^{\infty} (-1)^n \int_{\tilde{x}(0)=\tilde{x}(T)} \mathcal{D}\tilde{x} e^{-\frac{1}{4} \int_0^T d\tau \left(\frac{d}{d\tau} (\tilde{x}_i(\tau) + n\beta \frac{\tau}{T} \delta_{iD}) \right)^2} \dots \\ &= \sum_{n=-\infty}^{\infty} (-1)^n \int_{\tilde{x}(0)=\tilde{x}(T)} \mathcal{D}\tilde{x} e^{-\frac{1}{4} \int_0^T d\tau \left(\dot{\tilde{x}}_i(\tau) + \frac{n\beta}{T} \delta_{iD} \right)^2} \dots \\ &= \sum_{n=-\infty}^{\infty} (-1)^n e^{-\frac{n^2 \beta^2}{4T}} \int_{\tilde{x}(0)=\tilde{x}(T)} \mathcal{D}\tilde{x} e^{-\int_0^T d\tau \frac{\dot{\tilde{x}}^2}{4}} \dots \end{aligned} \quad (10.2)$$

The alternating sign arises from the anti-periodic boundary conditions, $\langle x + \beta | x \rangle = -\langle x | x \rangle$. It would not be present, if the functional determinant of a bosonic field was to be computed, e.g. to study the Casimir effect for a scalar field at finite temperature. The dots denote an integrand which does not depend on the time x_D . Therewith, the worldline expectation-value is the same as before, but with the winding-number sum as prefactor,

$$\langle \dots \rangle \rightarrow \sum_{n=-\infty}^{\infty} (-1)^n e^{-\frac{n^2 \beta^2}{4T}} \langle \dots \rangle. \quad (10.3)$$

Insertion into the Eq. (8.36) yields the full (unrenormalised) action at finite temperature in D dimensions,

$$\begin{aligned} S[\sigma] = \int d^D x \left(\frac{1}{2g^2} \sigma^2 + \frac{1}{2(4\pi)^{D/2}} \int_{1/\Lambda^2}^{\infty} \frac{dT}{T^{1+D/2}} \left(\left(\sum_{n=-\infty}^{\infty} (-1)^n e^{-\frac{n^2 \beta^2}{4T}} \right) \times \right. \right. \\ \left. \left. \times \left\langle e^{-\int_0^T d\tau \sigma^2} \text{tr}_\gamma \text{P} \cosh \left(i \int_0^T d\tau (\not{D} \sigma) \right) \right\rangle - d_\gamma \right) \right). \end{aligned} \quad (10.4)$$

10.1 Symmetry restoration

Let us now utilise this expression to briefly rediscover the critical temperature, at which the constant solution σ of the two dimensional Gross-Neveu model goes to zero and chiral symmetry is restored.

For constant σ in $D = 2$ Eq. (10.4) reduces to

$$S = \int d^2x \left(\frac{1}{2g^2} \sigma^2 + \frac{1}{4\pi} \int_0^\infty \frac{dT}{T^2} \left(e^{-T\sigma^2} \sum_{n=-\infty}^{\infty} (-1)^n e^{-\frac{n^2\beta^2}{4T}} - 1 \right) \right), \quad (10.5)$$

and using the relation

$$\sum_{n=-\infty}^{\infty} e^{-\frac{4\pi^2 T}{\beta^2} (n+1/2)^2} = \frac{\beta}{\sqrt{4\pi T}} \sum_{n=-\infty}^{\infty} (-1)^n e^{-\frac{\beta^2}{4T} n^2}, \quad (10.6)$$

we obtain (without the zero field subtraction)

$$S = \int d^2x \left(\frac{1}{2g^2} \sigma^2 + \frac{1}{2\sqrt{\pi}} \frac{1}{\beta} \sum_{k=-\infty}^{\infty} \int_0^\infty \frac{dT}{T^{3/2}} e^{-T \left(\left(\frac{2\pi}{\beta} \right)^2 (k+1/2)^2 + \sigma^2 \right)} \right). \quad (10.7)$$

This action is minimal if

$$\frac{1}{g^2} = \frac{1}{2\sqrt{\pi}} \frac{1}{\beta} \sum_{k=-\infty}^{\infty} \int_0^\infty \frac{dT}{T^{1/2}} e^{-T \left(\left(\frac{2\pi}{\beta} \right)^2 (k+1/2)^2 + \sigma^2 \right)} \quad (10.8)$$

$$= \frac{1}{2} \frac{1}{\beta} \sum_{k=-\infty}^{\infty} \frac{1}{\sqrt{(2\pi/\beta)^2 (k+1/2)^2 + \sigma^2}} \quad (10.9)$$

$$= \frac{1}{4\pi} \sum_{k=-\infty}^{\infty} \frac{1}{\sqrt{(k+1/2)^2 + (\beta\sigma/2\pi)^2}}. \quad (10.10)$$

Introducing a UV cutoff k_{\max} , the large β limit of this expression yields the coupling as function of the physical mass m (defined for $T = 0$) and the UV cutoff k_{\max} and $p_{\max} = 2\pi k_{\max}/\beta$, respectively:

$$\frac{1}{g^2} = \lim_{\beta \rightarrow \infty} \frac{1}{2} \frac{1}{\beta} \sum_{k=-k_{\max}}^{k_{\max}-1} \frac{1}{\sqrt{(2\pi/\beta)^2 (k+1/2)^2 + m^2}} \quad (10.11)$$

$$= \frac{1}{2} \frac{1}{2\pi} \int_{-p_{\max}}^{p_{\max}} dp \frac{1}{\sqrt{p^2 + m^2}} \quad (10.12)$$

$$= \frac{1}{2\pi} \operatorname{arsinh}(p_{\max}/m) \quad (10.13)$$

$$\xrightarrow{p_{\max} \rightarrow \infty} \frac{1}{2\pi} (\ln(p_{\max}/m) + \ln 2), \quad (10.14)$$

cp. Eq. (9.21). We set $\sigma = 0$ in Eq. (10.10), to obtain a relation for the critical value of β (for which the σ value of the minimum vanishes):

$$\frac{1}{g^2} = \frac{1}{4\pi} \sum_{k=-k_{\max}}^{k_{\max}-1} \frac{1}{\sqrt{(k+1/2)^2}} \quad (10.15)$$

$$= \frac{1}{2\pi} \sum_{k=1}^{k_{\max}} \frac{1}{k-1/2} \quad (10.16)$$

$$\xrightarrow{k_{\max} \rightarrow \infty} \frac{1}{2\pi} (2\ln 2 + C + \ln(p_{\max}\beta_c/2\pi)), \quad (10.17)$$

Comparing both expressions for the cut-off dependent coupling, in terms of the physical mass m (Eq. (10.13)) and in terms of the critical value of β (Eq. (10.16)) (the difference of both terms is finite even for $k_{\max} \rightarrow \infty$), and taking the limit $k_{\max} \rightarrow \infty$ (Eq. (10.17), Eq. (10.14)),

$$\frac{1}{2\pi} (2\ln 2 + C + \ln(p_{\max}\beta_c/2\pi)) = \frac{1}{2\pi} (\ln(p_{\max}/m) + \ln 2), \quad (10.18)$$

we obtain the critical value of β and the corresponding critical temperature T_c in terms of the physical mass m :

$$\beta_c = \pi e^{-C} m^{-1} \approx 1.76387 m^{-1} \quad (10.19)$$

$$T_c = 1/\beta_c \approx 0.566932 m \quad (10.20)$$

(cp. [89]). For temperatures larger than the critical temperature T_c the potential σ vanishes and the spontaneously broken chiral symmetry is restored.

Chapter 11

Chemical potential

We extend the Euclidean action Eq. (8.7) by the term μN with the fermion number $N = \int d^D x \psi^\dagger \psi$,*

$$S = \int d^D x \left(-\bar{\psi} \not{\partial} \psi + \frac{g^2}{2N} (\bar{\psi} \psi)^2 + \mu \psi^\dagger \psi \right) \quad (11.1)$$

$$= \int d^D x \left(-\bar{\psi} \not{\partial} \psi + \frac{g^2}{2N} (\bar{\psi} \psi)^2 - \mu \psi^\dagger \gamma_D^2 \psi \right) \quad (11.2)$$

$$= \int d^D x \left(-\bar{\psi} (\not{\partial} + \mu \gamma_D) \psi + \frac{g^2}{2N} (\bar{\psi} \psi)^2 \right). \quad (11.3)$$

Repeating the calculations of section 8.2, we obtain the action for the scalar field,

$$S[\sigma] = \int d^D x \frac{N}{2g^2} \sigma^2 - N \text{tr} \ln(-\not{\partial} - \mu \gamma_D - i\sigma) \quad (11.4)$$

The operator $\not{\partial} + \mu \gamma_D - i\sigma$ has the same spectrum as the argument of the logarithm, $-\not{\partial} - \mu \gamma_D - i\sigma$. Again, this can be verified by applying γ_5 on both sides of the eigenvalue equation, considering that γ_5 anti-commutes with all other Dirac matrices.

*In this context, the symbol “ N ” does *not* refer to (infinite) flavour number

Consequently, the trace can be written as

$$\text{tr} \ln(-\not{\partial} - \mu\gamma_D - i\sigma) = \frac{1}{2} \text{tr} \ln((-\not{\partial} - \mu\gamma_D - i\sigma)(\not{\partial} + \mu\gamma_D - i\sigma)) \quad (11.5)$$

$$= \frac{1}{2} \text{tr} \ln(\partial^2 - \sigma^2 + i(\not{\partial}\sigma) + \mu^2 - \mu\{\not{\partial}, \gamma_D\}) \quad (11.6)$$

$$= \frac{1}{2} \text{tr} \ln(\partial^2 - \sigma^2 + i(\not{\partial}\sigma) + \mu^2 - 2\mu\partial_D) \quad (11.7)$$

$$= \frac{1}{2} \text{tr} \ln(\vec{\partial}^2 + (\partial_D + \mu)^2 - \sigma^2 + i(\not{\partial}\sigma)), \quad (11.8)$$

where $\vec{\partial}$ are the spatial components of ∂ . Subtracting the zero field term yields

$$\frac{1}{2} \text{tr} \ln \left(\frac{-\vec{\partial}^2 - (\partial_D + \mu)^2 + \sigma^2 - i(\not{\partial}\sigma)}{-\vec{\partial}^2 - (\partial_D + \mu)^2} \right) = \frac{1}{2} \text{tr} \ln \left(\frac{\vec{p}^2 + (p_D - i\mu)^2 + V(x)}{\vec{p}^2 + (p_D - i\mu)^2} \right),$$

where $p = -i\partial$ and $V(x) = \sigma^2 - i(\not{\partial}\sigma)$. To obtain the corresponding worldline expression, we perform the usual procedure [50] which we have already employed in chapter 3: we introduce a proper-time representation for the logarithm, perform the trace in x space and interpret the resulting matrix elements as non-relativistic quantum-mechanical transition-amplitudes, which can be written as path integrals over closed worldlines. The numerator in Eq. (11) corresponds to the quantum mechanical (worldline) Hamiltonian, $H_W = \vec{p}^2 + (p_D - i\mu)^2 + V(x)$. The corresponding worldline Lagrangian is

$$L_W = \frac{\dot{x}^2}{4} + i\mu\dot{x}_D - V(x), \quad (11.9)$$

and we obtain the worldline representation

$$\frac{1}{2} \text{tr} \ln \left(\frac{\vec{p}^2 + (p_D - i\mu)^2 + V(x)}{\vec{p}^2 + (p_D - i\mu)^2} \right) \quad (11.10)$$

$$= -\frac{1}{2} \frac{1}{(4\pi)^{D/2}} \int_0^\infty \frac{dT}{T^{1+D/2}} \int \mathcal{D}x \left(\text{tr}_\gamma \text{P} e^{i \int_0^{-iT} dt \left(\frac{\dot{x}^2}{4} + i\mu\dot{x}_D - V(x) \right)} - \text{tr}_\gamma \text{P} e^{i \int_0^{-iT} dt \left(\frac{\dot{x}^2}{4} + i\mu\dot{x}_D \right)} \right) \quad (11.11)$$

$$= -\frac{1}{2} \frac{1}{(4\pi)^{D/2}} \int_0^\infty \frac{dT}{T^{1+D/2}} \int \mathcal{D}x e^{-\int_0^T d\tau \left(\frac{\dot{x}^2}{4} + \mu\dot{x}_D \right)} \left(\text{tr}_\gamma \text{P} e^{-\int_0^T dt V(x)} - d_\gamma \right). \quad (11.12)$$

Now we write the paths $x(\tau)$ as in Eq. (10.1). Compared to Eq. (10.2), in Eq. (11.12) there is the additional $\mu\dot{x}_D$ term in the exponential weight factor. But the τ integral over this term is just $n\beta\mu$, where n is the winding number. Thus, instead of Eq. (10.3), we can write

$$\langle \dots \rangle \rightarrow \sum_{n=-\infty}^{\infty} (-1)^n e^{-\frac{n^2\beta^2}{4T} - n\beta\mu} \langle \dots \rangle. \quad (11.13)$$

Consequently, the full, unrenormalised action at finite temperature and finite chemical potential in D dimensions is obtained by a minor extension to the finite temperature result Eq. (8.36):

$$S[\sigma] = \int d^D x \left(\frac{1}{2g^2} \sigma^2 + \frac{1}{2} \frac{1}{(4\pi)^{D/2}} \int_{1/\Lambda^2}^{\infty} \frac{dT}{T^{1+D/2}} \left(\left(\sum_{n=-\infty}^{\infty} (-1)^n e^{-\frac{n^2\beta^2}{4T} - n\beta\mu} \right) \times \left\langle e^{-\int_0^T d\tau \sigma^2} \text{tr}_\gamma \mathbf{P} \cosh \left(i \int_0^T d\tau (\not{\partial} \sigma) \right) \right\rangle - d_\gamma \right) \right). \quad (11.14)$$

This action can be written as the sum of a vacuum part and a thermodynamic part,

$$S = S_{\text{vac}} + S^{\beta,\mu}, \quad (11.15)$$

where S_{vac} denotes the contribution which is independent of the thermodynamic quantities and corresponds to Eq. (8.36). The thermodynamic part $S^{\beta,\mu}$ is

$$S^{\beta,\mu} = \int d^D x \frac{1}{(4\pi)^{D/2}} \int_0^{\infty} \frac{dT}{T^{1+D/2}} \left(\sum_{n=1}^{\infty} (-1)^n e^{-\frac{\beta^2 n^2}{4T}} \cosh(\mu\beta n) \right) \times \left\langle e^{-\int_0^T d\tau \sigma^2} \text{tr}_\gamma \mathbf{P} \cosh \left(i \int_0^T d\tau (\not{\partial} \sigma) \right) \right\rangle. \quad (11.16)$$

The proper-time integral of this expression is finite, since all terms of the sum are exponentially suppressed for $T \rightarrow 0$.

Due to the separation into vacuum part and finite thermodynamic part, Eq. (11.15), the renormalisation of the action at finite temperature/chemical potential is exactly the same as for zero temperature/chemical potential. In $D = 2$ dimensions, we simply

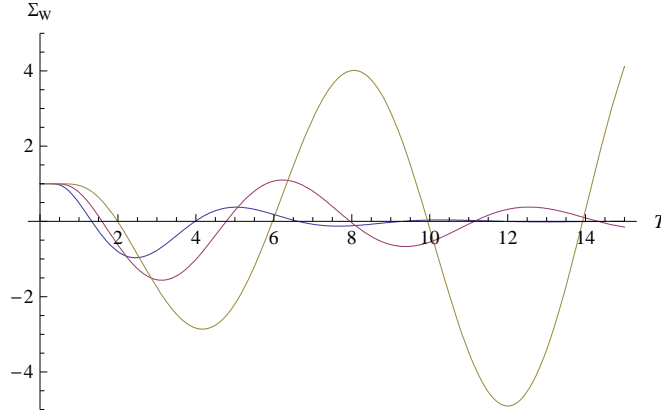


Figure 11.1: The winding sum Σ_W , Eq. (11.18), oscillates with increasing amplitude if $\beta\mu$ approaches π (here in three steps $T = 0.3, 0.25, 0.2$ at $\mu = \pi/5$).

insert the winding sum into Eq. (9.24):

$$S = \int d^2x \frac{1}{4\pi} \left(-\sigma^2 + \int_0^\infty \frac{dT}{T^2} \left(\frac{1}{2} \left(\sum_{n=-\infty}^{\infty} (-1)^n e^{-\frac{n^2\beta^2}{4T} - n\beta\mu} \right) \times \right. \right. \\ \left. \left. \times \left\langle e^{-\int_0^T d\tau \sigma^2} \text{tr}_\gamma P \cosh \left(i \int_0^T d\tau (\not{D}\sigma) \right) \right\rangle - \frac{\sigma^2}{m^2} (e^{-m^2T} - 1) - 1 \right) \right). \quad (11.17)$$

A shortcoming of this representation is that the T integral is in general only well defined for $\beta\mu \leq \pi$. If $\beta\mu > \pi$, the winding sum oscillates with increasing amplitude for large proptime values. This behaviour is typical for a Jacobi theta function with imaginary argument, in terms of which the winding sum can be written,

$$\Sigma_W := \sum_{n=-\infty}^{\infty} (-1)^n e^{-\frac{n^2\beta^2}{4T} - n\beta\mu} = \vartheta_4(i\mu\beta/2, \exp(-\beta^2/(4T))), \quad (11.18)$$

and exemplarily illustrated in Fig. 11.1. The continuation of expression Eq. (11.17) to the domain $\beta\mu > \pi$ has turned out to be highly non-trivial and is still work in progress. Even if the proptime is well defined, the winding sum and therewith the proptime integrand is oscillating rapidly for some temperatures and chemical potentials. This may result in a huge statistical error of the integral. In that case, it can be useful to employ the common techniques utilising the fourier transform of the winding sum, which has a very simple, non-oscillating shape.

Chapter 12

Towards the phase diagram

12.1 Phase diagram of the constant potential

For a fairly long time, the ground state of the Gross-Neveu model was believed to be translationally invariant, even at finite chemical potential. This assumption is not justified [90, 98], nevertheless the restriction to homogeneous ground states results in a non-trivial phase diagram [89], which agrees with the true phase diagram where the true ground state is homogeneous. This agreement includes a phase of broken chiral symmetry for small temperatures and chemical potential, and a critical line of a second-order transitions to a phase with restored chiral symmetry at finite temperature.

Now, with the worldline representation of the action for finite chemical potential and finite temperature at hand, we briefly revisit the constant potential. Actually, the worldline numerics for this is trivial, since the argument of the vacuum expectation in Eq. (11.17) yields the same value for any given worldline, namely $2 \exp(-T \sigma^2)$. However, the constant potential serves as a simple test for the (non-worldline) numerics of our algorithms and confirms the validity of the thermodynamic part of the action Eq. (11.16). In Fig. 12.1, the phase diagram obtained by numerically minimising the action Eq. (11.17) with respect to σ , for given chemical potential and temperature, is shown. In the accessible domain, that is for $\beta\mu < \pi$ as discussed above, the diagram nicely resembles the result of reference [89]. At $\mu = 0$, we recover the critical temperature Eq. (10.20). Even close to the line $T = \mu/\pi$, below which the proper-time integral is ill-defined, we obtain a stable result.

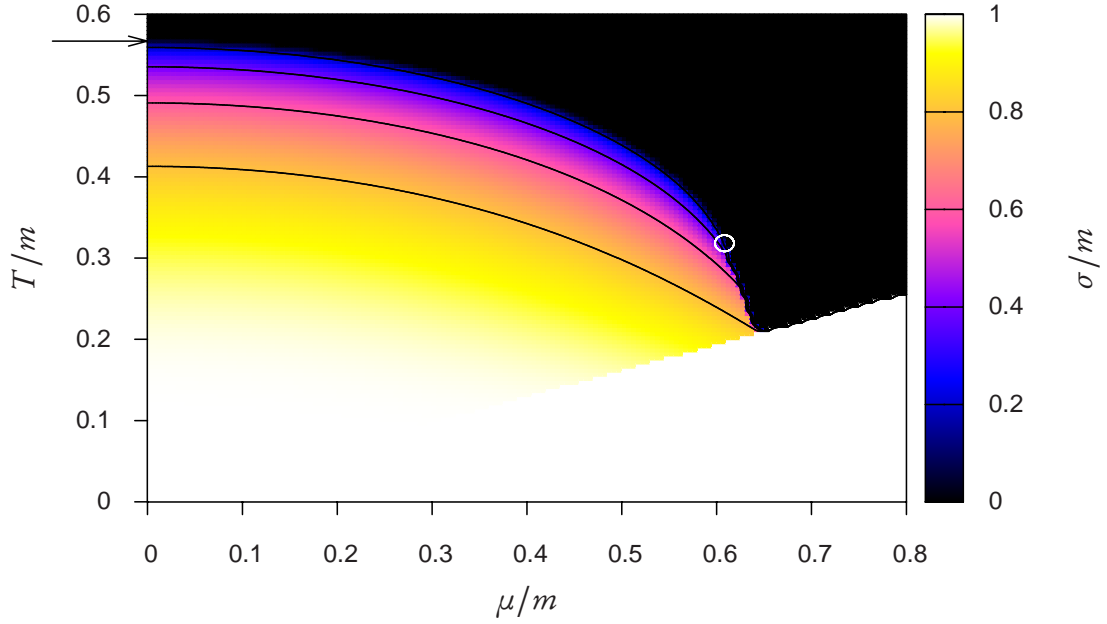


Figure 12.1: Phase diagram for a constant potential (cp. [89]) computed by numerically minimising the action Eq. (11.17) with respect to σ . The colour corresponds to the resulting σ value. In black, the phase of restored chiral symmetry. The tricritical point is marked by a white circle, situated between phase transitions of second order (the upper boundary of the blue region) and transitions of first order (discrete jump of the colour/ σ value). The line of second order transitions extends to the $\mu = 0$ axis, where it is marked by an arrow at the value $T_c \approx 0.567$ (Eq. (10.20)). The blank region below the $T = \mu/\pi$ line is inaccessible to the given expression for the action as discussed in the text.

12.2 In search of crystals

As we know today, instead of the phase transition of first order, there is a crystalline third phase down right in the phase diagram Fig. 12.1 [90]. With regard to using worldline numerics for the search for crystals in higher dimensions, an important question is, if this crystal phase of the two dimensional model can be rediscovered.

For the potential, we have to choose a sufficiently general ansatz with a sufficient number of free parameters, which will be determined by minimising the action. In the previous section, the ansatz has been the constant field with only one parameter, but clearly this has not been sufficient to find a crystal phase. In general, the potential can be parametrised using bicubic splines [99], for instance. For a first test, we simply use the kink-antikink array of Eq. (9.49). This means, we have to minimise with respect to three parameters.

The *Simplex* algorithm of Nelder and Mead [100] has proven to minimize quite efficiently without making use of derivative terms of, in our case, the action. For the multidimensional integral, here the integral over the proptime and the x_1 coordinate,

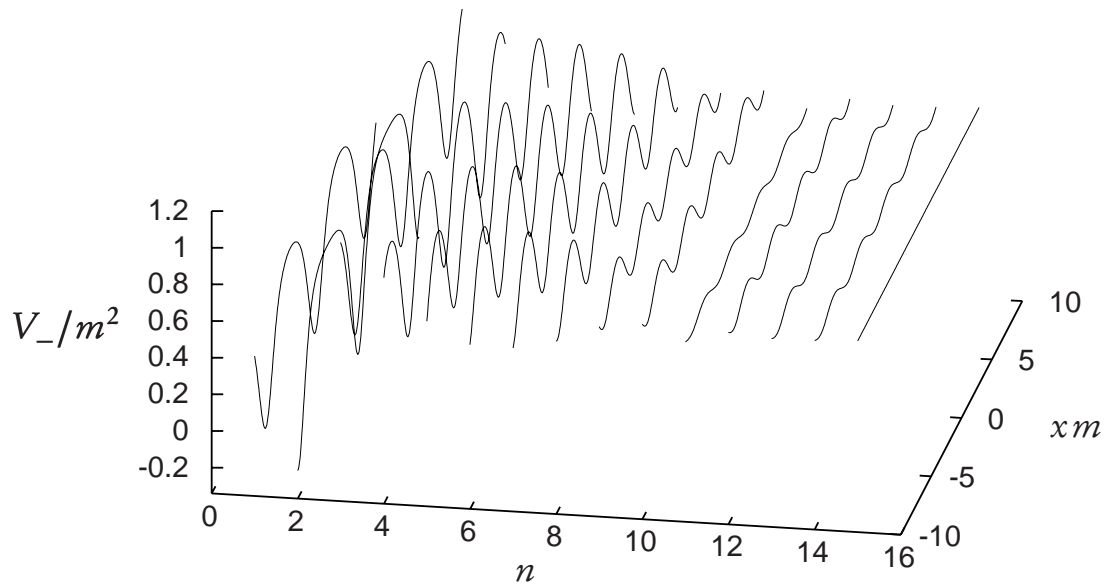


Figure 12.2: Minimisation of the action at $\mu = 0.56$ and $T = 0.25$. Starting from an initial configuration (left), the algorithm adjusts the three parameters of the V_- potential Eq. (9.49) to minimise the action. After 13 intermediate results, labelled with $n = 1, \dots, 14$, it finally approaches at the correct minimum $V_- \approx 0.7$. In the process, the action is computed worldline numerically, employing an ensemble of 1000 loops, each with 100 points.

we use the *VEGAS* Monte Carlo algorithm [101, 102]. Both algorithms are probably not the most efficient choices for this simple test, but they are robust and can also be used with more free parameters and in higher dimensions.

Figure 12.2 shows the result of a test run with chemical potential $\mu = 0.56$ and a temperature $T = 0.25$. Starting from some initial configuration, the algorithm correctly recovers the constant solution.

Similar results are obtained in the phase with restored chiral symmetry. In the crystal phase, first test runs suggest that the statistical error of the previous calculation is too large for a significant result. Runs with higher statistics and the corresponding amount of CPU time have to clarify this.

Chapter 13

Conclusions (Part II)

So far, we have succeeded in several steps of our worldline-numerical studies of the Gross-Neveu model. The fermionic functional-determinant in the action of the auxiliary scalar field has been translated into a worldline path-integral, which in turn could be evaluated by worldline numerical techniques. This has been demonstrated, initially at zero temperature and with no chemical potential, for potentials involving kinks and antikinks. These potentials include the kink-antikink array, which presents the real ground state of the theory for certain temperatures and chemical potentials. We have thereby observed an overlap problem for certain potentials, but this could be traced back to the presence of a zero mode in the quantum mechanical eigenstate-problem of the given potential. Though the presence of a zero mode appears to be a special case, the mode can in principle be determined by a worldline numeric computation. This knowledge can then be utilised to avoid the overlap problem.

We have introduced finite temperature by compactifying the Euclidean time. This allows the closed worldlines to wind around the finite temperature cylinder and results in a prefactor to the worldline expectation value involving a sum over all possible winding numbers.

Finite chemical potential has turned out to be a minor extension to the winding sum. However, the resulting worldline expression for the action is not well defined for all combinations of temperature and chemical potential. Nevertheless, in the accessible domain, it nicely reproduces the phase diagram for the translation invariant field.

Finally, we have provided a demonstration of a universal algorithm, minimizing the action of the kink-antikink array at finite temperature and chemical potential.

Future work will concentrate on the continuation of the worldline expression to the whole μ - T plane of the phase diagram. As long as a suitable expression is not available, employing more CPU time for the numerical evaluation of the expression

at hand will allow to recover the crystal phase in the accessible part of the phase diagram.

A long-term objective is to extend our studies to the three dimensional Gross-Neveu model. Qualitatively this should not be much more complicated than the present studies of the two dimensional model (though it will require more computing power). Nevertheless, these studies will shed light on the question, if crystalline phases are a special case of low dimensional theories or also to be expected in higher dimensions, possibly even in QCD.

Beyond the Gross-Neveu model, the worldline expression for finite temperature can be applied to the Casimir computations presented in the first part of the theses. This will provide a detailed understanding of the influence of thermal fluctuations on the Casimir force, a subject of recent controversial discussion [22–24].

Bibliography

- [1] H. B. G. Casimir. On the attraction between two perfectly conducting plates. *Indag. Math.*, 10:261–263, 1948. 3, 7, 36
- [2] S. K. Lamoreaux. Demonstration of the casimir force in the 0.6 to 6 micrometers range. *Phys. Rev. Lett.*, 78:5–7, 1997. 3, 4, 37
- [3] U. Mohideen and Anushree Roy. Precision measurement of the casimir force from 0.1 to 0.9 μm . *Phys. Rev. Lett.*, 81:4549–4552, 1998. 3, 4, 22, 37
- [4] Anushree Roy, Chiung-Yuan Lin, and U. Mohideen. Improved precision measurement of the casimir force. *Phys. Rev.*, D60:111101, 1999. 3, 4, 37
- [5] Thomas Ederth. Template-stripped gold surfaces with 0.4-nm rms roughness suitable for force measurements: Application to the casimir force in the 20–100-nm range. *Phys. Rev. A*, 62(6):062104, Nov 2000. 3, 4, 37
- [6] H. B. Chan, V. A. Aksyuk, R. N. Kleiman, D. J. Bishop, and Federico Capasso. Quantum Mechanical Actuation of Microelectromechanical Systems by the Casimir Force. *Science*, 291(5510):1941–1944, 2001. 3, 4, 37
- [7] F. Chen, U. Mohideen, G. L. Klimchitskaya, and V. M. Mostepanenko. Demonstration of the lateral casimir force. *Phys. Rev. Lett.*, 88(10):101801, Feb 2002. 3, 4, 37
- [8] M. Bordag, B. Geyer, G. L. Klimchitskaya, and V. M. Mostepanenko. Constraints for hypothetical interactions from a recent demonstration of the casimir force and some possible improvements. *Phys. Rev.*, D58:075003, 1998. 3
- [9] M. Bordag, B. Geyer, G. L. Klimchitskaya, and V. M. Mostepanenko. Stronger constraints for nanometer scale yukawa-type hypothetical interactions from the new measurement of the casimir force. *Phys. Rev.*, D60:055004, 1999. 3
- [10] M. Bordag, B. Geyer, G. L. Klimchitskaya, and V. M. Mostepanenko. New constraints for non-newtonian gravity in nanometer range from the improved precision measurement of the casimir force. *Phys. Rev.*, D62:011701, 2000. 3

- [11] Joshua C. Long, Hilton W. Chan, and John C. Price. Experimental status of gravitational-strength forces in the sub-centimeter regime. *Nucl. Phys.*, B539:23–34, 1999. 3
- [12] V. M. Mostepanenko and M. Novello. Constraints on non-newtonian gravity from the casimir force measurements between two crossed cylinders. *Phys. Rev.*, D63:115003, 2001. 3
- [13] K. A. Milton, R. Kantowski, C. Kao, and Y. Wang. Constraints on extra dimensions from cosmological and terrestrial measurements. *Mod. Phys. Lett.*, A16:2281–2290, 2001. 3
- [14] R. S. Decca et al. Improved tests of extra-dimensional physics and thermal quantum field theory from new casimir force measurements. *Phys. Rev.*, D68:116003, 2003. 3, 4, 37
- [15] R. S. Decca et al. Constraining new forces in the casimir regime using the isoelectronic technique. *Phys. Rev. Lett.*, 94:240401, 2005. 3, 4, 37
- [16] G. L. Klimchitskaya, Anushree Roy, U. Mohideen, and V. M. Mostepanenko. Complete roughness and conductivity corrections for casimir force measurement. *Phys. Rev. A*, 60(5):3487–3495, Nov 1999. 3, 37
- [17] Astrid Lambrecht and Serge Reynaud. Casimir force between metallic mirrors. *Eur. Phys. J.*, D8:309–318, 2000. 3, 37
- [18] V. B. Bezerra, G. L. Klimchitskaya, and V. M. Mostepanenko. Higher-order conductivity corrections to the casimir force. *Phys. Rev. A*, 62(1):014102, Jun 2000. 3, 37
- [19] M. Bordag, U. Mohideen, and V. M. Mostepanenko. New developments in the casimir effect. *Phys. Rept.*, 353:1–205, 2001. 3, 37, 59
- [20] A. Lambrecht P. A. Maia Neto and S. Reynaud. Roughness correction to the casimir force: Beyond the proximity force approximation. *Europhysics Letters (EPL)*, 69(6):924–930, 2005. 3, 37
- [21] Paulo A. Maia Neto, Astrid Lambrecht, and Serge Reynaud. Casimir effect with rough metallic mirrors. *Physical Review A (Atomic, Molecular, and Optical Physics)*, 72(1):012115, 2005. 3, 37
- [22] V. M. Mostepanenko et al. Present status of controversies regarding the thermal casimir force. *J. Phys.*, A39:6589–6600, 2006. 3, 37, 102
- [23] Iver Brevik, Simen A. Ellingsen, and Kimball A. Milton. Thermal corrections to the casimir effect. *New J. Phys.*, 8:236, 2006. 3, 102

- [24] M. Boström and Bo E. Sernelius. Thermal effects on the casimir force in the 0.1– $5\mu\text{m}$ range. *Phys. Rev. Lett.*, 84(20):4757–4760, May 2000. 3, 37, 102
- [25] N. Graham et al. Calculating vacuum energies in renormalizable quantum field theories: A new approach to the casimir problem. *Nucl. Phys.*, B645:49–84, 2002. 3, 4, 5
- [26] G. Bressi, G. Carugno, R. Onofrio, and G. Ruoso. Measurement of the casimir force between parallel metallic surfaces. *Phys. Rev. Lett.*, 88:041804, 2002. 4, 22, 56
- [27] B. V. Derjaguin, I. I. Abrikosova, and E. M. Lifshitz. Direct measurement of molecular attraction between solids separated by a narrow gap. *Q. Rev. Chem. Soc.*, 10:295 – 329, 1956. 4, 59
- [28] J. Blocki, J. Randrup, W. J. Swiatecki, and C. F. Tsang. Proximity forces. *Annals of Physics*, 105(2):427–462, June 1977. 4, 59
- [29] Martin Schaden and Larry Spruch. Infinity-free semiclassical evaluation of casimir effects. *Phys. Rev. A*, 58(2):935–953, Aug 1998. 4, 32, 58, 62
- [30] Martin Schaden and Larry Spruch. Focusing virtual photons: Casimir energies for some pairs of conductors. *Phys. Rev. Lett.*, 84(3):459–462, Jan 2000. 4, 32, 58, 62
- [31] Ramin Golestanian and Mehran Kardar. Path integral approach to the dynamic casimir effect with fluctuating boundaries. 1998. 4
- [32] Thorsten Emig, Andreas Hanke, and Mehran Kardar. Probing the strong boundary shape dependence of the casimir force. *Phys. Rev. Lett.*, 87:260402, 2001. 4, 55
- [33] Thorsten Emig. Casimir forces: An exact approach for periodically deformed objects. *Europhys. Lett.*, 62:466–472, 2003. 4, 55
- [34] Thorsten Emig and Rauno Buscher. Towards a theory of molecular forces between deformed media. *Nucl. Phys.*, B696:468–491, 2004. 4
- [35] Holger Gies, Kurt Langfeld, and Laurent Moyaerts. Casimir effect on the worldline. *JHEP*, 06:018, 2003. 4, 13, 18, 19, 29, 39, 62
- [36] A. Scardicchio and R. L. Jaffe. Casimir effects: An optical approach i. foundations and examples. *Nucl. Phys.*, B704:552–582, 2005. 4, 29, 32, 58, 60
- [37] R. L. Jaffe and A. Scardicchio. The casimir effect and geometric optics. *Phys. Rev. Lett.*, 92:070402, 2004. 4, 29, 32, 58, 60

- [38] Aurel Bulgac, Piotr Magierski, and Andreas Wirzba. Scalar casimir effect between dirichlet spheres or a plate and a sphere. *Phys. Rev.*, D73:025007, 2006. 4, 21, 29, 30, 32
- [39] Andreas Wirzba, Aurel Bulgac, and Piotr Magierski. Casimir interaction between normal or superfluid grains in the fermi sea. *J. Phys.*, A39:6815–6822, 2006. 4, 21, 29, 30, 32
- [40] T. Emig, R. L. Jaffe, M. Kardar, and A. Scardicchio. Casimir interaction between a plate and a cylinder. *Phys. Rev. Lett.*, 96:080403, 2006. 4, 21, 33, 34, 57
- [41] M. Bordag. The casimir effect for a sphere and a cylinder in front of plane and corrections to the proximity force theorem. *Phys. Rev.*, D73:125018, 2006. 4, 21, 33, 57, 58
- [42] Holger Gies and Kurt Langfeld. Quantum diffusion of magnetic fields in a numerical worldline approach. *Nucl. Phys.*, B613:353–365, 2001. 4
- [43] Holger Gies and Kurt Langfeld. Loops and loop clouds: A numerical approach to the worldline formalism in qed. *Int. J. Mod. Phys.*, A17:966–978, 2002. 4
- [44] Kurt Langfeld, Laurent Moyaerts, and Holger Gies. Fermion-induced quantum action of vortex systems. *Nucl. Phys.*, B646:158–180, 2002. 4
- [45] L. Moyaerts, K. Langfeld, and H. Gies. Worldline approach to the casimir effect. 2003. 4
- [46] R. P. Feynman. Mathematical formulation of the quantum theory of electromagnetic interaction. *Phys. Rev.*, 80:440–457, 1950. 4
- [47] Alexander M. Polyakov. Gauge fields and strings. CHUR, SWITZERLAND: HARWOOD (1987) 301 P. (CONTEMPORARY CONCEPTS IN PHYSICS, 3). 4
- [48] Matthew J. Strassler. Field theory without feynman diagrams: One loop effective actions. *Nucl. Phys.*, B385:145–184, 1992. 4
- [49] Michael G. Schmidt and Christian Schubert. On the calculation of effective actions by string methods. *Phys. Lett.*, B318:438–446, 1993. 4
- [50] Christian Schubert. Perturbative quantum field theory in the string-inspired formalism. *Phys. Rept.*, 355:73–234, 2001. 4, 15, 22, 94
- [51] Michael G. Schmidt and Ion-Olimpiu Stamatescu. Determinant calculations with random walk worldline loops. 2002. 4

- [52] Michael G. Schmidt and Ion-Olimpiu Stamatescu. Determinant calculations using random walk worldline loops. *Nucl. Phys. Proc. Suppl.*, 119:1030–1032, 2003. 4
- [53] Holger Gies and Klaus Klingmuller. Quantum energies with worldline numerics. *J. Phys.*, A39:6415–6422, 2006. 4, 18, 21, 29, 40, 43
- [54] Holger Gies and Klaus Klingmuller. Casimir effect for curved geometries: Pfa validity limits. *Phys. Rev. Lett.*, 96:220401, 2006. 4, 21
- [55] Noah Graham and Ken D. Olum. Plate with a hole obeys the averaged null energy condition. *Phys. Rev.*, D72:025013, 2005. 5
- [56] H. B. G. Casimir and D. Polder. The influence of retardation on the london-van der waals forces. *Phys. Rev.*, 73:360–372, 1948. 7, 30
- [57] R. L. Jaffe. The casimir effect and the quantum vacuum. *Phys. Rev.*, D72:021301, 2005. 7, 37
- [58] H. Verschelde, L. Wille, and P. Phariseau. Casimir effect in n dimensions. *Phys. Lett.*, B149:396–398, 1984. 9, 39
- [59] K. A. Milton. The casimir effect: Physical manifestations of zero-point energy. River Edge, USA: World Scientific (2001) 301 p. 10, 37
- [60] A. Chodos, R. L. Jaffe, K. Johnson, Charles B. Thorn, and V. F. Weisskopf. A new extended model of hadrons. *Phys. Rev.*, D9:3471–3495, 1974. 11
- [61] A. Larraza and B. Denardo. An acoustic casimir effect. *Phys. Lett. A*, 248:151–155, 1998. 11
- [62] P. C. Caussée. *L'Album du Marin*. Mantes, Charpentier, 1836. 11, 12
- [63] Sipko L. Boersma. A maritime analogy of the casimir effect. *American Journal of Physics*, 64(5):539–541, 1996. 11
- [64] E. Buks and M. L. Roukes. Quantum physics: Casimir force changes sign. *Nature*, 419:119–120, 2002. 11
- [65] M Reuter and W Dittrich. Regularisation schemes for the casimir effect. *European Journal of Physics*, 6(1):33–40, 1985. 16
- [66] D. Deutsch and P. Candelas. Boundary effects in quantum field theory. *Phys. Rev.*, D20:3063, 1979. 17
- [67] P. Candelas. Vacuum polarization in the presence of dielectric and conducting surfaces. *Ann. Phys.*, 143:241, 1982. 17

- [68] G. Barton. Perturbative casimir energies of dispersive spheres, cubes and cylinders. *J. Phys.*, A34:4083–4114, 2001. 17
- [69] N. Graham et al. The dirichlet casimir problem. *Nucl. Phys.*, B677:379–404, 2004. 17
- [70] H. Weigel. Dirichlet spheres in continuum quantum field theory. 2003. 17
- [71] Oded Kenneth and Israel Klich. Opposites attract - a theorem about the casimir force. *Phys. Rev. Lett.*, 97:160401, 2006. 19
- [72] Holger Gies and Klaus Klingmuller. Worldline algorithms for casimir configurations. *Phys. Rev.*, D74:045002, 2006. 21, 35
- [73] Michael Brown-Hayes, Diego A. R. Dalvit, Francisco D. Mazzitelli, Woo-Joong Kim, and Roberto Onofrio. Towards a precision measurement of the casimir force in a cylinder-plane geometry. *Phys. Rev.*, A72:052102, 2005. 22
- [74] A. Scardicchio and R. L. Jaffe. Casimir effects: an optical approach ii. local observables and thermal corrections. *Nucl. Phys.*, B743:249–275, 2006. 22
- [75] I. Brevik, E. K. Dahl, and G. O. Myhr. Casimir force on a micrometer sphere in a dip: Proposal of an experiment. *J. Phys.*, A38:L49–L56, 2005. 30
- [76] V. Druzhinina and M. DeKieviet. Experimental observation of quantum reflection far from threshold. *Phys. Rev. Lett.*, 91(19):193202, Nov 2003. 30
- [77] M. Brown-Hayes, D. A. R. Dalvit, F. D. Mazzitelli, W. J. Kim, and R. Onofrio. Towards a precision measurement of the casimir force in a cylinder-plane geometry. *Physical Review A (Atomic, Molecular, and Optical Physics)*, 72(5):052102, 2005. 32
- [78] F. D. Mazzitelli D. A. R. Dalvit, F. C. Lombardo and R. Onofrio. Casimir force between eccentric cylinders. *Europhysics Letters (EPL)*, 67(4):517–523, 2004. 32
- [79] D. C. Roberts and Y. Pomeau. Casimir-like force arising from quantum fluctuations in a slowly moving dilute bose-einstein condensate. *Physical Review Letters*, 95(14):145303, 2005. 35
- [80] Holger Gies and Klaus Klingmuller. Casimir edge effects. *Phys. Rev. Lett.*, 97:220405, 2006. 35
- [81] H. Kleinert. **PATH INTEGRALS** in quantum mechanics, statistics, polymer physics, and financial markets. World Scientific, Singapore, 2004. 39

- [82] N. F. Svaiter and B. F. Svaiter. Casimir effect in a d-dimensional flat space-time and the cutoff method. *J. Math. Phys.*, 32:175–180, 1991. 39
- [83] Ariel Edery. Multidimensional cut-off technique, odd-dimensional epstein zeta functions and casimir energy of massless scalar fields. *J. Phys.*, A39:685–712, 2006. 39
- [84] Robson B. Rodrigues, Paulo A. Maia Neto, Astrid Lambrecht, and Serge Reynaud. Lateral casimir force beyond the proximity force approximation. *Phys. Rev. Lett.*, 96:100402, 2006. 57
- [85] Yoichiro Nambu and G. Jona-Lasinio. Dynamical model of elementary particles based on an analogy with superconductivity. i. *Phys. Rev.*, 122:345–358, 1961. 65
- [86] Yoichiro Nambu and G. Jona-Lasinio. Dynamical model of elementary particles based on an analogy with superconductivity. ii. *Phys. Rev.*, 124:246–254, 1961. 65
- [87] David J. Gross and Andre Neveu. Dynamical symmetry breaking in asymptotically free field theories. *Phys. Rev.*, D10:3235, 1974. 65, 67
- [88] Michael Thies and Konrad Urlichs. From non-degenerate conducting polymers to dense matter in the massive gross-neveu model. *Phys. Rev.*, D72:105008, 2005. 65
- [89] U. Wolff. The phase diagram of the infinite n gross-neveu model at finite temperature and chemical potential. *Phys. Lett.*, B157:303–308, 1985. 65, 92, 97, 98
- [90] Michael Thies and Konrad Urlichs. Revised phase diagram of the gross-neveu model. *Phys. Rev.*, D67:125015, 2003. 65, 78, 85, 97, 98
- [91] K. Gawedzki and A. Kupiainen. Renormalizing the nonrenormalizable. *Phys. Rev. Lett.*, 55:363–365, 1985. 72
- [92] Roger F. Dashen, Brosl Hasslacher, and Andre Neveu. Semiclassical bound states in an asymptotically free theory. *Phys. Rev.*, D12:2443, 1975. 78
- [93] Holger Gies and Klaus Klingmuller. Pair production in inhomogeneous fields. *Phys. Rev.*, D72:065001, 2005. 79
- [94] Gerald V. Dunne. private communication, 2007. 79, 81, 85, 86
- [95] S. Duane, A. D. Kennedy, B. J. Pendleton, and D. Roweth. Hybrid monte carlo. *Phys. Lett.*, B195:216–222, 1987. 84

- [96] A. Irback. Hybrid monte carlo simulation of polymer chains. 1993. 84
- [97] Kurt Langfeld. private communication, 2007. 84
- [98] Andrej Brzoska and Michael Thies. No first-order phase transition in the gross-neveu model? *Phys. Rev.*, D65:125001, 2002. 97
- [99] William H. Press, Brian P. Flannery, Saul A. Teukolsky, and William T. Vetterling. *Numerical Recipes in C : The Art of Scientific Computing*. Cambridge University Press, October 1992. 98
- [100] J.A. Nelder and R. Mead. A simplex method for function minimization. *Computer Journal*, 7:308–315, 1965. 98
- [101] G.P. Lepage. A new algorithm for adaptive multidimensional integration. *Journal of Computational Physics*, 27:192–203, 1978. 99
- [102] G.P. Lepage. Vegas: An adaptive multi-dimensional integration program. *Cornell preprint*, 1980. 99

Danke!

Ganz besonders herzlich möchte ich mich für die motivierende, kompetente und immer freundliche Betreuung und die Zusammenarbeit an einem spannenden Thema bei Holger Gies bedanken. Prof. Michael G. Schmidt bin ich sehr dankbar, dass auch er die vorliegende Arbeit begutachtet. Ebenso danke ich Gerald Dunne, seine analytischen Ergebnisse für die Pfadintegrale im Gross-Neveu Modell waren eine große Hilfe bei der Entwicklung der Numerik.

Für die angenehme und lebhafte Atmosphäre im Westzimmer und für außeruniversitäre Betätigungen danke ich den Kollegen und Freunden am Institut, wie auch denen, die schon über alle Berge sind.

Schließlich wäre diese Arbeit nicht möglich gewesen, ohne die Unterstützung meiner Eltern, Geschwister und Christine.